4th INTERNATIONAL CONFERENCE NMSCAA'24

SOZOPOL, BULGARIA
June 17 - 21, 2024

NUMERICAL METHODS FOR SCIENTIFIC COMPUTATIONS AND ADVANCED APPLICATIONS

PROCEEDINGS OF SHORT COMMUNICATIONS

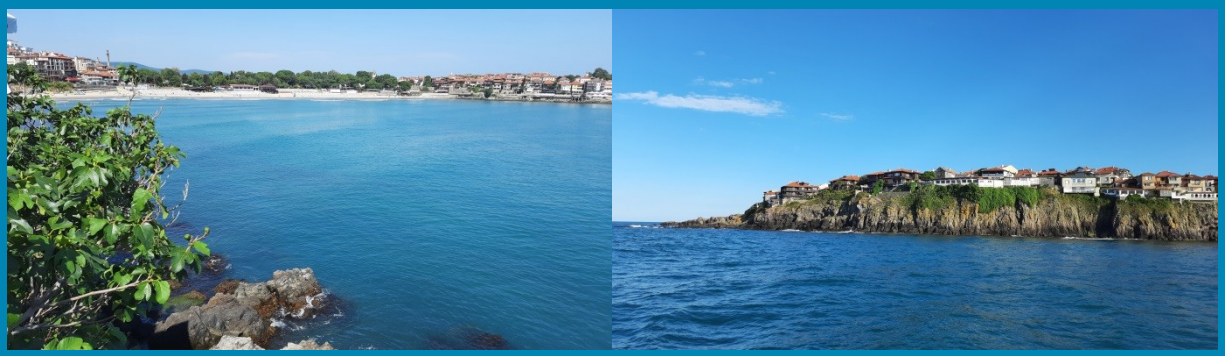

SVETOZAR MARGENOV

INTERNATIONAL CONFERENCE

NMSCAA'24

SOZOPOL, BULGARIA
JUNE 17 – 21, 2024

NUMERICAL METHODS FOR SCIENTIFIC COMPUTATIONS AND ADVANCED APPLICATIONS

PROCEEDINGS
OF SHORT COMMUNICATIONS

SVETOZAR MARGENOV

Editor
Svetozar Margenov
Bulgarian Academy of Sciences
Sofia, Bulgaria

ISBN 978-619-7320-11-4 (eBook)
Institute of Information and Communication Technologies, Bulgarian Academy of Sciences,
Acad. G. Bonchev Str., Bl. 2, 1113 Sofia, Bulgaria, 2024

PREFACE

The 4th International Conference on Numerical Methods for Scientific Computations and Advanced Applications (NMSCAA'24) is organized by the Institute of Information and Communication Technologies, Bulgarian Academy of Sciences and MIV Consult Ltd. in cooperation with Bulgarian Section of SIAM (BG SIAM).

The conference is dedicated to the 155th anniversary of the Bulgarian Academy of Sciences.

The major specific topics of NMSCAA'24 include: (i) Modeling, simulation and optimization; (ii) Multiscale and multiphysics problems; (iii) Robust iterative methods and sparse matrix computation; (iv) Fractional differential equations and non-local problems; (v) Parallel numerical methods and scalable algorithms; (vi) Advanced applications in science and engineering.

Keynote speakers and lectures

- Lidia Aceto (University of Eastern Piedmont, Alessandria, Italy)
  On the Computation of Fractional Powers of Operators
- Oleg Iliev (FTWM, Kaiserslautern, Germany)
  On the Efficient Preconditioning of the Stokes Equations in Tight Geometries
- Johannes Kraus (University of Duisburg-Essen, Germany)
  Convergence Analysis of Time-Continuous Strongly Conservative Space-Time Finite Element Methods for the Dynamic Biot Model
- Maya Neytcheva (Uppsala University, Sweden)
  Three Krylov Subspace Iteration Methods that Incorporate Variable Preconditioning
- Ludmil Zikatanov (Penn State and NSF, US)
  Operator Preconditioning and Reduced Basis Methods

Special sessions and organizers

- *Numerical solution of fractional differential equations and applications*, Lidia Aceto (University of Eastern Piedmont, Alessandria, Italy), Stanislav Harizanov (IICT-BAS, Bulgaria)
- *Advanced Computing in Life and Material Sciences and Climate Research*, Nevena Ilieva (IICT-BAS, Bulgaria)
- *Mathematical Modelling in Medicine*, Stefka Fidanova (IICT-BAS, Bulgaria)

Tutorial

- *Optimizing applications on the supercomputer HEMUS*, Emanouil Atanassov, Svetlozar Yordanov (IICT-BAS, Bulgaria)

The purpose of the conference is to bring together scientists in the field of numerical methods for scientific computations working with models in natural sciences and biomedical, environmental and industrial applications, as well as developers of algorithms for modern high-performance computers. Authors from more than 10 countries all over the world (America, Asia, and Europe) contributed to the success of the conference.

Acknowledgement
The event is organized with the financial support of Hewlett Packard Enterprise Bulgaria, operated by Selectium Bulgaria.

Svetozar Margenov

Table of Contents

On the Computation of Fractional Powers of Operators

L. Aceto

We consider the numerical approximation of $\mathcal{L}^{-\alpha}, \alpha \in (0,1)$. Here $\mathcal{L}$ is a self-adjoint positive operator acting in an Hilbert space $\mathcal{H}$ in which the eigenfunctions of $\mathcal{L}$ form an orthonormal basis of $\mathcal{H}$, so that $\mathcal{L}^{-\alpha}$ can be written through the spectral decomposition of $\mathcal{L}$. In other words, for a given $g \in \mathcal{H}$, we have

$$\mathcal{L}^{-\alpha} g = \sum_{j=1}^{+\infty} \mu_j^{-\alpha} \langle g, \varphi_j \rangle \varphi_j$$

where μ_j and φ_j are the eigenvalues and the eigenfunctions of $\mathcal{L}$, respectively, and $\langle \cdot, \cdot \rangle$ denotes the $\mathcal{H}$-inner product.

This problem finds immediate application when solving equations involving a fractional diffusion term like $(-\Delta)^{\alpha}$, where Δ denotes the standard Laplacian, and this is the main reason for which in recent years a lot of attention has been placed on the efficient approximation of fractional powers. Among the approaches recently introduced we quote the methods based on the best uniform rational approximation (BURA) of functions closely related to $\lambda^{-\alpha}$ that have been considered in [1–4] by using a modified version of the Remez algorithm. Another class of methods relies on quadrature rules for the integral representation of $\lambda^{-\alpha}$ [5–13]. Starting from the integral representation given in [10, Eq. (4)]

$$\mathcal{L}^{-\alpha} = \frac{2\sin(\alpha\pi)}{\pi} \int_0^{+\infty} t^{2\alpha-1} (\mathcal{I} + t^2 \mathcal{L})^{-1} dt, \qquad \alpha \in (0,1),$$

where $\mathcal{I}$ is the identity operator in $\mathcal{H}$, after suitable changes of variables and quadrature rules one typically finds rational approximations of the type

$$\mathcal{L}^{-\alpha} \approx \mathcal{R}_{m-1,m}(\mathcal{L}), \quad \mathcal{R}_{m-1,m}(\lambda) = \frac{p_{m-1}(\lambda)}{q_m(\lambda)}, \quad p_{m-1} \in \Pi_{m-1},\ q_m \in \Pi_m,$$

where m is equal or closely related to the number of points of the quadrature formula. In this talk we present a comparative analysis of the most reliable existing methods based on quadrature rules, with particular attention to the error estimate and the asymptotic rate of convergence (see e.g. [6–11,14]). The analysis is given in the infinite dimensional setting, so that all results can be directly applied to the discrete case, independently of the discretization used.

References

[1] Harizanov, S., Lazarov, R., Margenov, S., Marinov, P. and Vutov, Y. 2018 *Optimal solvers for linear systems with fractional powers of sparse SPD matrices*. Numer. Linear Algebra Appl. 25, no. 5, e2167.

[2] Harizanov, S., Lazarov, R., Marinov, P., Margenov, S. and Pasciak, J.E. 2020 *Analysis of numerical methods for spectral fractional elliptic equations based on the best uniform rational approximation*. J. Comput. Phys. 408, 109285.

[3] Harizanov, S., Lazarov, R., Marinov, P., Margenov, S. and Pasciak, J.E. 2019 Comparison analysis of two numerical methods for fractional diffusion problems based on the best rational approximations of t^{γ} on $[0,1]$. In *Advanced Finite Element Methods with Applications. FEM 2017* (ed. T. Apel, U. Langer, A. Meyer and O. Steinbach). Lecture Notes in Computational Science and Engineering, vol. 128. Springer.

[4] Harizanov, S. and Margenov, S. 2018 Positive approximations of the inverse of fractional powers of SPD M-Matrices. In *Control Systems and Mathematical Methods in Economics* (ed. G. Feichtinger, R. Kovacevic and G. Tragler). Lecture Notes in Economics and Mathematical Systems, vol. 687. Springer.

[5] Aceto, L., Bertaccini, D., Durastante, F. and Novati, P. 2019 *Rational Krylov methods for functions of matrices with applications to fractional partial differential equations*. J. Comput. Phys. 396, 470–482.

[6] Aceto, L., and Novati, P. 2018 *Efficient implementation of rational approximations to fractional differential operators*. J Sci Comput 76, 651–671.

[7] Aceto, L. and Novati, P. 2022 *Fast and accurate approximations to fractional powers of operators*. IMA J. Numer. Anal. 42(2), 1598-1622.
[8] Aceto, L. and Novati, P. 2020 *Padé-type approximations to the resolvent of fractional powers of operators*. J. Sci. Comput. 83, 13.
[9] Aceto, L. and Novati, P. 2019 *Rational approximations to fractional powers of self-adjoint positive operators*. Numer. Math. 143, 1–16.
[10] Bonito, A. and Pasciak, J.E. 2015 *Numerical approximation of fractional powers of elliptic operators*. Math. Comp. 84, 2083–2110.
[11] Bonito, A. and Pasciak, J.E. 2019 *On sinc quadrature approximations of fractional powers of regularly accretive operators*. J. Numer. Math. 27, 57–68.
[12] Vabishchevich, P.N. 2020 *Approximation of a fractional power of an elliptic operator*. Linear Algebra Appl. 27, e2287.
[13] Vabishchevich, P.N. 2018 *Numerical solution of time-dependent problems with fractional power elliptic operator*. Comput. Meth. in Appl. Math. 18, no. 1, 111–128.
[14] Aceto, L. and Novati, P. 2022 *Exponentially convergent trapezoidal rules to approximate fractional powers of operators*. J. Sci. Comput. 91(2), 55.

* * *

Behaviour of Diffusion Process under Space-Fractional Derivative Using Spectral Method

H. Bansu, S. Margenov

Over the last few decades, fractional calculus has managed to catch extensive attention from many researchers in various different fields. Thus, studies on fractional equations from both numerical and theoretical aspects are increasing, see [1] and references therein. Fractional differential equations have been implemented to model plenty of phenomena in many research areas such as heat transfer, wave propagation, control theory, fluid flows and so on. Fractional differential equations, unlike classical differential equations, can more accurately describe various phenomenons and therefore able to improve the inadequacy of classical models in expressing objective reality.

One of the most important applications of fractional differential equations is to model anomalous diffusion in the cases of sub-diffusion and super-diffusion. As a generalization of the classical diffusion equations, the fractional order diffusion equations have been used in a large number of applications where anomalous diffusion occurs. For example, this is because heat diffusion plays a central role in many real-world phenomena related to thermal science, materials science, chemical science, and biological science.

The present study is devoted to the numerical solution of the diffusion equation. In studying the behavior of the fractional diffusion process, Caputo generalized fractional derivative is used in the generalized space-fractional diffusion equation.

Because of their importance in representing many anomalous phenomena, there are many authors who have contributed significantly to the solution of fractional diffusion problems. Zheng et. al. [2] proposed spectral approximation method for fractional diffusion equations. Mainardi et. al. [3] obtained the fundamental solution of the space-time fractional diffusion equation. Ilic et. al. [4] provided a method based on a matrix representation of the fractional-in-space operator to approximate a fractional-in-space

diffusion equation in a bounded domain. Saadatmandi and Dehghan [5] proposed approximation techniques based on the shifted Legendre-tau idea to solve a class of fractional diffusion equations. Feng et. al. [6] used finite element method to solve fractional diffusion equation. Salehi et. al. [7] implemented method of lines and splines for numerical solution of space fractional diffusion equation. Issa et. al. [8] considered numerical approach for solving space fractional diffusion equation using shifted Gegenbauer polynomials.

Here we first consider the standard (local) parabolic equation

$$\frac{\partial u(x,t)}{\partial t} = \frac{\partial^2 u(x,t)}{\partial x^2}, \;\; 0 < x < 1, \; 0 < t < t_f \tag{1}$$

with initial condition $u(x,0) = u_0(x), \; 0 < x < 1$, and homogeneous boundary conditions $u(0,t) = 0$ and $u(1,t) = 0$. The spectral method in space (see, e.g., [9]) is implemented in the time stepping scheme developed. The accuracy of the solver is verified numerically. A test problem with an initial condition $u_0(x) = \sin(\pi x)$ and a known exact solution $u(x,t) = e^{-t^2}\sin(\pi x)$ is used to this goal.

We then turn to the target topic of this study and consider the space-fractional time-dependent problem in the form

$$\frac{\partial u(x,t)}{\partial t} = \frac{\partial^\beta u(x,t)}{\partial x^\beta}, \;\; 0 < x < 1, \; 0 < t < t_f \tag{2}$$

keeping the initial and boundary conditions $u(x,0) = u_0(x)$, $u(0,t) = 0$ and $u(1,t) = 0$. Here $\partial^\beta u(x,t)/\partial x^\beta$, $\beta \in (1,2)$, is the Caputo fractional derivative, thus defining the explored case of sub-diffusion.

The fractional diffusion is non-local. The corresponding discrete operators (matrices) are dense. Thus, the implementation of the time stepping algorithm requires solving dense matrix linear systems at each time step. This is a rather time-consuming task with a computational complexity of the order of $O(N^3)$, N being the number of unknowns, assuming a Gaussian-type solver is used.

The spectral method used in the case of standard diffusion is now applied to avoid dense matrix computations in the case of fractional diffusion. Thus, if a fast Fourier transform is applied to fractional-order matrix operations, the computational complexity can be reduced to $O(N \log N)$. In particular, the influence of decreasing fractional order β is investigated, which case corresponds to stronger anomalous sub-diffusion.

The results obtained by the proposed spectral method for the considered problem (1) and (2) are plotted in the following figure. Here we have taken 400 points in spatial direction and 100 points in temporal direction. The final time is $t_f = 0.25$ and figure is plotted at mid time i.e. at $t = 0.125$. We can observe, that the numerical solution obtained by the proposed method shows good aggregation with the known exact solution. Further, the temperature is almost inversely proportional to the order β i.e. the temperature keeps on increasing for the decreasing fractional order β which characterizes the anomalous diffusion.

Our interest in developing efficient numerical methods for the space-fractional parabolic equation is motivated in particular by the possibility to apply the obtained results to the fractional Penns bioheat model. The generalization of the proposed approach to the case of a multidimensional domain in space is a topic of future research with potentially great impact.

Acknowledgements

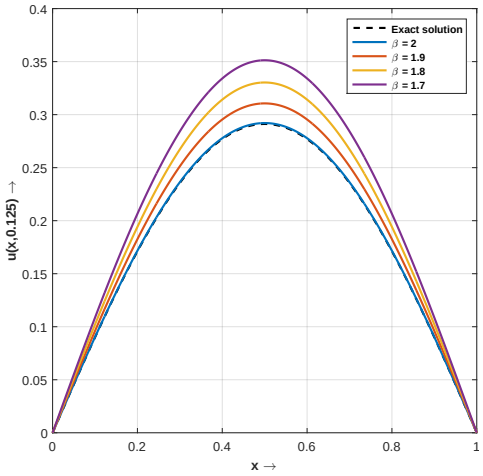

Figure 1: Temperature profile for (1) and (2) along the distance at $t = 0.125$ under the influence of decreasing β.

The first author is supported by Early-stage and Postdoctoral researchers National Programme 2 - Bulgarian Academy of Sciences. Our work is also partially supported by the Bulgarian National Science Fund under grant No. KP-06-N72/2.

References

[1] A. Kochubei, Y. Luchko, V. E. Tarasov, I. Petráš, Handbook of fractional calculus with applications, Vol. 1, de Gruyter Berlin, Germany, 2019.
[2] X. Zheng, V. Ervin, H. Wang, Spectral approximation of a variable coefficient fractional diffusion equation in one space dimension, Applied Mathematics and Computation 361 (2019) 98–111.
[3] F. Mainardi, Y. Luchko, G. Pagnini, The fundamental solution of the space-time fractional diffusion equation, arXiv preprint cond-mat/0702419 (2007).
[4] M. Ilic, F. Liu, I. Turner, V. Anh, Numerical approximation of a fractional-in-space diffusion equation, i, Fractional Calculus and Applied Analysis 8 (3) (2005) 323–341.
[5] A. Saadatmandi, M. Dehghan, A tau approach for solution of the space fractional diffusion equation, Computers & Mathematics with Applications 62 (3) (2011) 1135–1142.
[6] L. Feng, P. Zhuang, F. Liu, I. Turner, Y. Gu, Finite element method for space-time fractional diffusion equation, Numerical Algorithms 72 (2016) 749–767.
[7] Y. Salehi, M. T. Darvishi, W. E. Schiesser, Numerical solution of space fractional diffusion equation by the method of lines and splines, Applied Mathematics and Computation 336 (2018) 465–480.
[8] K. Issa, B. M. Yisa, J. Biazar, Numerical solution of space fractional diffusion equation using shifted gegenbauer polynomials, Computational Methods for Differential Equations 10 (2) (2022) 431–444.
[9] S. Harizanov, R. Lazarov, S. Margenov, A survey on numerical methods for spectral space-fractional diffusion problems, Fractional Calculus and Applied Analysis 23 (6) (2020) 1605–1646.

* * *

A Multi-Mesh Adaptive Scheme for the Spectral Fractional Laplacian

R. Bulle, A. Bespalov

Fractional powers of the Laplacian operator are important tools in the modeling and study of non-local phenomena. Several numerical challenges arise from the discretization of these operators due to

their non-local nature. One way to discretize these problems is by using a rational scheme combined with a finite element method. Rational schemes allow to reformulate the fractional Laplacian problem into a set of independent standard (i.e. non-fractional) reaction-diffusion problems.

In this talk we describe a novel multi-mesh finite element method for the spectral fractional Laplacian discretized via a rational scheme. This method uses a strategy introduced by Bank and Weiser to estimate the finite element discretization error (in L^2 norm) on all the cells of the meshes. Thus, it determines the minimal set of cells to be refined across all the meshes using a cross-mesh Dörfler's strategy.

With this method, we are able to estimate and evenly distribute the finite element discretization error across the meshes and avoid over-refinement, leading to a large gain in the computational cost of the overall method compared to the single mesh case.

We show the benefits of our method compared to the single mesh method with several numerical evidences generated with the T-IFISS Matlab software.

* * *

Hybrid Classical-Quantum Optimization with Inequality Constraints

H. Djidjev

We describe two new approaches for solving optimization problems with inequality constraints on quantum annealers such as the D-Wave quantum systems. As an illustration, the methods are applied to the set cover problem (SCP), a well-known NP-hard problem with many applications whose formulation typically involves a large number of inequality constraints. Constraints, and in particular inequality constraints, make it difficult to implement optimization problems on quantum annealers using standard methods.

The first approach utilizes the augmented Lagrangian method (ALM) to incorporate the inequality constraints. ALM combines the penalty method with the method of Lagrangian multipliers. The inequality constraints are incorporated into the objective function as an additive penalty term involving the constraints and Lagrangian multiplier parameters. An iterative procedure is then used to update the multiplier values and penalty coefficient in order to compute a single objective function that encodes both the original objective and all the constraints.

To apply this method to SCP, we encode its objective function as a QUBO (quadratic unconstrained binary optimization) problem and deal with the constraints using the ALM approach. This allows the constrained SCP to be solved on D-Wave quantum annealers, which can directly only solve unconstrained QUBO formulation.

The second approach formulates the SCP directly as a higher-order unconstrained binary optimization (HUBO) problem. Compared to QUBO functions, which are quadratic, HUBO formulations can use higher-degree monomial terms. Solving a HUBO formulation on a D-Wave quantum annealer requires first converting it into a QUBO, which can be done using standard software tools.

We experimentally analyze the methods on random SCP instances. For the ALM method we use a quantum annealing implementation (AL_QA) and a simulated annealing classical implementation (AL_SA). Similarly, for the HUBO version we implement a quantum annealing version (HUBO_QA) using D-Wave's HUBO-to-QUBO converter, and a simulated annealing classical version (HUBO_SA) that operates directly on the HUBO without conversion. The results show that both the ALM and HUBO approaches significantly outperform the standard slack variable method for handling constraints on D-Wave machines. The HUBO approach finds the highest quality solutions overall. However, the ALM method is more generalizable to other constrained problems beyond SCP. Moreover, the quantum annealing implementations (AL_QA and HUBO QA) are able to find better solutions than their simulated

annealing counterparts (AL_SA and HUBO_SA), particularly as the problem size increases. For the largest instances tested with up to 175 sets, both quantum methods could embed around 100% of the problems on the D-Wave Advantage 1 quantum annealer.

Key advantages of the proposed approaches include their ability to handle large numbers of inequality constraints without introducing too many auxiliary variables, and their better scalability compared to the standard method.

* * *

European fuel map used in simulation for Bulgarian test case

N. Dobrinkova

Abstract

Fire behaviour modelling is a time consuming process that requires a lot of preliminary work for data preparation, before a simulation is run. European fuel map created under the project FirEUrisk was tested in a simulation for a fire that was active in the period 10-14 August 2022 in south-east Bulgaria nearby the village of Razdel - municipality of Elhovo. This was first attempt for calibration of European fuel map in Bulgaria.

1 Introduction

The Razdel village fire started 2km in south east direction towards the municipality of Elhovo. The active fire front propagation was recorded by the local authorities in the period 10-14 August 2022. Between 15 and 17 August 2022 smaller events near by the suppressed fire front were also noted, but were considered as smaller separate events. The ignition occurred on the morning of August 10th. The alert was given at 11:00 of the same day, and the fire was detected by the passage of the Terra MODIS at 11:26. Final total burned area was 797 ha, where 560 ha were forest areas, and 237 ha were grasslands and pastures. The size of the burned forest territory makes that fire the largest forest fire in Bulgaria in the year 2022. The fire of Razdel village did not have an impact on residential zones, it affected considerable areas of NATURA 2000 and there was the risk of the fire crossing the Bulgarian - Turkish border.

The area of Elhovo municipality is affected regularly by small or large wild land fires. Since 2000, more than 35 wild land fires have been recorded within the municipal territory, which led to 5,640 ha burned area in total throughout the years. The three villages that were affected by the fire of 2022 had experienced seven other wild land fires, in the period from 2000 until 2021, with a total burned area of 2,200 ha.

There are a few dams located in the northern part of the Elhovo municipality and almost none in the South. This, combined with the higher degree of terrain roughness, was a prerequisite for the difficulties in finding water for fire fighting needs. On Fig. 1 we have the final burned shape of the fire spread and the location of the fire on the Bulgarian country map.

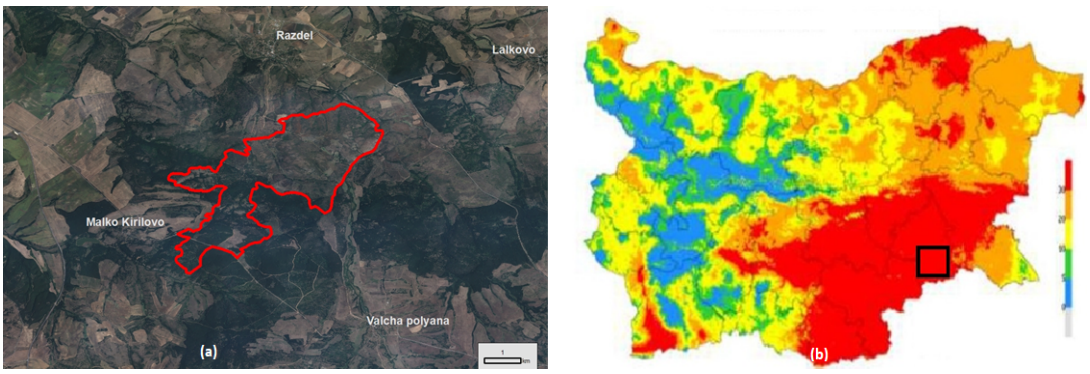

Figure 1: Location of the Razdel Fire in south-east Bulgaria:(a) burned shape of the fire perimeter and (b) fire location on the Bulgarian country map.

2 Meteorological conditions

The forecast for August 10th 2022, provided by the National Institute for Meteorology and Hydrology (NIMH) [1], was for sunny weather with a clear sky. The winds were strong from north-northeast with a speed of 6 to 9 m/s reaching up to 15 m/s. The forecast for the daily max temperatures was 32°C to 34°C for the region, where the Razdel Fire occurred. The relative humidity was above 40%, which in windy areas is a very dangerous combination that can cause a fast fire spread.

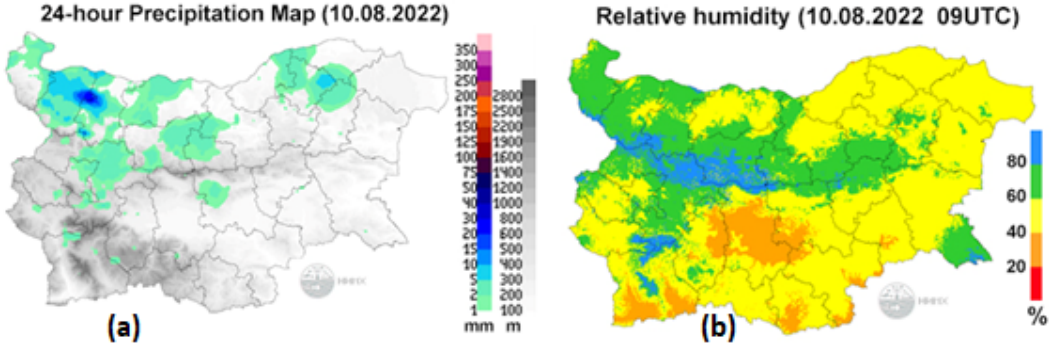

Figure 2: Meteorological conditions for August 10th, 2022: (a) 24-hour precipitation (mm); (b) Relative humidity (data from NIMH [1])

The wind had an important role in the fast fire perimeter spread of the Razdel Fire. As shown in Figure 3a, on August 10th, the wind was from the northwest reaching in the afternoon 10-15 m/s. This led to the fast spread of the fire in the southwest direction, but stopping the fire after reaching the top of the hill where it turns to the north (close to the village of Razdel). Figure 3b, represents the satellite image from Sentinel 2 taken from 10:55 on August 10th, just a few minutes after the fire started.

3 Simulation results

The meteorological conditions and the local geography were very favourable for the Razdel fire occurrence and its spread. The data about the fire simulation was collected from the field and transformed into GIS (Geographical Information Systems) layers [2,3]. The vegetation fuel data was used as a downscaled FirEUrisk 1km fuel map of Europe to a 100m resolution [4].

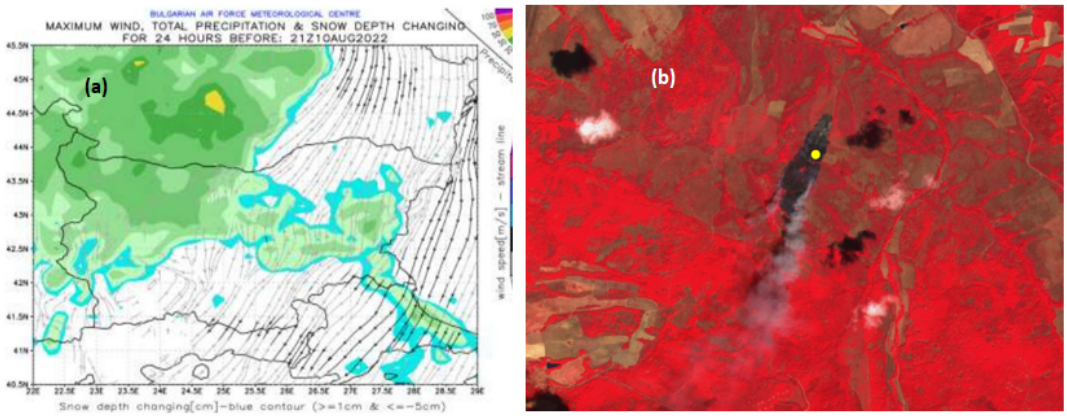

Figure 3: Wind influence on fire on August 10th: (a) Wind forecast for August 10th (data from NIMH); (b) Fire distribution on August 10th at 10:55, with a yellow dot, is presented the assumed start of the fire and the smoke shows the direction of the wind (data by Sentinel 2)

The resized 100m fuel map was run in FlamMap/FARSITE simulation. The final result of the fire run was relatively close to reality first few hours fire spread and extreme fire propagation after that. Possible reason for this can be the way the 1km downscaling was done for the grasslands, which can explain the fast fire front propagation. Fig. 4 presents the simulation result.

4 Conclusions

Typically, in Bulgaria, the hottest month of the year is August. This is especially true for the south-east regions of the country. During August 2022, 92 fires were registered in the country which is almost 25% of all the fires in Bulgaria for that year. The fire of Razdel village was a wind driven fire that occurred in very dry windy zone with pasture works nearby as cause for its ignition. Simulation results with European resized fuel map from 1km to 100m showed that extra work on fuels need to be done in order more realistic simulations to be observed.

Acknowledgements

This paper has been supported by the Bulgarian National Science Fund project with number KP-06-COST/23 and the European Union's Horizon 2020 Project "Developing a Holistic, Risk-Wise Strategy for European Wildfire Management" with acronym: FirEUrisk and Grant Agreement number:101003890.

References

[1] URL: http://www.weather.bg/pojaroopasnostPlus/index.php/ - A daily fire danger map of Bulgaria provided as online service in NIMH. Link accessed on 15 July 2023.

[2] Dobrinkov G., Dobrinkova N., "Input Data Preparation for Fire Behavior Fuel Modeling of Bulgarian Test Cases (Main Focus on Zlatograd Test Case).", 10th International Conference on "Large-Scale Scientific Computations" LSSC'15, Sozopol 8-12 June 2015, Lecture Notes in Computer Science 9374, ISSN 0302-9743, ISSN 1611-3349 (electronic), ISBN: 978-3-319-26519-3, DOI 10.1007/978-3-319-26520-9, Springer Germany, pp. 335–342, 2015.

[3] Dobrinkova N., Hollingsworth L., Heinsch F.A., Dillon G., Dobrinkov G., "Bulgarian fuel models developed for implementation in FARSITE simulations for test cases in Zlatograd area". (E-proceeding:http://www.treesearch.fs.fed.us/pubs/46778) Wade DD and Fox RL (Eds), Robinson ML (Comp) (2014) 'Proceedings of 4th Fire Behavior and Fuels Conference', 18-22 February 2013, Raleigh, NC and 1-4 July 2013, St. Petersburg, Russia. (International Association of Wildland Fire: Missoula, MT), p.513 - p.521.

[4] Aragoneses, E., García, M., Salis, M., Ribeiro, L. M., and Chuvieco, E.: Classification and mapping of European fuels using a hierarchical, multipurpose fuel classification system, Earth Syst. Sci. Data, 15, 1287–1315,

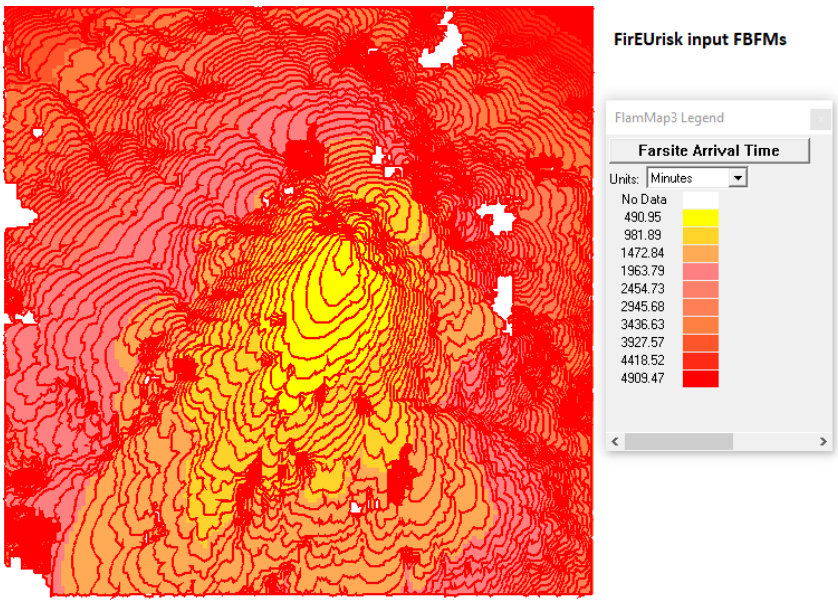

Figure 4: FireEUrisk fuel map on 100m resolution used in FlamMap/FARSITE run of Razdel fire

https://doi.org/10.5194/essd-15-1287-2023, 2023.

* * *

Generalized Net for Diabetics Evacuation After Earthquake

S. Fidanova, K. Atanassov, L. Kirilov, V. Ivanov

1 Introduction

When a natural disaster occurs, such as an earthquake, flood, etc., there are groups of people who cannot cope alone and need additional help. One such group is diabetics. In addition to the main disease, they often have various complications. Even if a diabetic is in good physical condition and able to evacuate the disaster site by himself, he needs additional care, such as regular insulin and other medications. In this research, we focus on the evacuation of diabetics after an earthquake. We propose a model of evacuation, base on Generalized Net (GN) aparatus [1,2]. The goal is to be able to play out a variety of scenarios and make the most appropriate decision given the specific situation. The purpose of the model is to support the local authorities for preliminary preparation and training of the staff who will provide assistance, as well as for a quick and adequate response after the occurrence of an earthquake.

2 Generalised Nets

In this work we propose a model for diabetics evacuatio after earthquake with a help of Generalizet Nets. GN are a very powerful tool for modeling a variety of processes. They were proposed 40 yera ago by K. Atanassov [1,2]. Later they were used by a lot of scientists for describing and modeling different

processes and algorithms [3–5]. They are very suitable for the description of inhomogeneous complex processes.

The structure of GN consists of **tokens**, which act as information carriers and can occupy a single place at every moment of the GN execution. The tokens pass through the transition from one input to another output place. The tokens' movement is governed by conditions (predicates), contained in the index matrix (see, [6]) of the transition. The information carried by a token is contained in its **characteristics**, which is obtained by a **characteristic function**. Every place possesses at most one characteristic function, which assigns new characteristics to the incoming tokens. Tokens can split and merge in the places. A transition can contain m input and n output places where $n, m \geq 1$ (see Figure 1) and m and n can be different.

With the help of GN, one can first describe the framework of the considered process, then replace each transition with a new network and thus add new details to the model. This makes it possible to describe a given process in depth and prevents important components from being omitted.

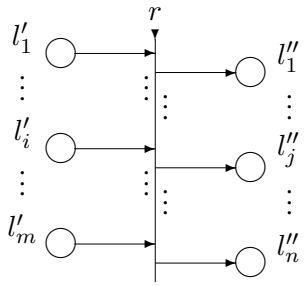

Figure 1: The form of transition in a GN

In our application, every particular situation will be reprezented by a transition. The tokens which entry the transition have different charachtersitics. In the transition they interact with each other and can change their characteristic.

3 GN for Diabetic Evacuation

Earthquakes are one of the most destructive natural phenomena. In order to preserve the life and health of people with physical needs, special plans and models are made for their removal from the place of destruction and providing them with the necessary additional medical assistance. In our previous model, we estimate damage and casualties. Data from it can be used in the current evacuation model [4].

The input data for our model are adresses of the diabetics and what co-morbidities they have. We need data about the building they live in. This data can be taken from our previous model of the consequences of an earthquake [4]. It is necessary to know what equipment is available in hospitals in the region and in evacuation centers. Thus, a preliminary plan can be made to refer the diabetic patient to the appropriate hospital or center depending on his specific needs.

In the second transition, diabetics will be grouped according to their comorbidities. This will help in properly directing them to an appropriate health facility or place of assistance.

The third transition will assess what additional injuries they may have sustained during the earthquake such as fractures and burns. As we know, in diabetics, wounds heal more slowly, and there may be a problem with the more important blood clotting. This should be taken into account when providing medical assistance.

In the fourth transition, diabetics will be allocated to hospitals and centers depending on their injuries and concomitant diseases.

The most important striking factors in earthquakes are traumatic and thermal. A team of scientists from the Trakia University, Stara Zagora, are developing new forms for topical application to treat wounds and burns, which could be applied in such situations.

4 Conclusion

Earthquakes are difficult to predict, but advance preparation can be crucial. When we have information about diabetics, their comorbidities, as well as information about the homes they live in and the likelihood of them getting injured and burned, local authorities and medical institutions can be prepared in advance and react adequately. Such type of models will lead to saving human lives and reducing casualties and disability when a disaster occurs.

Acknowledgements
The authors from IICT are supported by the National Scientific Fund of Bulgaria grant DFNI KP-06-N52/5 and by the project OMNIA grant BG05M20P011-2.016-0007 financed by the Science and Education for Smart Growth Operational Program and co-financed by European Union. Veselin Ivanow is supported by the European Union-NextGenerationEU, through the National Recovery and Resilience Plan of the Republic of Bulgaria, project No BG-RRP-2.004-0006.

References
[1] Atanassov, K.: Generalized Nets. World Scientific. Singapore, London, 1991.
[2] Atanassov, K.: On Generalized Nets Theory. "Prof. M. Drinov" Academic Publishing House. Sofia. (2007)
[3] Krawczak, M. Multilayer Neural Systems and Generalized Net Models. Akademicka Oficyna Wydawnicza EXIT, Warszawa, 2003.
[4] Fidanova, S., K. Atanassov,L. Kirilov, V. Slavova, V. Ivanov. Generalized Nets Model of the Consecances of Earthquake, Lecture Notes in Networks and Systems, 658, 2023, 281-292.
[5] Atanassov. K. Generalized Nets and Intuitionistic Fuzziness in Data Mining. "Prof. Marin Drinov" Academic Publishing House, Sofia, 2020.
[6] Atanassov, K.: Index Matrices: Towards an Augmented Matrix Calculus. Springer, Cham (2014)

* * *

Advanced Computing in Analysis of the Climate Changes Impact

G. Gadzhev, V. Ivanov, I. Georgieva, K. Ganev

1 Introduction

The global warming is a consequence of ongoing changes of the circulation of the system ocean-atmosphere, which lead not only to temperature changes, but also to the spatial/temporal distribution of precipitation, hence the global water budgets, to changes of the characteristics and spatial/temporal distribution of unfavorable and catastrophic events (drought, storms, hail, floods, fires, sea waves, soil erosion, etc.). The changes will have their influence on ecosystems, on all sectors of the economy and every aspect of human activity and quality of life. The regional/local characteristics of the climate changes cannot be predicted correctly by the global models. The present paper briefly describes the results of activities [1], [2], [3], [4] aiming to develop adequate methodology and implementing it to produce reliable, comprehensive and detailed evaluations of possible regional/local climate changes and their consequences for different global change scenarios. The main scientific challenges are the multi-scale

nature of the processes and the complex interactions of different scale phenomena and basic mechanisms and pathways trough which regional/local climate change specifics and their impact on environment and human activities are formed.

2 Methodology and input data

The studies are carried out by the means of computer simulations. The regional climate model, applied for the purpose is RegCM version 4.4 [5]. The model is driven by initial and boundary conditions from the ERA-Interim Reanalysis data with horizontal resolution 1.5° x 1.5° with time step 6 hours and 37 vertical levels [6].

16 numerical simulations scenarios for different model configurations with model grid in Lambert Conformal Conic projection were defined. The RegCM model simulations are done with spatial resolution 10 kilometers, time step 25 seconds and 27 vertical levels in hydrostatical mode. By comparison of the simulated results with measured data the following RegCM configuration is chosen as optimal: - Land-surface scheme – Biosphere-Atmosphere Transfer scheme; - Horizontal resolution 20 km and time step 30 sec.; - Boundary layer parameterization scheme – Holtslag scheme; - Large scale moisture parameterization scheme – Subgrid Explicit Moisture scheme; and - Convective parameterization scheme – Grell scheme.

Three Emission scenarios, which provide rough estimate of the radiative forcing in the year 2100, relative to preindustrial conditions are considered: RCP2.6 scenario - peak of the radiative forcing in the middle of 21th century and returning to 2.6 W.m^{-2} by 2100; RCP4.5 scenario - initial rising of the radiative forcing with stabilization on 4.5 W.m^{-2} after 2100; RCP8.5 scenario suggest rising pathway with 8.5 W.m^{-2} in 2100. The simulations are performed for the following time periods: ***Reference period*** (”control run” CR) – 1975-2005 years; ***Near future*** (NF) – 2021-2050 years; ***Far Future*** (FF) – 2071-2099 years. The fact that the regional/local phenomena really do have an impact on the climate characteristics is soundly demonstrate in Figure 1.

Figure 1: The 10^{th}, 25^{th}, 50^{th}, 75^{th} and 90^{th} percentiles of the mean temperature [°C] for the reference period from E-OBS (first row). And RegCM (second row), as well as the bias between them (third row).

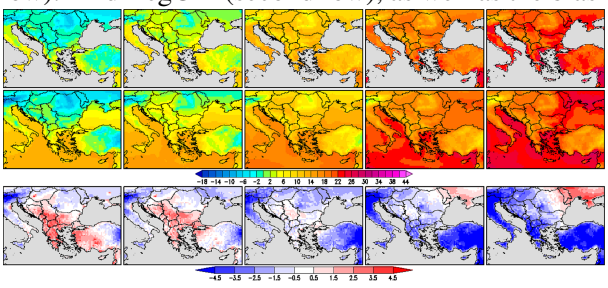

3 Forecast of the future regional/local changes of the climate

The climate has many characteristics, but the temperature and the precipitation are among the most important and perhaps the most demonstrative one. So in Figure 2 and Figure 3 are shown plots of the future changes of the mean temperature and precipitation for NF according to the 3 global change scenarios. Generally, the projected temperature increases from RCP2.6 to RCP8.5, more clearly in the far future and is remarkable bigger for far future compared with near future for the RCP8.5 scenario, which agrees with the prevailing number of the modern evaluation studies is the spatial dominating positive signal. The warming will be the general tendency in the 21thcentury. Such warming is the

Figure 2: Absolute change of the multiyear means for the NF of the mean temperature [°C] for DJF, MAM, JJA and SON as well as annual (from left to right) for RCP2.6 (first row), RCP4.5 (second row) and RCP8.5 (third row).

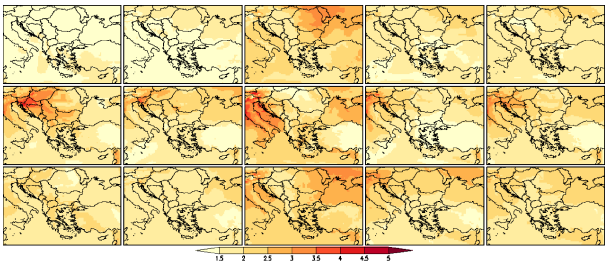

Figure 3: Relative change [%] of the multiyear means for the NF of the mean daily precipitation summ for DJF, MAM, JJA and SON as well as annual (from left to right) for RCP2.6 (first row), RCP4.5 (second row) and RCP8.5 (third row).

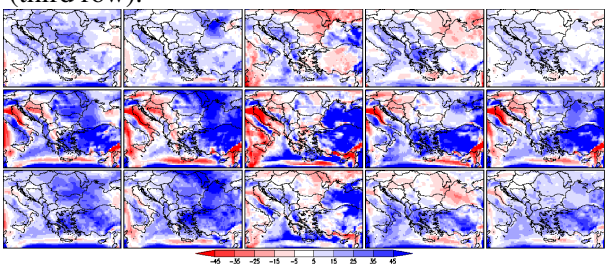

natural continuation of the already detected from the analysis of the historical time series for the previous decades, tendency. The maximum values are obtained for the summer, which is prerequisite for more frequent and/or long extreme hot episodes with all negative consequences. As expected, the projected precipitation change is more complex, with expected summer months reduction, which could amplify the negative impact of the expected hotter climate.

4 Some climate indices

An important task in the modern climatology is to assess extreme climate and weather events alongside various aspects of the mean climate. The climate indices (*Cis*), computed from daily minimum (*tn*), mean (*tg*), maximum (*tx*) and annual basis (*tb*) temperature, are relatively simple, but statistically consistent, quantitative indicators of the climate extremes and, subsequently, widely used. Space heating and cooling is responsible for a large fraction of European energy use. Heating degree days (HDDs) and cooling degree days (CDDs) are proxies for the energy demand needed to heat or cool, respectively, a home or a business. Both variables are derived from daily measurements and/or estimations of *tn*, *tg*, *tx* and *tb*. The effects of climate change clearly appear in agriculture and forestry in the considered domain. Production of these sectors is strongly influenced by the growing season length (GSL), accumulated active and effective temperatures (AAT and AET). These quantities are valuable agro-meteorological indicators relevant for cultivated plants phenology and active growth of crops [2]. According ETCCDI, the GSL is the annual count between first span of at least 6 days with $tg \geq tb$ and first span after July 1 of (at least) 6 days with $tg \leq tb$. The threshold temperature *tb* is 5°C for the cold-tolerant and 10°C for the thermophile species. In the present study, due to the geographical location of the region, we deal with *tb*=10°C. As the GSL, the AAT and AET are calculated also on annual basis and are defined as:
where *iu* is the day of year (DOY) of the start, and *io* is the end of the GSL. The most apparent result of the analysis on Figure 4 is that the distribution patterns of all indices are practically identical in the both

$$AAT = \sum_{i=iu}^{i=io} tg(i), \quad AET = \sum_{i=iu}^{i=io} (tg(i) - tb), \quad \text{if } tg(i) > tb$$

scenarios, with relatively small graduate increase from RCP2.6 to RCP4.5. The climate change results in definite evolution of the considered indicators – distinct and spatially dominating increase of the "warm" indicators (CDD, GSL, AAT and AET) and decrease of the "cold" one (i.e. the HDD).Figure 5 shows the fields of the MM of the HDD, CDD, GSL, AAT and AET for the FF. The distribution of all indicators is spatially coherent, as in the similar Figure 2. Again, there is gradual increase of the tendencies from RCP2.6 to RCP8.5 but in this case the difference between both scenarios appears more significant.

Figure 4: Multiyear means for the NF of HDD, CDD, GSL, AAT and AET from RegCM, RCP2.6 (first row), RCP4.5 (second row). The relative changes with respect to the near past (in %) for RCP2.6 and RCP4.5 are shown on the third and fourth row correspondingly.

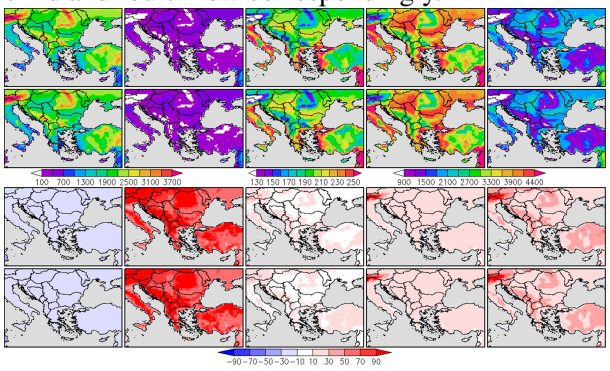

Figure 5: Same as Figure 4 but for the FF

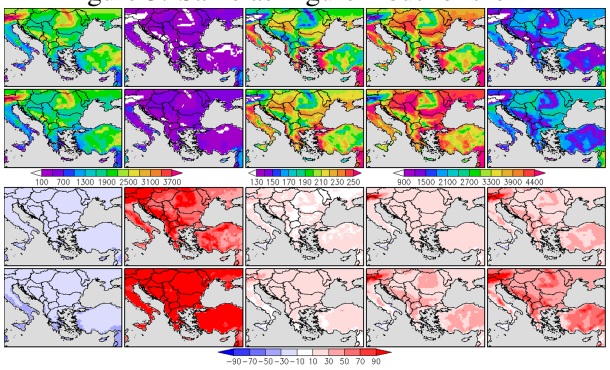

Acknowledgements

This work has been carried out in the framework of the National Science Program "Environmental Protection and Reduction of Risks of Adverse Events and Natural Disasters", approved by the Resolution of the Council of Ministers N 577/17.08.2018 and supported by the Ministry of Education and Science (MES) of Bulgaria (Agreement N D01- 27/06-02-2024)

References

[1] Chervenkov, H., Ivanov, V., Gadzhev, G. and Ganev, K., 2017, Sensitivity study of Different RegCM4.4 model set-ups – recent results from the TVRegCM experiment. CYBERNETICS AND INFORMATION TECHNOLOGIES, Vol. 17, No 5, pp. 17-26

[2] Chervenkov, H., Gadzhev, G., Ivanov, V. and Ganev, K., 2021, Degree-days and Agro-meteorological Indices in CMIP5 RCP8.5 Future Climate - Results for Central and Southeast Europe, Studies in Systems, Decision and Control, Vol. 361, pp. 19 – 30, https://doi.org/10.1007/978-3-030-70190-1_2

[3] Gadzhev, G., VIvanov, V., Ganev, K., and Chervenkov, H., 2018, TVRegCM Numerical Simulations - Preliminary Results, Lecture Notes in Computer Science (including subseries Lecture Notes in Artificial Intelligence and Lecture Notes in Bioinformatics), Vol. 10665 LNCS, pp. 266-274.
[4] Ivanov V., Gadzhev G., 2022, Behavior and Scalability of the Regional Climate Model RegCM4 on High Performance Computing Platforms. In: Lirkov I., Margenov S. (eds) Large-Scale Scientific Computing. LSSC 2021. Lecture Notes in Computer Science, Vol. 13127. Springer, Cham, pp. 124-131, https://doi.org/10.1007/978-3-030-97549-4_14
[5] Giorgi, F. et all., 2012, RegCM Model Description and Preliminary Tests over Multiple CORDEX Domains. Clim. Res., Vol. 52, pp. 7-29 . https://doi.org/10.3354/cr01018
[6] Dee, D. P., et al., 2011, The ERA Interim Reanalysis: Configuration and Performance of the Data Assimilation System. Q. J. R. Meteorol. Soc., Vol. 137, pp. 553-597. https://doi.org/10.1002/qj.828

* * *

Mathematical Modeling and Numerical Simulation on Tornado Dynamics

X. Guo, J. Cao

Tornadoes have been worldwide observed, and more frequently reported in the United States and Canada. Compared to a straight-line wind, a tornadic flow is much more complex, since it is a type of airflow that essentially combines translational, vertical, and rotational velocities, and all components have to be considered in a meaningful investigation. As the study of tornado dynamics through field observations or laboratory experiments tends to be time-consuming, laborious, and expensive, more research efforts have been made in the direction of mathematical modeling and numerical simulations. Historically, Wilson (*cf.* [1]) first applied a two dimensional (2D) tornado model to examine the effects of tornadoes on rectangular-shaped buildings. Lewellen et al. (*cf.* [2], [3]) employed a three-dimensional (3D) large eddy simulation (LES) turbulence model to investigate the dynamics of a tornado-like vortex near the surface with particular attention paid to the turbulent flow characteristics in the corner region. Natarajan and Hangan (*cf.* [4]) also used LES model to study the effects of surface roughness and translation on the mean tangential velocity of the tornadic wind for different swirl ratios. On the other hand, tornado-induced wind loadings exerted on constructions have been a practical topic. Based upon the Rankine-combined vortex model (RCVM), Selvam et al. (*cf.* [5,6]) used the finite difference discretization of the Navier-Stokes (N-S) equations to conduct a series of studies focusing on the tornado-induced loadings on 2D sections of a cylinder and multi-cubic buildings, followed by some 3D cases at elevated Reynolds numbers also with the aid of LES (*cf.* [7]).

However, most aforementioned computational tornado dynamics studies mainly relied on conventional numerical methods, through which the velocity boundary conditions have to be updated at all times due to the dynamic nature of tornado. To overcome this tedious updating process, Guo et al. (*cf.* [8,9]) utilized the "*relative motion*" principle to re-formulate RCVM for modeling two-dimensional (2D) tornado-building interaction with the aid of immersed boundary (IB) method, resulting in a "*virtual*" scenario in which the building "*moves*" at a velocity that is the negative of the translation velocity of the tornado, while the background airflow has only a rotational component about its "*pinned*" center. Thus, as long as the computational domain is large enough for its outer boundary to get practically unaffected by the inner flow evolution induced by the "*virtual translation*" of the building, the time-dependency and, hence, the kinematic condition updating process at the outer boundary of the computational domain can be effectively eliminated.

This study aims to extend the 2D tornado simulation framework (*cf.* [8,9]) to the 3D version by taking the vertical velocity component into account. This new development combines the direct forcing

IB approach with a centered finite difference scheme of high accuracy to solve the 3D N-S equations coupled with the LES turbulence model in order to better simulate the tornadic flow at relatively high Reynolds numbers. The advantage of this framework was discussed in terms of computational efficiency, accuracy, and simplicity (*cf.* [10]). Considering the large computational domain along with fine grid resolution required by 3D tornado simulations, this framework has been adapted to be portable on massive parallel computing platforms via Message Passing Interface (MPI) techniques (*cf.* [10]).

In terms of the governing equations, he momentum and mass conservation principles are represented by the Navier-Stokes equations, which have the following form for an incompressible fluid:

$$\rho\left(\frac{\partial\vec{V}}{\partial t}+(\vec{V}\cdot\vec{\nabla})\vec{V}\right)=-\vec{\nabla}p+\mu\vec{\nabla}^2\vec{V}+\vec{f} \tag{1}$$

and

$$\vec{\nabla}\cdot\vec{V}\ =0 \tag{2}$$

respectively. In Eqs. (5) and (6), $\vec{V}(\vec{x},t)=\{u(\vec{x},t),v(\vec{x},t),w(\vec{x},t)\}^t$ is the fluid velocity, $p(\vec{x},t)$ is the pressure, and ρ is a constant density ($\rho=1$) in the present framework; $\vec{f}(\vec{x},t)$ is the external forcing term caused by the interaction between the air and the immersed virtually translating building as a result of the re-tailored RCVM. The simulations are performed using Incompact3d, an open-source software package developed mainly by Laizet & Lamballais (*cf.* [11]). All governing equations are solved on a collocated velocity grid via the six-order central compact finite different scheme (*cf.* [12]), while the pressure is on a staggered grid. While time integration unfolds, continuity is verified at the end of each sub-time step by solving a Poisson equation of pressure. This Poisson equation is solved through a spectral solver to reduce the demand of computations incurred by the high-order discretization along with iterative schemes. The massive parallelism embedded in the code was realized through an MPI implementation based on pencil domain decomposition strategy (*cf.* [10]).

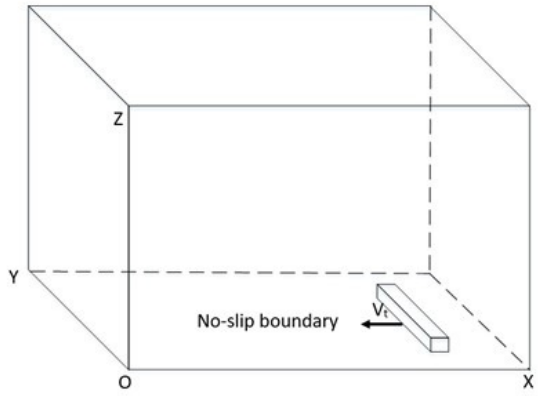

Figure 1: Schematic of the computational domains

Figure 1 illustrates the computational domain with $L_x\times L_y\times L_z=24\times16\times16$. The length (in the *x*-direction) and the height (in the *z*-direction) of the prism are equal to 1, and the depth (in the *y*-direction) of prism is set at 12. The translation velocity remains one unit. The Reynolds number based on the height of the prism is Re=10000. The dimensionless force coefficients in all three directions are defined as:

$$C_x=\frac{F_x}{\frac{1}{2}\rho V_t^2 S_x} \tag{3}$$

$$C_y=\frac{F_y}{\frac{1}{2}\rho V_t^2 S_y} \tag{4}$$

$$C_z = \frac{F_z}{\frac{1}{2}\rho V_t^2 S_z} \tag{5}$$

where F_x, F_y, F_z and S_x, S_y, S_z are the components of the resultant force and the projection areas in the three directions, respectively.

Fig. 2 illustrates the evolution of the force coefficients in all three directions C_x, C_y, and C_z. Note that the horizontal coordinate, X, is arranged such that, while $X < 0$, $X = 0$, and $X > 0$, the tornado center physically approaches the prism, nominally coincides with the prism, and leaves the prism, respectively.

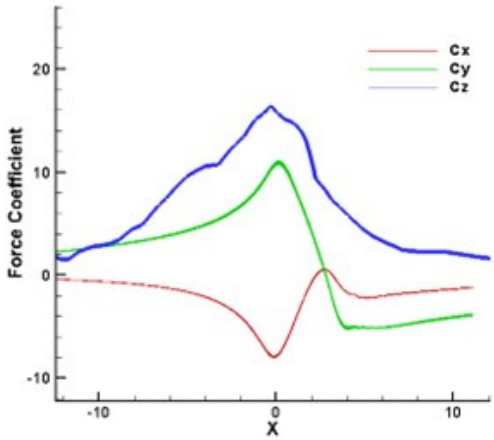

Figure 2: Evolution of force coefficients in three directions

When the translating tornado center approaches the prism, C_x keeps decreasing and stays negative, while both C_y and C_z keep positive and continuously increasing. This indicates the following tornado characteristics in the approaching stage: (1) the building is attracted by the tornado in the *x*-direction, and the closer between the tornado center of the building, the larger attractive force; (2) the building is pushed by the tornado towards the positive *y*-direction due to the counter-clockwise rotation direction of the airflow, and the closer between the tornado center of the building, the larger pushing force; and (3) the building experiences an upward suction force in the *z*-direction, and the closer between the tornado center of the building, the larger suction force. When the tornado is in the stage of nominally coinciding with the building, the three force coefficients consistently reach their respective extreme values, challenging the wind-resistant capability of the building to the utmost extent. Compared with each other, the magnitude of the *z*-direction force component is the highest, suggesting that the vertical force component of a tornado plays a significant role in the tornado dynamics study. Extensive simulations are underway to investigate the interaction between a variety of tornadic wind scenarios and differently deployed multi-constructions owing to the embedment of the IB strategy.

References

[1] N. B. Ward, *The exploration of certain features of tornado dynamics using a laboratory model*, Journal of the Atmospheric Sciences, **29**, 1194–1204, 1972.

[2] W. S. Lewellen, D. C. Lewellen, R.I. Sykes, *Large-eddy simulation of a tornado's interaction with the surface*, Journal of the Atmospheric Sciences, **54(5)**, 581-605, 1997.

[3] D. C. Lewellen, W. S. Lewellen, *Near-surface intensification of tornado vortices*, Journal of the Atmospheric Sciences, **64(7)**, 2176-2194, 2007.

[4] D. Natarajan, H. Hangan, *Large Eddy Simulation of Translation and Surface Roughness Effects on Tornado-like Vortices*, Journal of Wind Engineering Applications and Industrial Aerodynamics, **104**, 577-584, 2012.

[5] R. P. Selvam, P. C. Millett, *Computer modeling of tornado forces on buildings*, Wind and Structures, **6(3)**, 209-220, 2003.

[6] P. Gorecki, R. P. Selvam, *Rankine combined vortex interaction with a rectangular prism*, International Journal of Computational Fluid Dynamics, **29(1)**, 120-132, 2015.
[7] J. Smagorinsky, *General circulation experiments with the primitive equations: I. The basic experiment*, Monthly weather review, **91(3)**, 99-164, 1963.
[8] X. Guo, J. Cao, *An IB-LBM investigation into the aerodynamic coefficients in relation to the rotation intensity of a tornado-like wind*, Computers and Mathematic with Applications, **78**, 1206-1226, 2019.
[9] X. Guo, R. Palanisamy J. Cao, *A two-dimensional IB-LBM framework combined with re-tailored RCVM for assessing the rotation intensity of a tornadic wind over a building configuration*, Engineering Structures, **131**, 57-68, 2017.
[10] S. Laizet S, N. Li, *Incompact3d: a powerful tool to tackle turbulence problems with up to O (10^5) computational cores*, International Journal for Numerical Methods in Fluids, **67(11)**, 1735-1757, 2011.
[11] S. Laizet, E. Lamballais, *High-order compact schemes for incompressible flows: A simple and efficient method with quasi-spectral accuracy*, Journal of Computational Physics, **228(16)**, 5989-6015, 2009.
[12] S. K. Lele, *Compact finite difference schemes with spectral-like resolution*, Journal of Computational Physics, **103**, 16-42, 1992.
[13] J. Kim, P. Moin, *Application of a fractional-step method to incompressible Navier–Stokes equations*, Journal of Computational Physics, **59**, 308-323, 1985.

* * *

Quasi-Monte Carlo Algorithms for Eigenvalue Problems

S.-M. Gurova, A. Karaivanova

1 Introduction

In recent decades, some iterative Monte Carlo (MC) methods (such as Power MC iteration and Resolvent MC iteration) have established themselves as a successful approach for estimating extremal eigenvalues, especially those of large sparse matrices [1–4]. Note, that when we use low discrepancy sequences, such as Sobol or Halton sequences, these methods are called quasi-Monte Carlo (QMC). One advantage of QMC methods is their convergence rate which is typical $\mathcal{O}((logN)^n N^{-1})$ where n is the dimension of the problem, while the MC methods usually have a convergence $\mathcal{O}(N^{-\frac{1}{2}})$. On the other hand, recent developments of randomized quasi-random sequence generators [5,6] and their successful use in new supercomputing technologies for solving large-scale problems motivate us to develop and investigate new randomized QMC algorithms.

In this short scientific communication, we present the pseudo-code descriptions of the Power QMC and the Reselvent QMC algorithms for estimating the extreme eigenvalues of non-singular symmetric matrices.

Let $A = \{a_{ij}\}_{i,j=1}^{n} \in \mathbb{R}^{n\times n}$ is a given non-singular symmetric matrix. Consider the eigenvalue problem: find $\lambda(A)$ such that:

$$Ax = \lambda(A)x, \;\; x \in \mathbb{R}^n \tag{1}$$

$$0 < \lambda_{min} = \lambda_n < \lambda_{n-1} \leq \lambda_{n-2} \leq \ldots \leq \lambda_2 < \lambda_1 = \lambda_{max}.$$

The Power method [7] gives an estimate for the dominant eigenvalue λ_1.

$$\lambda_{max} = \lambda_1 \approx \lim_{k\to\infty} \frac{(h, A^k f)}{(h, A^{k-1} f)}, \tag{2}$$

where $(h, A^k f)$ is a scalar product, $f = \{f_i\}_{i=1}^{n}$ and $h = \{h_i\}_{i=1}^{n}$ are arbitrary vectors.

The extreme eigenvalues, λ_{min} and λ_{max} can be estimated by the Resolvent Power method,

$$\lambda = \frac{(h, AR_q^m f)}{(h, R_q^m f)} \approx \lambda_{max}, \text{ if } q > 0, \tag{3}$$

and

$$\frac{(h, AR_q^m f)}{(h, R_q^m f)} \approx \frac{1}{q}(1 - \frac{1}{\mu^{(m)}}) \approx \lambda_{min} \text{ if } q < 0,$$

where $\mu^{(m)}$ is the approximation value to the dominant eigenvalue of the resolvent matrix $R_q = [I - qA]^{-1} \in R^{n \times n}$. We suppose $|q\lambda| < 1$ or $|q| \parallel A \parallel < 1$, than R_q^m can be presented as an infinity series:

$$R_q^m = [I - qA]^{-m} = \sum_{i=0}^{\infty} q^i C_{i+m-1}^i A^i. \tag{4}$$

In the last formulas, q is an acceleration parameter, m is the power of the resolvent matrix, and C_{i+m-1}^i are binomial coefficients [8].

2 Power MC and Resolvent MC methods

To define Power MC methods and Resolvent MC methods the following random variable $\theta^{(k)}$ for evaluating the scalar product $(h, A^k f)$ is constructed. For this purpose, we consider the Markov chain:

$$l_0 \to l_1 \to \cdots \to l_j \to \ldots \quad (1 \le l_j \le n) \tag{5}$$

with initial density vector $p = \{p_\alpha\}_{\alpha=1}^n$, $Pr(l_0 = \alpha) = p_\alpha$ and the transition density matrix, $P = \{p_{\alpha\beta}\}_{\alpha,\beta=1}^n$, $Pr(l_j = \beta | l_{j-1} = \alpha) = p_{\alpha\beta}$, where

$$p_\alpha = \frac{|h_\alpha|}{\sum_{\alpha=1}^n |h_\alpha|} \text{ and } p_{\alpha\beta} = \frac{|a_{\alpha\beta}|}{\sum_{\beta=1}^n |a_{\alpha\beta}|}. \tag{6}$$

Then $\theta^{(k)}$ has the form

$$\theta^{(k)} = \frac{h_{l_0}}{p_{l_0}} W_k f_{l_k}, \text{ where } W_0 = 1, \ W_j = W_{j-1} \frac{a_{l_{j-1} l_j}}{p_{l_{j-1} l_j}}, \quad j = 1, \ldots, k. \tag{7}$$

It is shown [8,9] that mathematical expectation of $\theta^{(k)}$ is:

$$E[\theta^{(k)}] = (h, A^k f) \approx \frac{1}{N} \sum_{s=1}^{N} (\theta^{(k)})_s. \tag{8}$$

It is easy to show that:

$$\sum_{i=0}^{\infty} q^i C_{i+m-1}^i E[\theta^{(i)}] = (h, [I - qA]^{-m} f), \ \ m = 1, 2, ... \tag{9}$$

taking into account the construction of the random variable $\theta^{(k)}$ and formulas (3) and (4).

The Power MC method is defined in the following way:

$$\lambda_{max} = \lambda_1 \approx \frac{\sum_{s=1}^N (\theta^{(k)})_s}{\sum_{s=1}^N (\theta^{(k-1)})_s}. \tag{10}$$

The Resolvent MC method is described by the formula:

$$\lambda \approx \frac{\sum_{i=0}^{k} q^i C_{i+m-1}^i E[\theta^{(i+1)}]}{\sum_{i=0}^{k} q^i C_{i+m-1}^i E[\theta^{(i)}]}, \tag{11}$$

where $\theta^{(0)} = 1$ and the random variables $\theta^{(i)}$ are defined according (7).

In the formula (11), we have two options for the acceleration parameter q. In the case when $q > 0$, we find $\lambda_1 = \lambda_{max}$ and in the case when $q < 0$ we estimate $\lambda_n = \lambda_{min}$ of the matrix A.

We mention that the values of the random variables in both MC methods are computed using pseudorandom generators to define jumps in the Markov chain (5).

When we use low discrepancy sequences such as Sobol ones [5,6] to define the indexes in the jump of the Markov chain, the above methods are defined as Power QMC and Resolvent QMC methods.

3 QMC algorithms for estimating the biggest and the smallest eigenvalue of symmetric matrix

Algorithm 1 Pseudo code for computing the Power QMC algorithm

1: INPUT: matrix $A = \{a_{ij}\} \in \mathbb{R}^{n\times n}$; vectors $h, f \in \mathbb{R}^n$ and positive integers n, N, k

2: COMPUTE: $p_\alpha = \frac{|h_\alpha|}{\sum_{\alpha=1}^{n} |h_\alpha|}; p_{\alpha\beta} = \frac{|a_{\alpha\beta}|}{\sum_{\beta=1}^{n} |a_{\alpha\beta}|},\ 1 \le \alpha \le n,\ 1 \le \beta \le n$

3: COMPUTE: $a_i = \sum_{j=1}^{n} |a_{ij}|,\ \ 1 \le i \le n$

4: GENERATE: N elements of the $(k+1)$ - dimensional Sobol sequence

5: CONSTRUCT: N realisations of the Markov chain with integer elements

$$l_1^{(s)} \to l_2^{(s)} \to \ldots \to l_k^{(s)} \to l_{k+1}^{(s)},\ 1 \le l_i^{(s)} \le n,\ 1 \le i \le k+1,\ 1 \le s \le N$$

6: COMPUTE:

$$\overline{\theta}^{(k)} = \frac{1}{N} \sum_{s=1}^{N} sign(a_{l_k^{(s)} l_{k+1}^{(s)}}) a_{l_k^{(s)}} f_{l_{k+1}^{(s)}}\ ; \quad \overline{\theta}^{(k-1)} = \frac{1}{N} \sum_{s=1}^{N} f_{l_k^{(s)}}$$

7: OUTPUT: $\lambda_{max} \approx \frac{\overline{\theta}^{(k)}}{\overline{\theta}^{(k-1)}}$

Algorithm 1 describes the Power QMC algorithm for estimating the largest eigenvalue of non-singular symmetric matrix A. To generate k - dimensional Sobol sequences we can use BRODA's Sobol Randomized Sequence Generator (RSG) [5,6]. The indexes in the Markov chain (step 5 of Algorithm 1) are funded using the initial densities and the transition densities from Step 2. Step 4 in Algorithm 1 can be replaced with other quasi-random sequences such as Halton or Faure sequences [10,11]. When we apply pseudorandom generations in step 4 of Algorithm 1 we have systematic and stochastic errors. The balance between the two errors is investigated in [8,9]. Thus we can choose k and N in such a way to receive a good balance between both errors.

Algorithm 2 Pseudo code for computing the Resolvent QMC algorithm

1: INPUT: matrix $A = \{a_{ij}\} \in \mathbb{R}^{n\times n}$; vectors $h, f \in \mathbb{R}^n$, positive integers n, N, k, m and the real number q

2: COMPUTE: $p_\alpha = \frac{|h_\alpha|}{\sum_{\alpha=1}^{n}|h_\alpha|}; p_{\alpha\beta} = \frac{|a_{\alpha\beta}|}{\sum_{\beta=1}^{n}|a_{\alpha\beta}|},\ 1 \le \alpha \le n,\ 1 \le \beta \le n$

3: COMPUTE: $a_i = \sum_{j=1}^{n}|a_{ij}|,\ \ 1 \le i \le n$

4: GENERATE: N elements of the $(k+1)$ - dimensional Sobol sequence

5: CONSTRUCT: N realizations of the Markov chain with integers elements

$$l_1^{(s)} \to l_2^{(s)} \to \cdots \to l_k^{(s)} \to l_{k+1}^{(s)},\ 1 \le l_i^{(s)} \le n,\ 1 \le i \le k+1,\ 1 \le s \le N$$

6: COMPUTE:

$$\overline{\theta}^{(i)} = \frac{1}{N} \parallel h \parallel \sum_{s=1}^{N} sign\{h_{l_1^{(s)}} \prod_{i=1}^{k+1}(a_{l_i^{(s)} l_{i+1}^{(s)}})\} \prod_{i=1}^{k+1} a_{l_i^{(s)}} f_{l_{i+1}^{(s)}};\ \ 1 \le i \le k+1$$

7: COMPUTE:

$$C_{i+m-1}^{i} = \frac{(i+m-1)!}{i!(m-1)!}, \text{where } 1 \le i \le k$$

8: OUTPUT:

$$\lambda \approx \frac{\overline{\theta}^{(1)} + qC_m^1\overline{\theta}^{(2)} + q^2C_{m+1}^2\overline{\theta}^{(3)} + ... + q^kC_{k+m-1}^k\overline{\theta}^{(k+1)}}{1 + qC_m^1\overline{\theta}^{(1)} + q^2C_{m+1}^2\overline{\theta}^{(2)} + ... + q^kC_{k+m-1}^k\overline{\theta}^{(k)}}$$

Algorithm 2 describes the Resolvent QMC algorithm for estimating the largest and the smallest eigenvalues of non-singular symmetric matrix A. When we choose accelerated parameter q to be negative we estimate the smallest eigenvalue of A. Here, the power m of the resolvent matrix affects the convergence of the iteration process. Thus, we need to control the parameter m when the systematic and stochastic errors are balanced [12]. The construction of the discrete-valued Markov chain in step 5 in both Algorithms is done in the same way as in the article [13]. The difference is that instead of quasirandom numbers low discrepancies sequences are used.

4 Conclusion

Algorithm 2 is written in $C++$ program code using Sobol sequences and pseudorandom numbers for estimating the smallest eigenvalue when $q < 0$. Some numerical results for given symmetric matrices A were presented in [12]. Algorithm 1 is also written in $C++$ program code using only a pseudorandom number generator to investigate the balance between stochastic and systematic error. Some numerical results for given matrices A were described in [9]. In future work, we will continue to test both algorithms for large dimensional sparse or dense matrices to find the best balance between all errors.

Acknowledgements

The work was carried out using the infrastructure purchased under the National Roadmap for RI, financially coordinated by the MES of the Republic of Bulgaria (Grant No. DO1-325/01.12.2023) and supported also by Grant No 30 from CAF America.

References

[1] Alexandrov, V., et al.: On the Prec. QMC Alg. for Matrix Comput., LNCS, Vol. 9374, Springer, 163-171, (2015), DOI:10.1007/978-3-319-26520-9 17

[2] Dimov, I.T., et al.: Robustness and applicability of MCMC algorithms for eigenvalue problems. Appl. Math. Modelling, 32, 8, Elsevier Inc., 1511-1529, (2008),DOI: http://dx.doi.org/10.1016/j.apm.2007.04.012
[3] Mascagni, M., Karaivanova, A.: Matrix computations using quasirandom sequences. LNCS, Springer, vol.1988, 552–559, (2001) https://doi.org/10.1007/3-540-45262-165
[4] Dimov, I., Karaivanova, A.: A Power Method with MC Iterations, Proceeding Recent Advances in Num. Methods and Appls II, World Scientific, 239-247, (1999), https://doi.org/10.1142/9789814291071_0022
[5] Sobol, I.M., Asotsky, D., Kreinin, A., Kucherenko, S.: Construction and Comparison of High-Dimensional Sobol' Generator, WILMOTT magazine, 64-79, (2012).
[6] BRODA's Sobol RSG: broda.co.uk/software.html (Last accessed: 15 April 2024)
[7] Isaacson, E., Keller, H.B.: Analysis of Numerical Methods. Dover Publications, Mineola; Wiley New York, (1996). ISBN 0-486-68029-0.
[8] Dimov, I.: Monte Carlo Methods For Applied Scientists, World Scientific, (2008), ISBN:9812779892
[9] Gurova, S.-M., Karaivanova, A.: Monte Carlo Method for Estimating Eigenvalues Using Error Balancing. LNCS, vol 13127, 447-455, Springer, (2022) https://doi.org/10.1007/978-3-030-97549-4_51
[10] Faure, H., Lemieux, Ch.: Generalized Halton sequences in 2008: A comparative study. ACM Transactions on Modeling and Comp. Sim. Vol. 19, Issue 404, 1–31, (2009) https://doi.org/10.1145/1596519.1596520
[11] Faure, H., Good permutations for extreme discrepancy, Journal of Number Theory, Vol. 42, 47-56, (1992)
[12] Gurova, S.-M., Atanassov, E., Karaivanova, A., A Resolvent Quasi-Monte Carlo Method for Estimating the Minimum Eigenvalues Using the Error Balancing, In: Lirkov, I., Margenov, S. (eds), LSSC 2023, LNCS, vol.13952 (accepted for publication)
[13] Dimov, I., Dimov T., Gurov, T., A new iterative Monte Carlo approach for inverse matrix problem, JCAM, **92** (1), 15-35, (1998)

* * *

Efficient Solution Algorithm for the Three Dimensional Diffusion Equations on General Hexahedral Meshes

X. Hang

1 Introduction

In the simulation of 3D radiation hydrodynamics, a large part of time(over 80%) is spent on the solution of the diffusion equations. We introduce an efficient solution algorithm for the 3D diffusion equation on general3D hexahedral meshes. In the new algorithm, the structure of the finite volume scheme is used to reduced the storage and computation work of the linear systems. And the proposed new solution method is easy in implementation.

2 Algorithm

Firstly, we review the Pyramid scheme(P-scheme) for diffusion equations on general hexahedral meshes[1]. On general hexahedral cells, the cell faces can be non-planar, which leads to extra difficulty in the discretization. T pyramid scheme gives a unique flux for every cell face.

The flux takes the form

$$F_\sigma = \tau_{\bar{\sigma}}(u_K - u_L + u_{L'} - u_{K'})|n_e| \tag{1}$$

where $\frac{\tau_\sigma = \kappa_K \kappa_L}{\kappa_K d_{LL'} + \kappa_L d_{KK'}}$, and $u_{L'} - u_{K'} \approx \alpha(u_C - u_A) + \beta(u_D - u_B)$, and the $u_A, u_B, u_C, u_D$are expressed by the cell-centered unknowns around. Numerical experiments show the scheme is 2^{nd} order

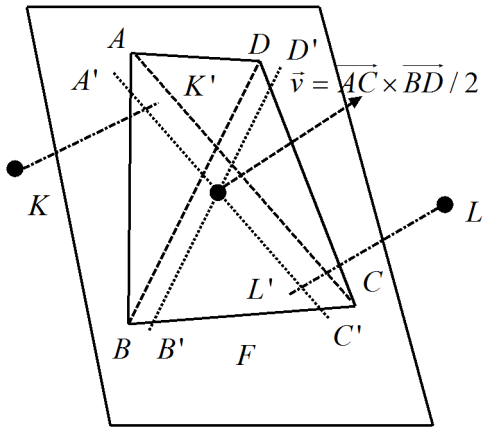

Figure 1: The flux on the cell face

accuracy. The scheme is much more efficient than the conventional method, which split the non-planar face into 4 triangles.

Table 1: The comparison of the CPU time (seconds) of discretization on the 3D distorted mesh.[1]

	smooth coefficient		discontinuous coefficient	
number of cells	P-scheme	O-scheme	P-scheme	O-scheme
$64 \times 64 \times 64$	2.0e-2	5.3e-1	3.0e-2	5.6e-1

Secondly, we propose a new solution algorithm for the linear system, which utilizes a new matrix form based on the flux expression of diffusion scheme. On a structured hexahedral mesh, the matrix of the linear system is a 27-diagonal matrix. So the computational work is quite large. By decomposing the matrix to the form

$$A = C + GW \tag{2}$$

where C is a 7-diagonal matrix which is related to $\tau_{\bar{\sigma}}(u_K - u_L)|n_e|$, and $G$is a 8-diagonal matrix related to $\tau_{\bar{\sigma}}(u_{L'} - u_{K'})|n_e|$, and W is also a 8-diagonal matrix related to the expression of the u_A, u_B, u_C, u_D. So the storage requirement is only 7+8+8=23. And the computational work of the MVM operation is also about 23 multiplication operations. Moreover, the matrix decomposition gives a M-matrix C. So it is quite fit for a preconditioner to the matrix A. We show the preconditioner is quite robust and efficient for the matrix A in the numerical experiments.

3 Numerical experiments

Consider the Poisson equation

$$-\nabla \cdot \nabla T = f \tag{3}$$

where the exact solution is

$$T(x, y, z) = 0.1e^{-0.5z}(x^2 + y^2) \tag{4}$$

$f$is determined by the exact solution and the Dirichlet boundary is applied.

Three kinds of meshes are tested. The first one is the orthogonal mesh, the second is the a mesh with small distortion and the third one is a mesh with large distortion as shown in Figure .

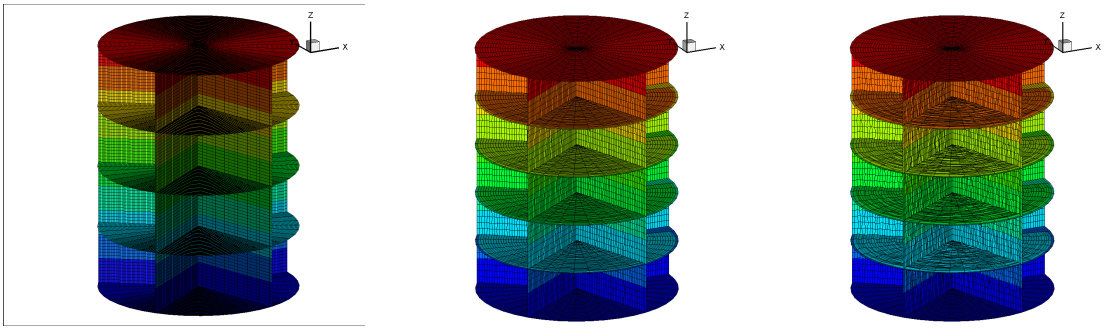

(a) The error distribution for the DFVE scheme. (b) The error distribution for the DFE scheme. (c) The error distribution for the DFE scheme.

Figure 2: The error distribution on the cubic domain with $\alpha = 0.65$.

The distorted meshes are generated by

$$\bar{\vec{x}} = \vec{x} + \varepsilon \begin{pmatrix} ran1 \\ ran2 \\ ran3 \end{pmatrix} h_x \tag{5}$$

Where $ran1$, $ran2$, $ran3$ are 3 random numbers, h_x is the minimal distance to the neighboring cell grids. ε is a parameter range from 0 to 0.5. The preconditioner is generated by a subroutine in the software SPARSKIT2 which is the ILUT $1.E-6,13$ preconditioner [2], which permits 27 non-zeros for each row.

The size of the tests problems ranges from 16000 to 256000, and it is considered to be convergent if the residual reduces to 10^{-6}. Three tables are listed below. In the tables, we give the times and iteration numbers for different items. PCGEN is the time for the generation of the preconditioner. PCSOL is the time for the solution of the preconditioner. MVM is the time for the matrix vector multiplication and SOLU is the time for the total solution, which contains MVM and PCSOL,but not PCGEN.

Table 2: Solution time for the case of orthogonal meshes

Algorithm	Item	20,20,40	20,40,20	20,40,40	40,40,40	40,40,80	40,80,80
Old	PC GEN	1.64E-1	3.47E-1	4.52E-1	1.004	1.247	3.559
	PCSOL/LIT	2.9E-2/31	3.2E-2/32	8.6E-2/41	2.43E-1/57	6.55E-1/80	1.764/108
	MVM/LIT	1.5E-2/33	1.6E-2/34	4.1E-2/44	1.01E-1/60	2.65E-1/84	7.39E-1/114
	SOLU	5.6E-2	5.9E-2	1.57E-1	4.28E-1	1.175	3.302
New	PC GEN	1.67E-1	3.47E-1	4.61E-1	1.006	1.326	3.586
	PCSOL/LIT	3.1E-2/31	3.3E-2/32	8.3E-2/41	2.53E-1/57	6.51E-1/80	1.802/108
	MVM/LIT	1.E-2/33	1.E-2/34	3.4E-2/44	8.7E-2/60	2.28E-1/84	6.69E-1/114
	SOLU	5.7E-2	5.7E-2	1.49E-1	4.28E-1	1.132	3.283

For the orthogonal meshes, $A = C$. So the iteration numbers are the same for the two methods. The main difference is on the time for MVM, where the new method costs less time.

Table 3: Solution time for the case of small distorted meshes.

Algorithm	Item	20,20,40	20,40,20	20,40,40	40,40,40	40,40,80	40,80,80
Old	PC GEN	2.51E-1	4.46E-1	6.63E-1	1.65	2.339	6.051
	PCSOL/LIT	3.1E-2/32	3.1E-2/32	8.5E-2/42	2.26E-1/54	6.65E-1/80	1.756/108
	MVM/LIT	1.5E-2/34	1.3E-2/34	4.1E-2/45	9.3E-2/57	2.7E-1/84	7.48E-1/114
	SOLU	6.1E-2	6.E-2	1.57E-1	3.98E-1	1.198	3.285
New	PC GEN	1.9E-1	3.76E-1	5.37E-1	1.32	1.682	4.843
	PCSOL/LIT	3.2E-2/32	2.9E-2/32	8.8E-2/42	2.15E-1/54	6.54E-1/80	1.744/108
	MVM/LIT	1.7E-2/34	1.8E-2/34	3.1E-2/45	8.E-2/57	2.3E-1/84	6.39E-1/114
	SOLU	6.E-2	5.8E-2	1.53E-1	3.72E-1	1.142	3.168

Table 4: Solution time for the case of large distorted meshes.

Algorithm	Item	20,20,40	20,40,20	20,40,40	40,40,40	40,40,80	40,80,80
Old	PC GEN	2.8E-1	4.83E-1	7.63E-1	1.833	2.588	6.701
	PCSOL/LIT	3.4E-2/33	3.3E-2/33	8.6E-2/42	2.26E-1/55	6.6E-1/80	1.773/109
	MVM/LIT	1.2E-2/35	1.8E-2/35	4.1E-2/45	9.3E-2/58	2.78E-1/84	7.52E-1/115
	SOLU	6.2E-2	6.1E-2	1.6E-1	3.93E-1	1.204	3.342
New	PC GEN	2.1E-1	3.97E-1	6.31E-1	1.406	1.903	5.086
	PCSOL/LIT	2.7E-2/32	3.7E-2/32	8.4E-2/41	2.19E-1/53	6.57E-1/80	1.728/108
	MVM/LIT	1.6E-2/34	1.1E-2/34	3.6E-2/44	7.1E-2/56	2.32E-1/84	7.05E-1/114
	SOLU	5.9E-2	6.4E-2	1.48E-1	3.64E-1	1.145	2.99

For small and large distorted mesh, the preconditioner is equally efficient.Sometimes the new preconditioner is even a little more efficient. And the PCGEN of the new method costs less time. The MVM operation also cost less time for large size problems.

4 Conclusion

In all, the new solution method is more efficient than the conventional ones both in storage and computation. At the same time, the solution method can be extended to more complex problems.

Acknowledgements

This work is partially supported by the National Science Foundation of China (nos. 12001049 ,11971069 and 12035002), the CAEP Fundation(Grant No. CX20210021).

References

[1] Wang, S., et al. (2017). "A pyramid scheme for three-dimensional diffusion equations on polyhedral meshes." Journal of Computational Physics **350**: 590-606.

[2] Y. Saad, Iterative Methods for Sparse Linear Systems, PWS Publishing Company, Boston, 1996.

* * *

On the Efficient Preconditioning of the Stokes Equations in Tight Geometries

V. Pimanov, O. Iliev, E. Muravleva, I. Oseledets

If the Stokes equations are properly discretized in a simple domain, it is well-known that the Schur complement matrix can be efficiently preconditioned by a diagonal matrix. This is the rationale behind the famous Uzawa and Krylov-Uzawa algorithms. Recently, however, it was demonstrated that in the case of complex geometries coming from tight porous media, a diagonal preconditioner for the Schur com- plement matrix is less efficient compared to the Laplacian-like SIMPLE preconditioner. In this presentation we investigate this behavior for staggered finite-difference discretization and identify certain domain characteristics which are indicators for the performance of the respective Stokes solvers. We start by presenting specific 3D samples from tight rocks for which the established Uzawa algorithm stagnates, while the SIMPLE preconditioner ensures robust convergence to low tolerances. To explain this behavior, we perform a comprehensive numerical study for synthesized 2D geometries — periodic arrays of randomly shifted square obstacles. For these synthetic geometries, we compute the full spectra of the Schur complement matrix and study how it depends on such geometric charac- teristics as the average and minimum channel thicknesses. The performed experiments show that there is one to one correspondence between the number of non-unit eigenvalues of the Schur complement matrix and the surface area of the boundary where no-slip boundary conditions are imposed, with an additional correction for the connectivity of the flow domain. We conclude that an increase in the surface-to-volume ratio leads to an increase of the condition number of the Schur complement matrix, while the dependence is inverse for the Schur complement matrix preconditioned with SIMPLE. We conjecture that in general the no-slip boundary conditions are the reason for the non-unit eigenvalues of the Schur complement and show numerical results supporting this.

* * *

Impeding Viral Interception of Intracellular Information Flow: a Novel Strategy for Targeted-Therapeutics Design

N. Ilieva

A key concept in biology and medicine as well as in information theory is awareness of the significance of information in comprehending living matter as a whole and the organization and dynamics of processes within it. The idea that coding is a crucial characteristic that sets living things apart from non-living materials suggests that information flow — which happens mostly through transcription and translation processes in DNA — and its potential obstructions are vital components of living systems. Viral infections can be thought of as a process that impairs the cell's normal information flow, hindering regular functions and potentially resulting in cell death. This highlights the sensitive nature of the cellular information system and the dynamic interplay between living beings and the various environmental factors and agents.

We examine this process using two key proteins of the SARS-CoV-2 virus — the helicase NSP13 and the ORF6 protein. They both play a significant role in antagonizing host-cell interferon signalling pathways [1]. In addition, NSP13 is involved in viral replication while ORF6 prevents mRNA export from the nucleus into the cytoplasm (Fig. 1), thus blocking the synthesis of cell proteins but also affecting cell-DNA replication by favouring RNA-DNA hybrids accumulation [2]. Interestingly, these are the

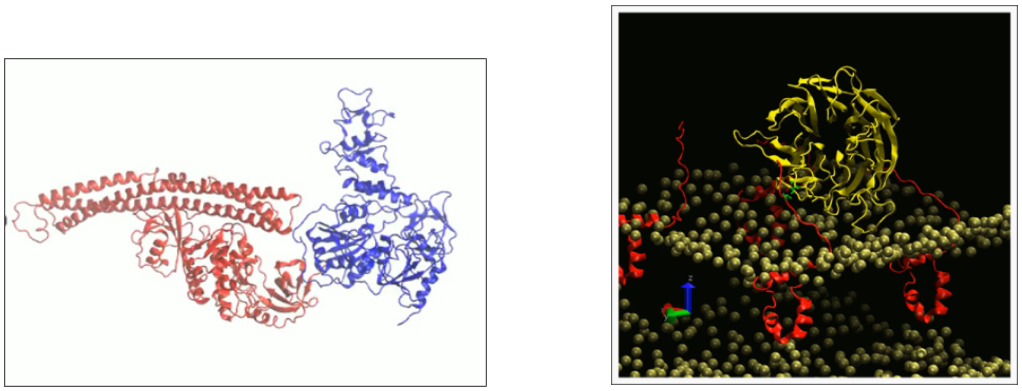

Figure 1: (a) The helicase NSP13 engages with TBK1, a key element of the innate immunity antiviral response; (b) SARS-CoV-2 ORF6 immobilises the mRNA export factor RAE1 on the cellular membrane.

two viral proteins with the highest, respectively the lowest degree of homology with the corresponding proteins of the previous corona virus that generated deadly outbreaks — the SARS-CoV virus: only 69.9% for the ORF6 protein and just one amino acid difference for the helicase NSP13. No effective inhibitors of these two viral proteins have been reported to date. We explore the possibilities of modern information technologies for the intelligent design of precision pharmaceutical agents for targeted action against specific intracellular proteins, using these two proteins as a working model [3,4]. Our attention is directed towards peptide aptamers — combinatorial sequences of 5-20 amino acids, that belong to the fastest-growing class of therapeutics, the protein-based bioactive agents. Addressing the challenges of intracellular drug delivery this pilot study may reveal new perspectives for the development of biological agents with the potential for therapeutic applications and practical solutions in medicine and pharmaceutics.

Contributors

The reported results are obtained through concerted multidisciplinary investigations conducted by: N. Ilieva, E. Lilkova (Institute of Information and Communication Technologies, BAS); I. Ivanov, G. Nacheva, A. Gospodinov, E. Krachmarova, R. Hristova, K. Malinova (Institute of Molecular Biology "Acad. R. Tsanev", BAS); L. Litov, P. Petkov, D. Stoynova, T. Nedeva (Sofia University "St. Kl. Ohridki", Physics Faculty); M. Rangelov (Institute of Organic Chemistry with Center of Phytochemistry, BAS); N. Todorova (Institute of Biodiversity and Ecosystem Research, BAS); A. Pashov (Steffan Angelov Institute of Microbiology, BAS); S. Pashova (Institute of Biology and Immunology of Reproduction, BAS).

Acknowledgments

We acknowledge the inspiring discussions within the DYNALIFE COST Action, CA21169, supported by the European Cooperation in Science and Technology. This work was supported in part by the Bulgarian National Science Fund (grant KP-06-N71/3/2023).

Computational resources were provided by CI TASK (Centre of Informatics–Tricity Academic Supercomputer & networK), Gdansk (Poland), as well as the BioSim HPC cluster at the Faculty of Physics, Sofia University "St. Kliment Ohridski".

References

[1] C.K. Yuen, J.Y. Lam, W.M. Wong, L.F. Mak et al. *SARS-CoV-2 nsp13, nsp14, nsp15 and orf6 function as potent interferon antagonists* Emerg. Microbes Infect. **9** (2020) 1418–1428.

[2] E. Krachmarova, P. Petkov, E. Lilkova, N. Ilieva, M. Rangelov et al. *Insights into the SARS-CoV-2 ORF6 Mechanism of Action* Int. J. Mol. Sci. **24**(14) (2023) 11589.

[3] E. Krachmarova, P. Petkov, E. Lilkova, D. Stoynova, K. Malinova et al. *Interferon-γ as a Potential Inhibitor of SARS-CoV-2 ORF6 Accessory Protein* Int. J. Mol. Sci. **25**(4) (2024) 2155

[4] M. Rangelov, N. Todorova, P. Petkov, T. Nedeva, N. Ilieva et al. *In silico screening for potential inhibitors of the SARS-CoV-2 helicase Nsp13* In: E. Lilkova et al. (eds.) Advanced Computing in Industrial Mathematics: BGSIAM 2023, SCI, Springer *(accepted)*

* * *

Generalized Net for Invalides Evacuation After Earthquake

V. Ivanov, K. Atanassov, L. Kirilov, S. Fidanova

1 Introduction

When evacuation is required, people with reduced mobility cannot move to a safe place on their own. Specialized help should be provided to such people. Disabled people and the elderly fall into the group of people with difficulty moving. A large proportion of people in this group have chronic or other co-morbidities that also need to be addressed. Due to the high stress of the evacuation event, some of these illnesses may be exacerbated. Such are cardiovascular diseases. In this development, we have focused on modeling the evacuation and helping people with difficulty moving after an earthquake. For this purpose, the apparatus of the Generalized Nets (GN) will be used [1,2]. The model will include the individual steps that need to be taken to get disabled people from their place of residence to a safe place and provide them with the necessary medical care. The model can be used by local authorities to prepare action teams in advance.

2 Generalised Nets

With this development, Generalized Nets are applied for modeling the evacuation process of people with difficulty moving after an earthquake. GN were proposed 40 yera ago by K. Atanassov [1,2]. They are a powerful and convenient tool for describing and modeling a variety of processes, in industry, in living organisms, and more [3–5].

The structure of GN consists of **tokens**, which act as information carriers and can occupy a single place at every moment of the GN execution. The tokens pass through the transition from one input to another output place. The tokens' movement is governed by conditions (predicates), contained in the index matrix of the transition [6]. The information carried by a token is contained in its **characteristics**, which is obtained by a **characteristic function**. Every place possesses at most one characteristic function, which assigns new characteristics to the incoming tokens. Tokens can split and merge in the places. A transition can contain m input and n output places where $n, m \geq 1$ (see Figure 1) and m and n can be different.

A convenient quality of generalized networks is their extensibility. First a simpler mesh can be made giving the basic elements of the model. Each transition can then be replaced with a net and thus the model evolves and new details are added to it.

Each separate step of the evacuation process will be represented by a separate transition. The tokens have specific characteristics corresponding to the data they represent. They interact with other tokens as they enter the transition, and there their characteristics can be changed.

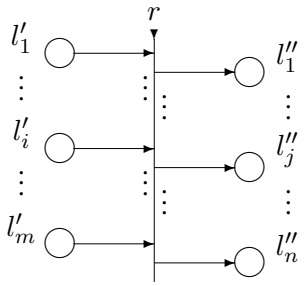

Figure 1: The form of transition in a GN

3 GN for Evacuation of Invalids

Earthquakes are natural phenomena that cause a lot of material damage, but the most important thing is saving human life. Good organization and advance preparation are of great importance. People with limited mobility, such as the disabled and the elderly, are particularly vulnerable. They need specialized help to leave their homes and evacuate to a safe place. When there is a crowding of people with difficulty moving, then an organization and a plan for their evacuation must be created in advance. These are the cases of the presence of nursing homes or homes for the disabled in the earthquake area.

The input data for this model are the addresses of those in need. It should also be noted whether there are up to 2 people at this address or if it is a social home and how many residents there are. When it comes to a social home such as a home for the disabled or a home for the elderly, their number is needed to make a preliminary evacuation plan. I.e. their evacuation will be a separate generalised net that will be incorporated as part of the overall evacuation generalized net.

In the second transition, sorting will be done according to the earthquake resistance of the building (possible degree of destruction) and if it is not destroyed, on which floor is the person with reduced mobility. A judgment will be made about the way of removing the needy and the need for additional or special tool.

In the third transition, an assessment will be made of the possibility that the disabled person has suffered some kind of injury and needs additional medical assistance or hospitalization.

In the fourth transition, disabled people taken out of the buildings will be grouped according to whether they have co-morbidities that require treatment and will be assigned to appropriate health facilities or accommodation centers accordingly.

The most important striking factors in earthquakes are traumatic and thermal. A team of scientists from the Trakia University, Stara Zagora, are developing new forms for topical application to treat wounds and burns, which could be applied in such situations.

4 Conclusion

Advance preparation and proper planning can be crucial in saving lives in an earthquake. People with reduced mobility are particularly vulnerable in such a natural disaster. When their addresses are known in advance and whether they are individuals or a social institution, preliminary arrangements can be made for their evacuation. Some of these people may have other illnesses as well as having received injuries during the earthquake. All of these data can be taken into account when evacuating people from the earthquake zone and directing them to medical facilities or accommodation centers.

Acknowledgements
The authors from IICT are supported by the National Scientific Fund of Bulgaria grant DFNI KP-06-N52/5 and by the project OMNIA grant BG05M20P011-2.016-0007 financed by the Science and Education for Smart Growth

Operational Program and co-financed by European Union. Veselin Ivanov is supported by the European Union-NextGenerationEU, through the National Recovery and Resilience Plan of the Republic of Bulgaria, project No BG- RRP-2.004-0006.

References

[1] Atanassov, K.: Generalized Nets. World Scientific. Singapore, London, 1991.
[2] Atanassov, K.: On Generalized Nets Theory. "Prof. M. Drinov" Academic Publishing House. Sofia. (2007)
[3] Krawczak, M. Multilayer Neural Systems and Generalized Net Models. Akademicka Oficyna Wydawnicza EXIT, Warszawa, 2003.
[4] Fidanova, S., K. Atanassov,L. Kirilov, V. Slavova, V. Ivanov. Generalized Nets Model of the Consecances of Earthquake, Lecture Notes in Networks and Systems, 658, 2023, 281-292.
[5] Atanassov. K. Generalized Nets and Intuitionistic Fuzziness in Data Mining. "Prof. Marin Drinov" Academic Publishing House, Sofia, 2020.
[6] Atanassov, K.: Index Matrices: Towards an Augmented Matrix Calculus. Springer, Cham (2014)

* * *

Analysis of hydrogen-enhanced decohesion across block boundaries in lath martensite

I. Katzarov

Hydrogen-enhanced decohesion (HEDE) hypothesis associates hydrogen embrittlement with a reduction of the atomic bond strength due to hydrogen segregation at a grain boundary or other interface, which leads to initiation and propagation of cracks along these interfaces when the applied stress exceeds the cohesive strength [1]. The present work presents a theoretical analysis of the phenomenon of hydrogen-enhanced decohesion in lath-martensite steel. A lath martensite grain is divided into packets comprising blocks constructed from parallel laths of martensite. Block boundaries can be low and high angle twist boundaries. We make connection between the thermodynamic-kinetic continuum and atomistic cohesive zone models to solve a coupled set of equations using atomistic data to follow the decohesion process in time as traction is applied to a hydrogen charged lath-martensite and decohesion occurs between two bcc-Fe crystals forming a block boundary.

Within our continuum decohesion model [2] we assume that the hydrogen exchange at the bulk-–interface boundary is controlled by a driving force proportional to the difference between chemical potentials in the cohesive zone and in the bulk [3]. Our atomistic simulations show that hydrogen atoms will be attracted by diffusion into the cohesive zone giving rise to an increased H occupancy. This results in a time-dependent interfacial hydrogen concentration that depends on the relation between the strain rate and the rate of bulk diffusion.

Energy versus separation curves for fixed hydrogen concentrations between decohering planes (Fig. 1a) are calculated by making atomistic calculations of the relaxed structure and excess energy of slabs having a fixed value of separation across the cohesive zone and a fixed H occupancy. The maximum of each stress versus separation curve (Fig. 1b) may be identified as a critical stress for rupture. Our calculations find a reduction in the cohesive strength as a result of dissolved hydrogen at the block boundaries. Therefore, the flux of hydrogen into the cohesive zone results in a reduction of the cohesive strength in the block boundaries.

Acknowledgements
This work was supported in part by the Bulgarian National Science Fund (grant KP-06-PN67/26).

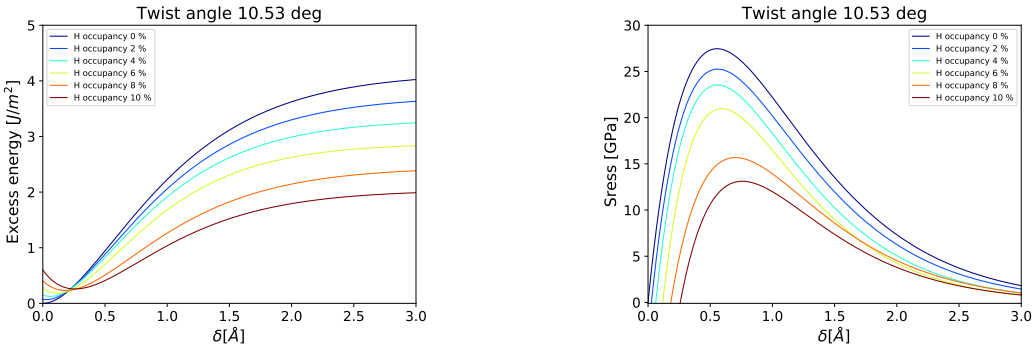

Figure 1: (a) Excess binding energy per unit area of cohesive zone as a function of opening between decohering planes. (b) Traction curves: stress as a function of opening.

References

[1] H. Birnbaum, in Hydrogen Effects on Material Behavior, edited by N. R. Moody and A. W. Thompson (The Minerals Metals and Materials Society, Warrendale, 1990), pp. 639–660.

[2] I. H. Katzarov and A. T. Paxton, Hydrogen embrittlement II. Analysis of hydrogen-enhanced decohesion across (111) planes in α-Fe, Phys. Rev. Mater. 1, 033603 (2017).

[3] Y. Mishin, P. Sofronis, and J. Bassani, Acta Mater. 50, 3609 (2002).

* * *

On the Rational Approximation of $\mathbb{A}^{-\alpha}$ and $\mathbb{A}^{\beta}$

N. Kosturski, S. Margenov

1 Introduction

Let us consider the linear system

$$\mathbb{A}^{\alpha}\mathbf{u} = \mathbf{f} \tag{1}$$

where $\mathbb{A} \in \mathbb{R}^{N\times N}$ is a sparse, symmetric and positive definite (SPD) matrix. When $\mathbb{A}$ is a result of, e.g. FDM or FEM, discretization of a given second order self-adjoin elliptic operator, and if $\alpha \in (0, 1)$, the system (1) is associated with numerical solution of sub-diffusion problems. For such problems, methods based on the best uniform rational approximation (BURA) of z^{α} on $[0, 1]$ (see [1]) for numerical solution of (1) were introduced in [2] and further developed in [3].

Here we consider the general case of $\alpha \in \mathbb{R}^{+} \setminus \mathbb{Z}$ in the spirit of [4].

2 Approximation of $\mathbb{A}^{-\alpha}$

The BURA approximation of $\mathbb{A}^{-\alpha}$ can be defined by the minimizer $r_{\alpha,k}(\xi) = P_k(\xi)/Q_k(\xi) \in \mathcal{R}(k)$,

$$r_{\alpha,k}(\xi) := \min_{r_k\in\mathcal{R}(k)} \max_{\xi\in[\lambda_1,\infty)} |\xi^{-\alpha} - r_k(\xi)|, \tag{2}$$

where $\lambda_1 > 0$ is a the first eigenvalue of $\mathbb{A}$, thus obtaining an approximate solution of the system (1) in the form

$$\mathbf{u} \approx \mathbf{u}_r := r_{\alpha,k}(\mathbb{A})\mathbf{f}.$$

Applying the approach of [4], the following estimate of the relative error can be obtained

$$\varepsilon_{bura}^{flss} = \frac{||\mathbf{u} - \mathbf{u}_r||_{\ell_2}}{||\mathbf{f}||_{\ell_2}} \leq C_\alpha e^{-2\pi\sqrt{k\alpha}}, \tag{3}$$

where

$$C_\alpha \approx 4^{1+\alpha} |\sin \pi\alpha|.$$

The exponential convergence rate of $\varepsilon_{bura}^{flss}$ ensures that a small value of the power k of BURA is sufficient to achieve the required accuracy of solving the fractional linear system (1). Now the software BRASIL (Best Rational Approximation by Consecutive Interval Length Correction) [5] is used to calculate $r_{\alpha,k}(\xi)$. Some results of the conducted numerical tests are shown in Fig. 1. They are consistent with the estimate (3).

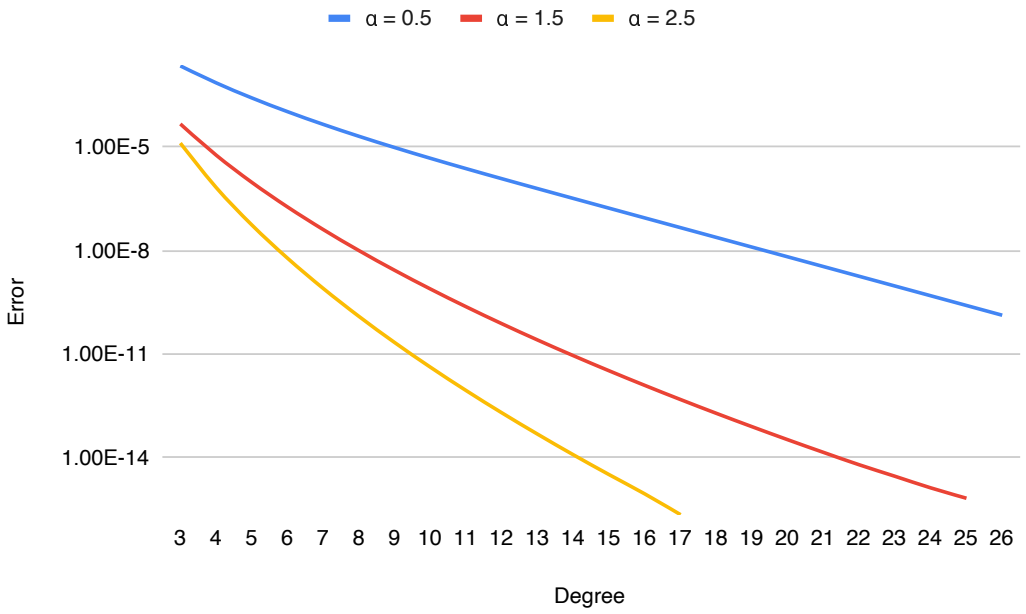

Figure 1: Relative error $\varepsilon_{bura}^{flss}$ of the numerical solution of $\mathbb{A}^\alpha \mathbf{u} = \mathbf{f}$: $\alpha \in \{0.5, 1.5, 2.5\}$; the BURA approximation $r_{\alpha,k}(\xi)$ is computed by BRASIL for $\kappa(\mathbb{A}) = 10^{12}$.

3 Approximation of $\mathbb{A}^\beta$

Analogous to (2), in this case we define the BURA approximation via the minimizer

$$\hat{r}_{\beta,k}(\xi) := \min_{r_k \in \mathcal{R}(k)} \max_{\xi \in [\lambda_1, \infty)} |\xi^\beta - r_k(\xi)|$$

for $\beta \in \mathbb{R}^+ \setminus \mathbb{Z}$. In this way we obtain the following approximation of the matrix-vector multiplication $\mathbf{w} = \mathbb{A}^\beta \mathbf{g}$:

$$\mathbf{w} \approx \mathbf{w}_{\hat{r}} := \hat{r}_{\beta,k}(\mathbb{A})\mathbf{g}$$

The following relative error estimate holds true

$$\varepsilon_{bura}^{fmvm} = \frac{||\mathbf{w} - \mathbf{w}_{\hat{r}}||_{\ell_2}}{||\mathbf{g}||_{\ell_2}} \leq \hat{C}_\beta e^{-2\pi\sqrt{k(\lceil\beta\rceil - \beta)}}, \tag{4}$$

where

$$\hat{C}_\beta \approx \kappa^{\lceil\beta\rceil} 4^{1+(\lceil\beta\rceil-\beta)} |\sin \pi(\lceil\beta\rceil - \beta)|,$$

$\kappa = \kappa(\mathbb{A})$ is the spectral condition number of $\mathbb{A}$. The proof of (4) follows from the estimate of the BURA-based approximation in [4], which is an upper bound of $\varepsilon_{bura}^{fmvm}$. For a better comparison, we followed the experimental set-up used to obtain the data of Figure 1, when conducting the numerical experiments shown in Figure 2. Again, for a fixed value of the condition number $\kappa(\mathbb{A})$, the relative error decreases exponentially with respect to the degree of BURA k. However, unlike (2), the estimate (4) is

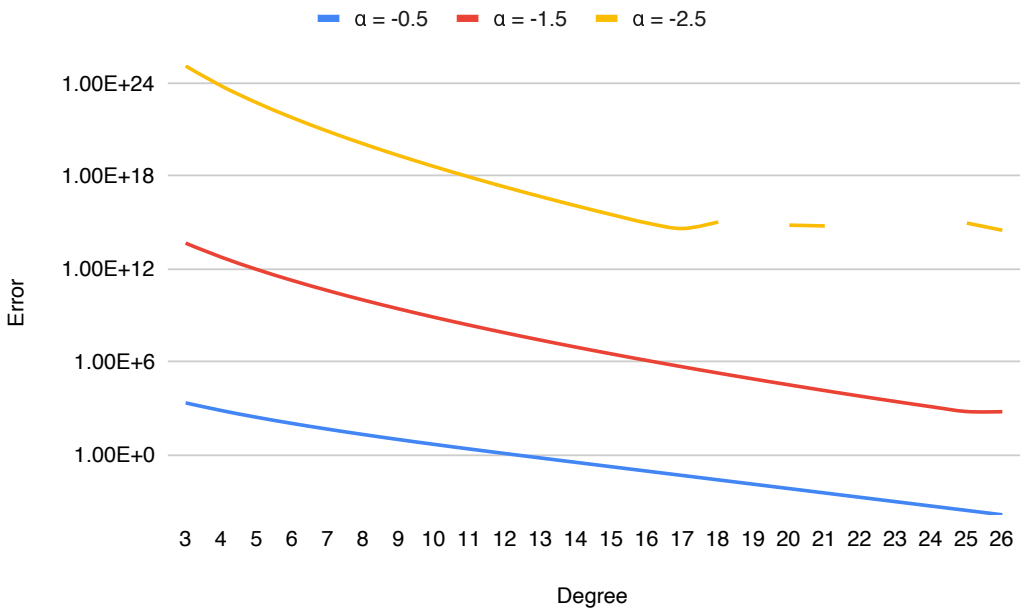

Figure 2: Relative error $\varepsilon_{bura}^{fmvm}$ of the numerical computation of $\mathbb{A}^\beta \mathbf{g}$ which is equivalent to solution of $\mathbb{A}^{-\beta}\mathbf{w} = \mathbf{f}$: $\alpha = -\beta \in \{-0.5, -1.5, -2.5\}$; the BURA approximation $r_{\alpha,k}(\xi)$ is computed by BRASIL for $\kappa(\mathbb{A}) = 10^{12}$.

not robust with respect to $\kappa(\mathbb{A})$. The influence of the condition number of $\mathbb{A}$ increases for larger values of β. Then a BURA approximation of higher degree k will be needed. However, it turns out that in this case there is a problem with the stability of the BRASIL software. This is evident from the atypical behavior and missing parts of the plot for $\alpha = -2.5$ and $k > 16$.

4 Concluding remarks

BURA approximations of $\mathbb{A}^{-\alpha}$ and $\mathbb{A}^\alpha$ for $\alpha \in \mathbb{R}^+ \setminus \mathbb{Z}$ were discussed. Results were presented in the spirit of [4], which significantly extend the scope of the methods analysed in [3]. In all cases considered, the BURA methods converge exponentially with respect to the degree of rational approximation k. However, theoretical estimates and numerical experiments show that the error of BURA approximation of $\mathbb{A}^\alpha$ grows linearly with $(\kappa(\mathbb{A}))^{\lceil\alpha\rceil}$. In this context, it turns out that multiplication by $\mathbb{A}^\alpha$ is computationally more expensive than solving linear systems in the form $\mathbb{A}^\alpha \mathbf{u} = \mathbf{f}$.

Acknowledgements
The work is partially supported by the Bulgarian National Science Fund under grant No. KP-06-N72/2.

References
[1] Stahl, H.: Best uniform rational approximation of x^α on [0,1]. Bull Amer Math Soc (NS). **28**. 116–122 (1993)
[2] Harizanov, S., Lazarov, R., Margenov, S., Marinov, P., Vutov, Y.: Optimal solvers for linear systems with fractional powers of sparse SPD matrices. Numerical Linear Algebra with Applications. **25** (5). e2167. (2018)
[3] Harizanov, S., Lazarov, R., Margenov, S., Marinov, P., Pasciak, J.: Analysis of numerical methods for spectral fractional elliptic equations based on the best uniform rational approximation. J. Comput. Phys. **408**. 109285 (2020)
[4] Kosturski, N., Margenov, S.: Analysis of BURA and BURA-based approximations of fractional powers of sparse SPD matrices. Fract. Calc. Appl. Anal. https://doi.org/10.1007/s13540-024-00256-6 (2024)
[5] Software BRASIL. https://baryrat.readthedocs.io/en/latest/#baryrat.
brasil

* * *

Convergence Analysis of Time-Continuous Strongly Conservative Space-Time Finite Element Methods for the Dynamic Biot Model

J. Kraus

1 Problem formulation

In this presentation, we study the dynamic Biot model for a linear elastic, homogeneous, isotropic, porous solid saturated with a slightly compressible fluid as proposed in [1,2], i.e, the system

$$\bar{\rho}\partial_t^2\boldsymbol{u} - 2\mu\mathrm{div}(\boldsymbol{\epsilon}(\boldsymbol{u})) - \lambda\nabla\mathrm{div}(\boldsymbol{u}) + \alpha\nabla p + \rho_f\partial_t\boldsymbol{w} = \boldsymbol{f} \quad \text{in } \Omega\times(0,T], \tag{1a}$$

$$\rho_f\partial_t^2\boldsymbol{u} + \rho_w\partial_t\boldsymbol{w} + \boldsymbol{K}^{-1}\boldsymbol{w} + \nabla p = \boldsymbol{g} \quad \text{in } \Omega\times(0,T], \tag{1b}$$

$$s_0\partial_t p + \alpha\mathrm{div}(\partial_t\boldsymbol{u}) + \mathrm{div}(\boldsymbol{w}) = 0 \quad \text{in } \Omega\times(0,T], \tag{1c}$$

of partial differential equations in a bounded Lipschitz domain $\Omega\subset\mathbb{R}^d, d\in\{2,3\}$ and $T>0$. The physical parameters in the model are the total density $\bar{\rho} = (1-\phi_0)\rho_s + \phi_0\rho_f > 0$ and the effective fluid density $\rho_w \geq \phi_0^{-1}\rho_f > 0$, where $\rho_s > 0$ represents the solid density, $\rho_f > 0$ the fluid density and $\phi_0\in(0,1)$ the porosity. In addition, the Biot-Willis parameter is specified by $\alpha\in[\phi_0,1]$, cf. [3] and the constrained specific storage coefficient by $s_0>0$, cf. [2]. The Lamé parameters are denoted by $\lambda>0$ and $\mu>0$. Furthermore, $\boldsymbol{\epsilon}(\boldsymbol{u}) = (\nabla\boldsymbol{u} + (\nabla\boldsymbol{u})^\top)/2$ represents the strain tensor, $\boldsymbol{K}$ the symmetric positive definite permeability tensor, $\boldsymbol{f}:\Omega\times[0,T]\to\mathbb{R}^d$ the body force density and $\boldsymbol{g}:\Omega\times[0,T]\to\mathbb{R}^d$ a source term. The unknown physical fields are the displacement $\boldsymbol{u}=\boldsymbol{u}(\boldsymbol{x},t)$, the fluid velocity $\boldsymbol{w}=\boldsymbol{w}(\boldsymbol{x},t)$ and the fluid pressure $p=p(\boldsymbol{x},t)$. Problem (1) is completed by the following initial and boundary conditions

$$\begin{aligned} \boldsymbol{u} &= \boldsymbol{u}_0 \quad \text{in } \Omega\times\{0\}, & \boldsymbol{u} &= \boldsymbol{0} \quad \text{on } \partial\Omega\times(0,T],\\ \partial_t\boldsymbol{u} &= \boldsymbol{v}_0 \quad \text{in } \Omega\times\{0\}, & \boldsymbol{w}\cdot\boldsymbol{n} &= 0 \quad \text{on } \partial\Omega\times(0,T],\\ p &= p_0 \quad \text{in } \Omega\times\{0\}. \end{aligned} \tag{2}$$

As it can be shown using Picard's theorem [Thm. 6.2.1, 4], problem (1)–(2) is well-posed.

2 Variational formulations

To begin with, we introduce the variable $\boldsymbol{v} := \partial_t \boldsymbol{u}$ and rewrite problem (1) as

$$\bar{\rho}\partial_t \boldsymbol{v} - 2\mu \mathrm{div}(\boldsymbol{\epsilon}(\boldsymbol{u})) - \lambda \nabla \mathrm{div}(\boldsymbol{u}) + \alpha \nabla p + \rho_f \partial_t \boldsymbol{w} = \boldsymbol{f} \quad \text{in } \Omega \times (0,T], \tag{3a}$$

$$\partial_t \boldsymbol{u} - \boldsymbol{v} = \boldsymbol{0} \quad \text{in } \Omega \times (0,T], \tag{3b}$$

$$\rho_f \partial_t \boldsymbol{v} + \rho_w \partial_t \boldsymbol{w} + \boldsymbol{K}^{-1}\boldsymbol{w} + \nabla p = \boldsymbol{g} \quad \text{in } \Omega \times (0,T], \tag{3c}$$

$$s_0 \partial_t p + \alpha \mathrm{div}(\partial_t \boldsymbol{u}) + \mathrm{div}(\boldsymbol{w}) = 0 \quad \text{in } \Omega \times (0,T]. \tag{3d}$$

In the following, we present a time-continuous as well as a time-discrete variational formulation of problem (3). For the discrete problem, we utilize a discontinuous Galerkin methods in space.

2.1 Space-time variational problem

In order to give a space-time variational formulation of problem (3), we define the following spaces

$$\begin{aligned} \boldsymbol{U} = \boldsymbol{V} &:= \boldsymbol{H}_0^1(\Omega) = \{\boldsymbol{u} \in \boldsymbol{H}^1(\Omega) : \boldsymbol{u} = \boldsymbol{0} \text{ on } \partial\Omega\}, \\ \boldsymbol{W} &:= \boldsymbol{H}_0(\mathrm{div}, \Omega) = \{\boldsymbol{w} \in \boldsymbol{H}(\mathrm{div}, \Omega) : \boldsymbol{w} \cdot \boldsymbol{n} = 0 \text{ on } \partial\Omega\}, \\ P &:= L_0^2(\Omega) = \{p \in L^2(\Omega) : \int_\Omega p \mathrm{d}\boldsymbol{x} = 0\}, \\ \boldsymbol{X} &:= \boldsymbol{U} \times \boldsymbol{V} \times \boldsymbol{W} \times P, \end{aligned} \tag{4}$$

and bilinear forms

$$a(\boldsymbol{u}, \boldsymbol{\varphi}^{\boldsymbol{u}}) := 2\mu \left(\boldsymbol{\epsilon}(\boldsymbol{u}), \boldsymbol{\epsilon}(\boldsymbol{\varphi}^{\boldsymbol{u}})\right) + \lambda \left(\mathrm{div}(\boldsymbol{u}), \mathrm{div}(\boldsymbol{\varphi}^{\boldsymbol{u}})\right), \tag{5a}$$

$$b(p, \boldsymbol{\varphi}^{\boldsymbol{w}}) := \left(p, \mathrm{div}(\boldsymbol{\varphi}^{\boldsymbol{w}})\right), \tag{5b}$$

for $\boldsymbol{u}, \boldsymbol{\varphi}^{\boldsymbol{u}} \in \boldsymbol{U}, \boldsymbol{\varphi}^{\boldsymbol{w}} \in \boldsymbol{W}, p \in P$. Next, we pose the time-continuous weak problem:

Problem 2.1. *Let $\boldsymbol{f}, \boldsymbol{g} \in W^{1,1}([0,T]; \boldsymbol{L}^2(\Omega))$ and $(\boldsymbol{u}_0, \boldsymbol{v}_0, \boldsymbol{w}_0, p_0) \in \boldsymbol{X}$ be given. Additionally, let $p_0 \in H_0^1(\Omega)$ and $\mathrm{div}(2\mu\boldsymbol{\epsilon}(\boldsymbol{u}_0) + \lambda \mathrm{div}(\boldsymbol{u}_0)\boldsymbol{I} - \alpha p_0 \boldsymbol{I}) \in \boldsymbol{L}^2(\Omega)$. Then we seek $(\boldsymbol{u}, \boldsymbol{v}, \boldsymbol{w}, p) \in L^2(I; \boldsymbol{X})$ such that $\boldsymbol{u}(\cdot, 0) = \boldsymbol{u}_0,\ \boldsymbol{v}(\cdot, 0) = \boldsymbol{v}_0,\ \boldsymbol{w}(\cdot, 0) = \boldsymbol{w}_0,\ p(\cdot, 0) = p_0$, and*

$$\int_I (\bar{\rho}\partial_t \boldsymbol{v} + \rho_f \partial_t \boldsymbol{w}, \boldsymbol{\varphi}^{\boldsymbol{u}}) + a(\boldsymbol{u}, \boldsymbol{\varphi}^{\boldsymbol{u}}) - (\alpha p, \mathrm{div}(\boldsymbol{\varphi}^{\boldsymbol{u}}))\,\mathrm{d}t = \int_I (\boldsymbol{f}, \boldsymbol{\varphi}^{\boldsymbol{u}})\,\mathrm{d}t, \tag{6a}$$

$$\int_I (\partial_t \boldsymbol{u} - \boldsymbol{v}, \boldsymbol{\varphi}^{\boldsymbol{v}})\,\mathrm{d}t = 0, \tag{6b}$$

$$\int_I \left(\rho_f \partial_t \boldsymbol{v} + \rho_w \partial_t \boldsymbol{w} + \boldsymbol{K}^{-1}\boldsymbol{w}, \boldsymbol{\varphi}^{\boldsymbol{w}}\right) - b(p, \boldsymbol{\varphi}^{\boldsymbol{w}})\mathrm{d}t = \int_I (\boldsymbol{g}, \boldsymbol{\varphi}^{\boldsymbol{w}})\,\mathrm{d}t, \tag{6c}$$

$$\int_I (s_0 \partial_t p + \alpha \mathrm{div}(\partial_t \boldsymbol{u}), \varphi^p) + b(\varphi^p, \boldsymbol{w})\mathrm{d}t = 0, \tag{6d}$$

for all $(\boldsymbol{\varphi}^{\boldsymbol{u}}, \boldsymbol{\varphi}^{\boldsymbol{v}}, \boldsymbol{\varphi}^{\boldsymbol{w}}, \varphi^p) \in L^2(I; \boldsymbol{X})$.

The well-posedness of Problem 2.1 is proven in [5].

2.2 Discontinuous Galerkin method

Here, we utilize a continuous Galerkin-Petrov (cGP(k)) method in time of degree $k \in \mathbb{N}$ for problem (3). With this time stepping scheme, we end up with a globally continuous solution in time. For the spatial

discretization, we exploit a discontinuous Galerkin (DG) method for the displacement $\boldsymbol{u}$. To this end, we define the discrete spaces

$$\begin{aligned}\boldsymbol{U}_h = \boldsymbol{V}_h &:= \{\boldsymbol{u}_h \in \boldsymbol{H}(\mathrm{div},\Omega) : \boldsymbol{u}_h\big|_K \in \boldsymbol{U}(K) \quad \forall K \in \mathcal{T}_h \text{ and } \boldsymbol{u}\cdot\boldsymbol{n} = 0 \text{ on } \partial\Omega\},\\ \boldsymbol{W}_h &:= \{\boldsymbol{w}_h \in \boldsymbol{H}(\mathrm{div},\Omega) : \boldsymbol{w}_h\big|_K \in \boldsymbol{W}(K) \quad \forall K \in \mathcal{T}_h \text{ and } \boldsymbol{w}\cdot\boldsymbol{n} = 0 \text{ on } \partial\Omega\},\\ P_h &:= \{p_h \in L^2_0(\Omega) : p_h\big|_K \in P(K) \quad \forall K \in \mathcal{T}_h\},\\ \boldsymbol{X}_h &:= \boldsymbol{U}_h \times \boldsymbol{V}_h \times \boldsymbol{W}_h \times P_h,\end{aligned} \tag{7}$$

where $\boldsymbol{U}(K)\times\boldsymbol{W}(K)\times P(K)$ here are chosen to be $\mathrm{BDM}_{\ell+1}(K)\times\mathrm{BDM}_{\ell+1}(K)\times\mathbb{P}_\ell(K)$ for $\ell\geq 0$. The space $\mathrm{BDM}_\ell(K)$ denotes the Brezzi-Douglas-Marini space of order $\ell\in\mathbb{N}$.

In order to obtain mass conservation, we require $\mathrm{div}(\boldsymbol{U}_h)\subseteq P_h$ and $\mathrm{div}(\boldsymbol{W}_h)\subseteq P_h$, see [6]. For the discontinuous Galerkin method, we will partition the domain Ω by a shape-regular triangulation $\mathcal{T}_h$. Let $\{\!\{\cdot\}\!\}$ be the average and $[\![\cdot]\!]$ the jump defined by

$$\{\!\{\boldsymbol{\tau}\}\!\} := \frac{1}{2}\left(\boldsymbol{\tau}\big|_{\partial K_1\cap e}\boldsymbol{n}_1 - \boldsymbol{\tau}\big|_{\partial K_2\cap e}\boldsymbol{n}_2\right), \qquad [\![\boldsymbol{y}]\!] := \boldsymbol{y}\big|_{\partial K_1\cap e} - \boldsymbol{y}\big|_{\partial K_2\cap e},$$

for any interior facet (edge in 2D and face in 3D) $e := K_1\cap K_2$ and $\{\!\{\boldsymbol{\tau}\}\!\} := \boldsymbol{\tau}\big|_e\boldsymbol{n}$, $[\![\boldsymbol{y}]\!] := \boldsymbol{y}\big|_e$, for any boundary facet e, where $\boldsymbol{\tau}$ denotes a matrix-valued and $\boldsymbol{y}$ a vector-valued function, see e.g. [7]. Additionally, we specify the tangential component by $\mathrm{tang}(\boldsymbol{z}) := \boldsymbol{z} - (\boldsymbol{z}\cdot\boldsymbol{n})\boldsymbol{n}$. Next, we introduce the bilinear forms

$$\begin{aligned}a_h(\boldsymbol{u}_{\tau,h},\boldsymbol{\varphi}^{\boldsymbol{u}}_{\tau,h}) := &\sum_{K\in\mathcal{T}_h} 2\mu\int_K \boldsymbol{\epsilon}(\boldsymbol{u}_{\tau,h}) : \boldsymbol{\epsilon}(\boldsymbol{\varphi}^{\boldsymbol{u}}_{\tau,h})\mathrm{d}\boldsymbol{x}\\ &- \sum_{e\in\mathcal{E}_h} 2\mu\int_e \{\!\{\boldsymbol{\epsilon}(\boldsymbol{u}_{\tau,h})\}\!\}\cdot[\![\mathrm{tang}(\boldsymbol{\varphi}^{\boldsymbol{u}}_{\tau,h})]\!]\mathrm{d}s - \sum_{e\in\mathcal{E}_h} 2\mu\int_e \{\!\{\boldsymbol{\epsilon}(\boldsymbol{\varphi}^{\boldsymbol{u}}_{\tau,h})\}\!\}\cdot[\![\mathrm{tang}(\boldsymbol{u}_{\tau,h})]\!]\mathrm{d}s\\ &+ \sum_{e\in\mathcal{E}_h} 2\mu\eta h_e^{-1}\int_e [\![\mathrm{tang}(\boldsymbol{u}_{\tau,h})]\!]\cdot[\![\mathrm{tang}(\boldsymbol{\varphi}^{\boldsymbol{u}}_{\tau,h})]\!]\mathrm{d}s + \lambda\left(\mathrm{div}(\boldsymbol{u}_{\tau,h}),\mathrm{div}(\boldsymbol{\varphi}^{\boldsymbol{u}}_{\tau,h})\right)\end{aligned}$$

and $b_h(p_{\tau,h},\boldsymbol{\varphi}^{\boldsymbol{w}}_{\tau,h}) := \left(p_{\tau,h},\mathrm{div}(\boldsymbol{\varphi}^{\boldsymbol{w}}_{\tau,h})\right)$, where h_e is the diameter of the facet e, the set $\mathcal{E}_h$ contains all facets, and η is a stabilization parameter, cf. [7]. Using block vectors for all unknowns, i.e., $\boldsymbol{x}_{\tau,h} := (\boldsymbol{u}^\top_{\tau,h},\boldsymbol{v}^\top_{\tau,h},\boldsymbol{w}^\top_{\tau,h},p_{\tau,h})^\top$ and approximation of initial values, i.e., $\boldsymbol{x}_{0,h} := (\boldsymbol{u}^\top_{0,h},\boldsymbol{v}^\top_{0,h},\boldsymbol{w}^\top_{0,h},p_{0,h})$ enables us to give a short representation of the DG method:

Problem 2.2. *Let $k,\ell\in\mathbb{N}$ and $\boldsymbol{x}^{n-1}_{\tau,h} := \boldsymbol{x}_{\tau,h}(t_{n-1})$ be given where $\boldsymbol{x}_{\tau,h}(t_0) = \boldsymbol{x}_{0,h}$. Find $\boldsymbol{x}_{\tau,h}\in\mathbb{P}_k(I_n;\boldsymbol{X}_h)$ such that $\boldsymbol{x}_{\tau,h}(t_{n-1}) = \boldsymbol{x}^{n-1}_{\tau,h}$ and*

$$\int_{I_n}\left(\bar\rho\partial_t\boldsymbol{v}_{\tau,h} + \rho_f\partial_t\boldsymbol{w}_{\tau,h},\boldsymbol{\varphi}^{\boldsymbol{u}}_{\tau,h}\right) + a_h(\boldsymbol{u}_{\tau,h},\boldsymbol{\varphi}^{\boldsymbol{u}}_{\tau,h}) - \left(\alpha p_{\tau,h},\mathrm{div}(\boldsymbol{\varphi}^{\boldsymbol{u}}_{\tau,h})\right)\mathrm{d}t = \int_{I_n}\left(\mathfrak{I}^*_\tau\boldsymbol{f},\boldsymbol{\varphi}^{\boldsymbol{u}}_{\tau,h}\right)\mathrm{d}t, \tag{8a}$$

$$\int_{I_n}\left(\partial_t\boldsymbol{u}_{\tau,h} - \boldsymbol{v}_{\tau,h},\boldsymbol{\varphi}^{\boldsymbol{v}}_{\tau,h}\right)\mathrm{d}t = 0, \tag{8b}$$

$$\int_{I_n}\left(\rho_f\partial_t\boldsymbol{v}_{\tau,h} + \rho_w\partial_t\boldsymbol{w}_{\tau,h} + \boldsymbol{K}^{-1}\boldsymbol{w}_{\tau,h},\boldsymbol{\varphi}^{\boldsymbol{w}}_{\tau,h}\right) - b_h(p_{\tau,h},\boldsymbol{\varphi}^{\boldsymbol{w}}_{\tau,h})\mathrm{d}t = \int_{I_n}\left(\mathfrak{I}^*_\tau g,\boldsymbol{\varphi}^{\boldsymbol{w}}_{\tau,h}\right)\mathrm{d}t, \tag{8c}$$

$$\int_{I_n}\left(s_0\partial_t p_{\tau,h} + \alpha\mathrm{div}(\partial_t\boldsymbol{u}_{\tau,h}),\varphi^p_{\tau,h}\right) + b_h(\varphi^p_{\tau,h},\boldsymbol{w}_{\tau,h})\mathrm{d}t = 0, \tag{8d}$$

for all $(\boldsymbol{\varphi}^{\boldsymbol{u}}_{\tau,h},\boldsymbol{\varphi}^{\boldsymbol{v}}_{\tau,h},\boldsymbol{\varphi}^{\boldsymbol{w}}_{\tau,h},\varphi^p_{\tau,h})\in\mathbb{P}_{k-1}(I_n;\boldsymbol{X}_h)$.

Here $\mathfrak{I}^*_\tau$ denotes any interpolation operator that locally is defined via $k+1$ points on I_n, $n = 1,\dots,N$.

3 Error analysis

Using the notation $\boldsymbol{M}_\rho := \begin{pmatrix} \bar{\rho}\boldsymbol{I} & \rho_f \boldsymbol{I} \\ \rho_f \boldsymbol{I} & \rho_w \boldsymbol{I} \end{pmatrix}$,

$$\|\boldsymbol{u}_h\|_{\mathrm{DG}}^2 := \sum_{K\in\mathcal{T}_h} \|\nabla \boldsymbol{u}_h\|_{L^2(K)}^2 + \sum_{e\in\mathcal{E}_h} h_e^{-1} \|[\![\mathrm{tang}(\boldsymbol{u}_h)]\!]\|_{L^2(e)}^2 + \sum_{K\in\mathcal{T}_h} h_K^2 |\boldsymbol{u}_h|_{H^2(K)}^2, \tag{9a}$$

$$\|\boldsymbol{u}_h\|_{\boldsymbol{U}_h}^2 := \|\boldsymbol{u}_h\|_{\mathrm{DG}}^2 + \|\mathrm{div}(\boldsymbol{u}_h)\|_{L^2(\Omega)}^2, \tag{9b}$$

where h_K represents the diameter of the element K, we have the following error estimate for the solution of Problem 2.2, see [8].

Theorem 3.1. *There holds*

$$\|\boldsymbol{u}_{\tau,h} - \boldsymbol{u}\|_{L^\infty(I;\boldsymbol{U}_h)}^2 + \|\boldsymbol{M}_\rho^{1/2} \begin{pmatrix} \boldsymbol{v}_{\tau,h} - \boldsymbol{v} \\ \boldsymbol{w}_{\tau,h} - \boldsymbol{w} \end{pmatrix}\|_{L^\infty(I;\boldsymbol{L}^2)}^2 + \|\boldsymbol{K}^{-1/2}(\boldsymbol{w}_{\tau,h} - \boldsymbol{w})\|_{L^\infty(I;\boldsymbol{L}^2)}^2$$
$$+ s_0 \|p_{\tau,h} - p\|_{L^\infty(I;L^2)}^2 \le c\left(\tau^{2(k+1)} + h^{2(\ell+1)}\right) \|(\boldsymbol{u},\boldsymbol{w},p)\|_I^2 + c\tau^{2k+2} \|\partial_t^{k+1} \begin{pmatrix} \boldsymbol{f} \\ \boldsymbol{g} \end{pmatrix}\|_{L^2(I;\boldsymbol{L}^2)}^2.$$

4 Conclusion

We propose a family of time-continuous strongly conservative space-time finite element methods for the dynamic Biot model. These methods combine a Galerkin-Petrov scheme for time discretization, which constructs a continuous solution in time, with a discontinuous Galerkin method for the displacement and a mixed space discretization for the fluid flux, fluid pressure and the time derivative of the displacement. We prove optimal error estimates in energy norm.

Acknowledgments The authors acknowledge the funding by the German Science Fund (DFG) as part of the project "Physics-oriented solvers for multicompartmental poromechanics" under grant number 456235063.

References

[1] M. A. Biot. General theory of three-dimensional consolidation. *J. Appl. Phys.*, 12(2):155–164, 1941.

[2] M. A. Biot. Mechanics of deformation and acoustic propagation in porous media. *J. Appl. Phys.*, 33(4):1482–1498, 1962.

[3] M. A. Biot and D. G. Willis. The elastic coefficients of the theory of consolidation. *Journal of Applied Mechanics*, 24:594–601, 1957.

[4] C. Seifert, S. Trostorff, and M. Waurick. *Evolutionary equations - Picard's theorem for partial differential equations and applications*. Birkhäuser Cham, 1 edition, 2022.

[5] A. Mielke and E. Rohan. Homogenization of elastic waves in fluid-saturated porous media using the Biot model. *Math. Models Methods Appl. Sci.*, 23(5), 2013.

[6] B. Cockburn, G. Kanschat, and D. Schötzau. A note on discontinuous Galerkin divergence-free solutions of the Navier-Stokes equations. *J. Sci. Comput.*, 31(1-2):61–73, 2007.

[7] Q. Hong and J. Kraus. Parameter-robust stability of classical three-field formulation of Biot's consolidation model. *Electron. Trans. Numer. Anal.*, pages 202–226, 2018.

[8] J. Kraus, M. Lymbery, K. Osthues, and F. Philo. Analysis of a family of time-continuous strongly conservative space-time finite element methods for the dynamic Biot model. *arXiv:2401.04609 [math.NA]*, 2024.

* * *

Numerical Solution of Parabolic Equations: from Local to Non-Local in Space Problems

S. Margenov

Let us consider the parabolic equation

$$\frac{\partial u(x,t)}{\partial t} + \mathcal{L}u(x,t) = f(x,t), \quad \forall (x,t) \in \Omega \times [0,T], \tag{1}$$

$$u(x,t) = 0, \quad \forall (x,t) \in \partial\Omega \times [0,T], \quad \text{and } u(x,0) = u_0(x) \quad \forall x \in \Omega,$$

where $\mathcal{L}$ is a second order linear elliptic operator in a given multidimensional domain Ω. In physics, it describes the macroscopic behaviour of many micro-particles. Under some circumstances, (1) is equivalent to the heat equation.

We now introduce a uniform mesh with a time step $\tau = T/M$ and consider the backward Euler

$$\frac{u^{j+1}(x) - u^j(x)}{\tau} + \mathcal{L}u^{j+1}(x) = f^{j+1}(x) \tag{2}$$

and the Crank-Nicolson

$$\frac{u^{j+1}(x) - u^j(x)}{\tau} + \frac{\mathcal{L}u^{j+1}(x) + \mathcal{L}u^j(x)}{2} = \frac{f^{j+1}(x) + f^j(x)}{2} \tag{3}$$

methods where $j = 0, \ldots, M-1$, $u^j(x) = u(x, j\tau)$ and $f^j(x) = f(x, j\tau)$. The finite difference scheme (2) is of first order, i.e. has $O(\tau)$ accuracy, while the second-order scheme (3) has $O(\tau^2)$ accuracy. At the operator level, each time step of the backward Euler method involves solving one equation which can be written in the form $(\mathcal{L} + 1/\tau\mathcal{I})u^{j+1}(x) = F^j(x)$, while in the of Crank-Nicolson method, $\mathcal{L}u^j(x)$ has to be performed in addition. Here $\mathcal{I}$ denotes the identity operator. How different the complexities of the semi-discrete schemes (2) and (3) are depends on the operator $\mathcal{L}$.

In the case of standard (local) diffusion, $\mathcal{L} = \mathcal{A}$, $\mathcal{A}$ is a self-adjoin positive definite differentiation operator associated with the bilinear form $a(u,v) = \int_\Omega D\nabla u \nabla v d\Omega$, D is the matrix of diffusion coefficients. There have been many years of successful work in the development of numerical methods in this case. The situation changes significantly when $\mathcal{L} = \mathcal{A}^\alpha$, $\alpha \in (0,1)$ and the equation (1) describes anomalous diffusion (sub-diffusion). Then the operator $\mathcal{L}$ is non-local. The challenges in the transition from local to non-local parabolic equations are the focus of this study.

Mesh methods such as finite element method (FEM) and finite difference method (FDM) are among the most used in approximating $\mathcal{A}$ and then $\mathcal{A}^\alpha$ [1]. For simplicity of presentation, we will assume that FDM is applied on a uniform rectangular mesh ω_h , with mesh parameter h and N internal nodes and a 3-point stencil in each coordinate direction. Then the fully discrete backward Euler and Crank-Nicolson schemes are written in the form

$$\frac{\mathbf{u}^{j+1} - \mathbf{u}^j}{\tau} + \mathbb{A}^\alpha \mathbf{u}^{j+1} = \mathbf{f}^{j+1} \tag{4}$$

and

$$\frac{\mathbf{u}^{j+1} - \mathbf{u}^j}{\tau} + \frac{\mathbb{A}^\alpha \mathbf{u}^{j+1} + \mathbb{A}^\alpha \mathbf{u}^j}{2} = \frac{\mathbf{f}^{j+1} + \mathbf{f}^j}{2} \tag{5}$$

respectively. Here $\mathbb{A} \in \mathbb{R}^{N \times N}$ is a sparse, symmetric and positive definite (SPD) matrix obtained as the FDM approximation of $\mathcal{A}$, and $\mathbf{u}^j$ and $\mathbf{f}^j$ are the vectors of nodal values of $u^j(x)$ and $f^j(x)$ respectively. The accuracy in the L^2 norm of approximating $\mathcal{A}^\alpha$ by $\mathbb{A}^\alpha$ is essentially $O(h^{2\alpha})$.

In the case of standard diffusion, i.e. when $\alpha = 1$, given that $\mathbb{A}$ is sparse, the computational complexity of one time step in both, (4) and (5), is dominated by solving a linear system with $\mathbb{A} + 1/\tau\mathbb{I}$, $\mathbb{I}$ is the identity matrix. We can think of using a suitable fast preconditioned conjugate gradient (PCG) solver for this purpose.

Non-local fractional diffusion is characterized by the loss of sparsity of the discrete operator. The matrix $\mathbb{A}^\alpha$ is SPD but dense. The first key issue for efficient implementation of the backward Euler and Crank-Nicolson schemes, (4) and (5), is the numerical solution of linear systems that can be written in the form

$$\left(\mathbb{A}^\alpha + \frac{1}{\tau}\mathbb{I}\right)\mathbf{u}^{k+1} = \mathbf{F}^k. \tag{6}$$

Unlike the case of standard diffusion, now the matrix-vector multiplication $\mathbf{w}^k = \mathbb{A}^\alpha\mathbf{u}^k$ has a significant impact on the computational complexity of (5).

The numerical solution of spectral fractional diffusion equations in multidimensional domains has been studied very actively in the last decade. As it was shown, the proposed several methods for solving the fractional Laplacian equation, quite different in their origin, can be interpreted as some rational approximation of $\mathcal{A}^{-\alpha}$. Here we further develop the concept of BURA methods, which were originally defined by the best uniform rational approximation of z^α in the interval $[0, 1]$, see [1,2].

A more direct approach will be applied in this work. The studied BURA methods correspond to the minimizer $r_{q,\alpha,k}(\xi) = P_k(\xi)/Q_k(\xi) \in \mathcal{R}(k)$ defined as

$$r_{q,\alpha,k}(\xi) := \min_{r_k\in\mathcal{R}(k)} \max_{\xi\in[\underline{\Lambda},\infty]} \left|\frac{1}{\xi^\alpha + q} - r_k(\xi)\right|,$$

where $\underline{\Lambda} > 0$ is a lower bound of the minimal eigenvalue of $\mathbb{A}$. According to this framework, the BURA approximation of the solution of the system (6) is defined as

$$\mathbf{u}^{k+1} \approx \mathbf{u}_r^{k+1} := r_{1/\tau,\alpha,k}(\mathbb{A})\mathbf{F}^k.$$

The following relative error estimate characterizes this approximation

$$\frac{||\mathbf{u}^{k+1} - \mathbf{u}_r^{k+1}||_\ell}{||\mathbf{F}^k||_\ell} = O(\tau e^{\sqrt{k}}). \tag{7}$$

The presented result is consistent with [3] as well as the more recent rigorous analysis in [4]. Then, following [5], we consider the BURA-based approximation of $\mathbf{w}^k = \mathbb{A}^\alpha\mathbf{u}^k$ in the form

$$\mathbf{w}^k \approx \mathbf{w}_r^k := \mathbb{A}r_{0,1-\alpha,k}(\mathbb{A})\mathbf{u}^k.$$

The relative error of this approximation satisfies the estimate

$$\frac{||\mathbf{w}^k - \mathbf{w}_r^k||_\ell}{||\mathbf{u}^k||_\ell} = O(\kappa^\alpha e^{\sqrt{k}}) \tag{8}$$

where $\kappa = \kappa(\mathbb{A})$ denotes the spectral condition number of $\mathbb{A}$. Estimates (7) and (8) show that multiplying a vector by $\mathbb{A}^\alpha$ is computationally more difficult (expensive) than solving linear systems with such a matrix. Some readers may be quite surprised by such a conclusion, which completely distinguishes fractional from standard diffusion.

Using (7) and (8), sufficient conditions for balancing errors of different origins are obtained. In this way, consistent error estimates with respect to the discretization parameters h and τ are derived. As a result of the analysis, estimates of the computational complexity were obtained in terms of the number of degrees of freedom M and N. In conclusion, the developed BURA-based composite methods and algorithms have near-optimal complexity, essentially on the order of $O(MN \log N)$.

Acknowledgements
The work is partially supported by the Bulgarian National Science Fund under grant No. KP-06-N72/2.

References
[1] Harizanov, S., Lazarov, R., Margenov, S.: A survey on numerical methods for spectral space-fractional diffusion problems. Fractional Calculus and Applied Analysis. **23** (6). 1605–1646 (2020)
[2] Harizanov, S., Lazarov, R., Margenov, S., Marinov, P., Pasciak, J.: Analysis of numerical methods for spectral fractional elliptic equations based on the best uniform rational approximation. J. Comput. Phys. **408**. 109285 (2020)
[3] Harizanov, S., Lazarov, R., Margenov S., Marinov, P.: Numerical solution of fractional diffusion-reaction problems based on BURA. Computers & Mathematics with Applications. **80** (2). 316–331 (2020)
[4] Duan, B., Yang, Z.: A Quadrature Scheme for Steady-State Diffusion Equations Involving Fractional Power of Regularly Accretive operator. SIAM Journal on Scientific Computing, **45** (5). A2226-–A2249 (2023)
[5] Kosturski, N., Margenov, S.: Analysis of BURA and BURA-based approximations of fractional powers of sparse SPD matrices. Fract. Calc. Appl. Anal. https://doi.org/10.1007/s13540-024-00256-6 (2024)

* * *

Three Krylov Subspace Iteration Methods that Incorporate Variable Preconditioning

M. Neytcheva, M. Pourbagher

Since long, when solving large scale linear algebraic systems of equations, in particular with sparse matrices, Krylov subspace iteration methods have been established to be the methods of choice. The reasons to be so widely used are that these methods are parameter-free, they possess finite termination property, optimality approximation property and the influence of roundoff error is usually acceptable. These methods have favourable memory requirements and computational complexity per iteration. Further, the use of a good preconditioner can significantly improve their performance.

When solving linear systems of equations with a general nonsymmetric matrix, currently there are three Krylov subspace iteration methods, known to handle variable preconditioning, namely, the Generalized Conjugate Gradient (GCG) method, the Flexible Generalized Minimal Residual (FGMRES) method and the Generalized Conjugate Residual (GCR) method.

Peeking in the history of their development unveils the following chronology.

GCG was first published with this name in [1] in its Least Squares form. However, the ideas have been published earlier in [2] and [3]. In its second form, GCG-Minimal Residual (GCGMR) it is published in [4], together with its convergence analysis and ability to handle variable preconditioning. Relevant ideas are also published in [5].

The GMRES method is first published in [6]. Formally, looking at the year of publication, GMRES seems to have won the competition for a most popular Krylov subspace iteration method for solving linear systems with general nonsymmetric matrices and is made available in all numerical linear algebra packages, offering iterative solvers. However, in its original form it does not incorporate variable preconditioning and may diverge.

The GMRES upgrade, the Flexible GMRES, which can handle variable preconditioning appears in [7], about two years after GCG.

The original derivation of the GCR method is found in [8].

Below we provide a description of the GCGMR, FGMRES and GCR algorithms. The presentation will discuss their similarities and differences, as well as the easiness of their implementation easiness, memory footprint and convenience in accessing the methods' ingredients.

To facilitate the presentation we introduce some notations. We aim at solving the linear system of equations

$$A\boldsymbol{x} = \boldsymbol{b}, \tag{1}$$

using a preconditioned Krylov subspace iteration method, where $A \in \mathbb{R}^{n\times n}$, $\boldsymbol{x}, \boldsymbol{b}$ are vectors in $\mathbb{R}^n$. We denote the iterative solutions per iteration k as $\boldsymbol{x}^{(k)}$ for $k = 0, 1, \cdots$, where $\boldsymbol{x}^{(0)}$ is given and let $\boldsymbol{r}^{(k)} = \boldsymbol{b} - A\boldsymbol{x}^{(k)}$ be the corresponding residuals. Here the matrix A may not be available in an explicit form but we assume that we can compute its action on a vector. We denote the Krylov subspace, built during the iterations as $\mathcal{K}_k(A, \boldsymbol{r}^{(0)})$ and by $\mathcal{G}_k = \{\boldsymbol{g}^{(0)}, \boldsymbol{g}^{(1)}, \cdots, \boldsymbol{g}^{(k-1)}\}$ a basis of $\mathcal{K}_k(A, \boldsymbol{r}^{(0)})$.

Below P denotes a preconditioner, which does not have to be explicitly defined and can vary from one iteration to another. The only recuirement we impose is that we can solve a system with it and we denote the action of its inverse on a vector as $P^{-1}[\boldsymbol{w}]$.

The Generalised Conjugate Gradient method

The derivation of GCG is based on the the following assumptions. Instead for solving the system $A\boldsymbol{x} = \boldsymbol{b}$ we derive the method for the equivalent system $B\boldsymbol{x} = \boldsymbol{g}$, where $B = PA$, $B = AP$ or $B = P^{-1}A$ and P is some preconditioner to A. We also assume that we have defined two scalar products $(\cdot,\cdot)_0 = (\cdot, M_0\cdot)$ and $(\cdot,\cdot)_1 = (\cdot, M_1\cdot)$, where M_0 and M_1 are two symmetric and positive matrices.

The system $B\boldsymbol{x} = \boldsymbol{g}$ is solved by an iterative method, based on minimizing the quadratic functional $f(\boldsymbol{x}) = \frac{1}{2}(\boldsymbol{r}, \boldsymbol{r})_0 = \frac{1}{2}(B\boldsymbol{x} - \boldsymbol{g}, B\boldsymbol{x} - \boldsymbol{g})_0$. Algorithm 3 shows how GCGMR can be implemented (as in [4], Algorithm 2).

As already mentioned, GCG is derived in two frameworks - Least Squares (GCGLS) and Minimal Residual (GCGMR). The derivations and convergence estimates can be found, for instance, in [4,10].

Algorithm GCG

The computational procedure is presented in Algorithm 3. It is important to note, that the matrix $\Lambda^{(j)}$ is symmetric and positive definite. At each iteration it is extended by one row and column. iteration The method can be further tuned by the choices of the two scalar projects, i.e., choosing particular matrices M_0 and M_1. From the general form of the algorithm we see that we have to store vector sequences $\boldsymbol{d}^{(i)}$, $A\boldsymbol{d}^{(i)}$. The method has a final termination property, a restarted version with proven convergence and for certain choices of the scalar products and the way to compute the search directions, its computational cost is analogous to that of GMRES and GCR.

The Flexible Generalized Minimal Residual method

For clarity of the presentation we include first the algorithm of the standard GMRES (as in [9] and then that of FGMRES, to facilitate the discussion of the differences between the two methods.

Algorithm GMRES

In Algorithm 4, $\boldsymbol{e}_1$ is a vector of size k with first component 1 and the rest - 0. The matrix $V_k = [\boldsymbol{v}^{(1)}, \cdots, \boldsymbol{v}^{(k)}]$ consists of the computed basis vectors in the Krylov subspace $\mathcal{K}_k$.

Steps 3-12 define the Arnoldi process, during which we construct an orthogonal basis of the preconditioned Krylov subspace $\mathcal{K}_k = \{\boldsymbol{r}^{(0)}, AP^{-1}\boldsymbol{r}^{(0)}, \cdots, (AP^{-1})^{k-1}\boldsymbol{r}^{(0)}\}$.

Algorithm 4 requires to store the set of vectors $\boldsymbol{v}^{(i)}$. As the preconditioner is assumed to be fixed, it suffices to apply P the the linear combination of the vectors $\boldsymbol{v}$, namely, to $V_k\boldsymbol{y}^{(k)}$.

Algorithm 3 The GCG algorithm

Choose a maximum number of iterations k, define a matrix $\Lambda_k = \{\Lambda_{i,j}\}$ of size $k \times k$ and set it to zero. Let P be a preconditioner and $\varepsilon > 0$ be some apriori chosen stopping tolerance.
Given $\boldsymbol{x}^{(0)}$, compute $\boldsymbol{r}^{(0)} = A\boldsymbol{x}^{(0)} - \boldsymbol{b}$, $\boldsymbol{d}^{(0)} = -\boldsymbol{r}^{(0)}$
for $j = 1, \cdots, k$ **do**
    Compute $\boldsymbol{v}^{(j)} = A\boldsymbol{d}^{(j-1)}$
    Construct $\Lambda^{(j)} : \Lambda^{(j)}_{i,\ell} = (\boldsymbol{v}^{(j-1)}, \boldsymbol{v}^{(j-i)})_0$, $1 \le i \le j$, $\gamma^{(j)} = [0, \cdots, 0, -(r^{(j-1)}, \boldsymbol{v}^{(j-1)})_0]^T$
    Solve $\Lambda^{(j)}\alpha^{(j)} = \gamma^{(j)}$
    Set $\boldsymbol{x}^{(j)} = \boldsymbol{x}^{(j-1)}$, $\boldsymbol{r}^{(j)} = \boldsymbol{r}^{(j-1)}$
    for $i = 1, \cdots, j$ **do**
        $\boldsymbol{x}^{(j)} = \boldsymbol{x}^{(j)} + \alpha_i^{(j)}\boldsymbol{d}^{(i)}$
        $\boldsymbol{r}^{(j)} = \boldsymbol{r}^{(j)} + \alpha_i^{(j)}\boldsymbol{v}^{(i)}$
    end for
    Check convergence: if $\|\boldsymbol{r}^{(j)}\| < \varepsilon$ then stop.
    Compute $\boldsymbol{z}^{(j)} = P[\boldsymbol{r}^{(j)}]$
    Set $\boldsymbol{d}^{(j)} = -\boldsymbol{r}^{(j)}$
    for $i = 0, \cdots, j-1$ **do**
        Compute $\beta_i^{(j-1)} = \dfrac{(\boldsymbol{z}^{(j)}, \boldsymbol{d}^{(i)})_1}{(\boldsymbol{d}^{(i)}, \boldsymbol{d}^{(i)})_1}$ and $\boldsymbol{d}^{(j)} = \boldsymbol{d}^{(j)} + \beta_i^{(j-1)}\boldsymbol{d}^{(i)}$
    end for
end for

Algorithm FGMRES

We pose next the question how to incorporate a preconditioner, which changes during each iterations, thus, instead of P e have P_j for $j = 1, \cdots, k$. As derived in [7] the algorithm becomes

In Algorithm 5, $Z_k = [\boldsymbol{z}^{(1)}, \cdots, \boldsymbol{z}^{(k)}]$ and, as for GMRES, $\boldsymbol{e}_1 = [1, 0, \cdots, 0]$. Clearly, the only difference between the GMRES and FGMRES algorithms is that in the latter case we have to store the vectors $\boldsymbol{z}^{(*)}$.

The Generalized Conjugate Residual method

Algorithm GCR

The derivation of GCR is based on the assumption that we have a basis of the Krylov subspace with respect to the initial residual, which is A^TA-orthogonal. Thus,

$$(A\boldsymbol{g}^{(i)}, A\boldsymbol{g}^{(j)}) = 0 \text{ for } i \neq j.$$

As shown in [9], Lemma 6.2, the approximate solution $\boldsymbol{x}^{(k)}$ with the smallest norm in the space $\boldsymbol{x}^{(0)} + \mathcal{K}_k(A, \boldsymbol{r}^{(0)})$ can be expressed as

$$\boldsymbol{x}^{(k)} = \boldsymbol{x}^{(0)} + \sum_{i=1}^{k-1} \frac{(\boldsymbol{r}^{(0)}, A\boldsymbol{g}^{(i)})}{(A\boldsymbol{g}^{(i)}, A\boldsymbol{g}^{(i)})}\boldsymbol{g}^{(i)} = \boldsymbol{x}^{(m-1)} + \frac{(\boldsymbol{r}^{(m-1)}, A\boldsymbol{g}^{(m-1)})}{(A\boldsymbol{g}^{(m-1)}, A\boldsymbol{g}^{(m-1)})}\boldsymbol{g}^{(m-1)}.$$

The GCR is one of the methods, mathematically equivalent to the full GMRES, that are derived from this framework computing the next basis vector $\boldsymbol{g}^{(k+1)}$ as a linear combination of the current residual $\boldsymbol{r}^{(k)}$ and all previous $\boldsymbol{g}^{(i)}$. This leads to the following algorithm.

Algorithm 4 The preconditioned GMRES algorithm

1: Choose a maximum number of iterations k, define a matrix $\widetilde{H}_k = \{h_{i,j}\}$ of size $k+1 \times k$ and set it to zero. Let P be a preconditioner.
2: Given $\boldsymbol{x}^{(0)}$, compute $\boldsymbol{r}^{(0)} = \boldsymbol{b} - A\boldsymbol{x}^{(0)}$, $\beta = \|\boldsymbol{r}^{(0)}\|_2$, $\boldsymbol{v}_1 = \boldsymbol{r}^{(0)}/\beta$.
3: **for** $j = 1, \cdots, k$ **do**
4: Compute $\boldsymbol{z}^{(j)} = P^{-1}\boldsymbol{v}^{(j)}$
5: Compute $\boldsymbol{w} = A\boldsymbol{z}^{(j)}$
6: **for** $i = 1, \cdots, j$ **do**
7: $h_{ij} = (\boldsymbol{w}, \boldsymbol{v}^{(i)})$
8: $\boldsymbol{w} = \boldsymbol{w} - h_{ji}\boldsymbol{v}^{(i)}$
9: **end for**
10: $h_{j+1,j} = \|\boldsymbol{w}\|_2$. If $h_{j+1,j} = 0$, set $k = j$ and goto 13
11: $\boldsymbol{v}^{(j+1)} = \boldsymbol{w}/h_{j+1,j}$
12: **end for**
13: Compute $y^{(k)}$ as the minimizer of $\|\beta\boldsymbol{e}_1 + \widetilde{H}_k\boldsymbol{y}\|_2$ and $\boldsymbol{x}^{(k)} = \boldsymbol{x}^{(0)} + P^{-1}V_k\boldsymbol{y}^{(k)}$
14: If convergence is detected, stop. Otherwise set $\boldsymbol{x}^{(0)} = \boldsymbol{x}^{(k)}$ and go to 2.

Algorithm 5 The preconditioned FGMRES algorithm

1: Choose a maximum number of iterations k, define a matrix $\widetilde{H}_k = \{h_{i,j}\}$ of size $k+1 \times k$ and set it to zero.
2: Given $\boldsymbol{x}^{(0)}$, compute $\boldsymbol{r}^{(0)} = \boldsymbol{b} - A\boldsymbol{x}^{(0)}$, $\beta = \|\boldsymbol{r}^{(0)}\|_2$, $\boldsymbol{v}_1 = \boldsymbol{r}^{(0)}/\beta$.
3: **for** $j = 1, \cdots, k$ **do**
4: Compute $\boldsymbol{z}^{(j)} = P_j^{-1}\boldsymbol{v}^{(j)}$
5: Compute $\boldsymbol{w} = A\boldsymbol{z}^{(j)}$
6: **for** $i = 1, \cdots, j$ **do**
7: $h_{ij} = (\boldsymbol{w}, \boldsymbol{v}^{(i)})$
8: $\boldsymbol{w} = \boldsymbol{w} - h_{ji}\boldsymbol{v}^{(i)}$
9: **end for**
10: $h_{j+1,j} = \|\boldsymbol{w}\|_2$. If $h_{j+1,j} = 0$, set $k = j$ and goto 13
11: $\boldsymbol{v}^{(j+1)} = \boldsymbol{w}/h_{j+1,j}$
12: **end for**
13: Compute $y^{(k)}$ as the minimizer of $\|\beta\boldsymbol{e}_1 + \widetilde{H}_k\boldsymbol{y}\|_2$ and $\boldsymbol{x}^{(k)} = \boldsymbol{x}^{(0)} + Z_k\boldsymbol{y}^{(k)}$
14: If convergence is detected, stop. Otherwise set $\boldsymbol{x}^{(0)} = \boldsymbol{x}^{(k)}$ and go to 2.

Algorithm 6 The preconditioned GCR algorithm

1: Given $\boldsymbol{x}^{(0)}$, compute $\boldsymbol{r}^{(0)} = \boldsymbol{b} - A\boldsymbol{x}^{(0)}$, $\boldsymbol{v}^{(0)} = \boldsymbol{r}^{(0)}$, $\boldsymbol{z}^{(0)} = P^{-1}[\boldsymbol{r}^{(0)}]$, $\boldsymbol{g}^{(0)} = A\boldsymbol{z}^{(0)}$.
2: **for** $j = 0, 1, \cdots$ until convergence **do**
3: $\alpha_j = \dfrac{(\boldsymbol{r}^{(k-1)}, \boldsymbol{g}^{(k)})}{(\boldsymbol{g}^{(k)}, \boldsymbol{g}^{(k)})}$
4: $\boldsymbol{x}^{(j+1)} = \boldsymbol{x}^{(j)} + \alpha_j\boldsymbol{z}^{(j)}$
5: $\boldsymbol{r}^{(j+1)} = \boldsymbol{r}^{(j)} - \alpha_j\boldsymbol{g}^{(j)}$
6: Compute $\boldsymbol{z}^{(j+1)} = P^{-1}[\boldsymbol{r}^{(j+1)}]$, $\boldsymbol{g}^{(j+1)} = A\boldsymbol{z}^{(j+1)}$
7: **for** $i = 0, \cdots, j-1$ **do**
8: $\beta_{j,i} = -\dfrac{(\boldsymbol{g}^{(j+1)}, \boldsymbol{z}^{(i)})}{(\boldsymbol{z}^{(i)}, \boldsymbol{z}^{(i)})}$, $\boldsymbol{v}^{(j+1)} = \boldsymbol{v}^{(j+1)} + \beta_{ji}\boldsymbol{v}^{(i)}$
9: **end for**
10: **end for**

We see that Algorithm 6 requires to store two sets of vectors - $\boldsymbol{g}^{(i)}$ and $A\boldsymbol{g}^{(i)}$.

In the presentation we discuss further the convergence of the methods and some variants (cf., e.g., [11–13]) as well as we present some numerical illustrations of their performance.

References

[1] O. Axelsson, A generalized conjugate gradient, least square method, *Numerische Mathematik*, 51 (1987), 209–227.

[2] O. Axelsson, Conjugate gradient type methods for unsymmetric and inconsistent systems of linear equations, RR.78.03R, Department of Computer Sciences, Chalmers University of Technology, G oteborg, Sweden 1978.

[3] O. Axelsson, Conjugate gradient type methods for unsymmetric and inconsistent systems of linear equations. *Linear Algebra and Its Applications* 29 (1980), 1–16.

[4] O. Axelsson, P. Vassilevski, A black box Generalized Conjugate Gradient solver with inner iterations and variable-step preconditioning, *SIAM Journal on Matrix Analysis and Applications*, 12 (1991), 625–644.

[5] O. Axelsson, A restarted version of a generalized preconditioned conjugate gradient method, *Comm. Appl. Numer. Meth.*, 4 (1988), 521–530.

[6] Yousef Saad, Martin H. Schultz, GMRES: A Generalized Minimal Residual Algorithm for Solving Nonsymmetric Linear Systems, *SIAM Journal on Scientific and Statistical Computing*, 7 (1986), 856–869.

[7] Yousef Saad, A Flexible Inner-Outer Preconditioned GMRES Algorithm, *SIAM Journal on Scientific Computing*, 14 (1993), 461–469.

[8] S.C. Eisenstat, H.C. Elman, M.H. Schultz. Variational iterative methods for non- symmetric systems of linear equations, *SIAM Journal on Numerical Analysis*, 20 (1983), 345–357.

[9] Yousef Saad, *Iterative methods for sparse linear systems*, International Thomson Publishing Inc. 1996.

[10] O. Axelsson, *Iterative Solution Methods*, Cambridge University Press, 1994.

[11] V. Simoncini, D. Szyld, Flexible Inner-Outer Krylov Subspace Methods, *SIAM Journal on Numerical Analysis*, 40 (2002), 2219–2239.

[12] Kuniyoshi Abe, Shao-Liang Zhang, A variable preconditioning using the SOR method for GCR-like methods, *International Journal of Numerical Analysis and Modeling*, 2 (2005), 147–161.

[13] Z. B, D. Hu, L. Reichel, A Newton basis GMRES implementation, *IMA Journal of Numerical Analysis*, 14 (1994), 563–581.

* * *

Variance-based Sensitivity Analysis of an Air Pollution Model

T. Ostromsky, R. Georgieva, V. Todorov, S.-M. Gurova, I. Dimov

Abstract

Sensitivity analysis is a technique that studies how various sources of uncertainty in a mathematical model contribute to the model's overall uncertainty. It is a powerful tool for studying and improving the reliability of mathematical models that are high-dimensional and labor-intensive. Air pollution and meteorological models are examples of such difficult-to-solve mathematical problems. They are characterized by uncertainty in the input data sets and parameters. Here, we present some results from our global sensitivity study of the Unified Danish Euler Model (UNIDEM). One favorable feature of UNI-DEM is its advanced chemical scheme – Condensed CBM IV, which deals in detail with a lot of chemical species and numerous reactions between them. Ozone is known to be one of the most dangerous pollutants. The sensitivity of UNI-DEM outputs for ozone concentration to variations of some chemical reaction rate coefficients is investigated in this short communication.

Three different stochastic algorithms (Crude Monte Carlo, Fibonacci Lattice rule, and a new Lattice Sequence algorithm using CBC [1]) for construction of the generating vector were used in this study. The numerical experiments were carried out on the Bulgarian supercomputer Discoverer. They show that the studied stochastic algorithms are quite efficient for this purpose, especially for estimating the contribution of small-valued sensitivity indices.

1 Introducton

Among quantitative sensitivity analysis methods, variation-based methods are the most commonly used [1]. Their main idea is to estimate how the variance of an input or group of inputs contributes to the variance of the output. In the case of correlated model inputs, some other approaches must be used to calculate not only variance-based sensitivity measures but also some other sensitivity measures. In this case, non-parametric methods [2] and density-based methods [3] can be applied.

Variation-based methods calculate global, quantitative and model-independent measures of sensitivity. In [4], a general concept of sensitivity is used, namely a variance-based sensitivity analysis using the Monte Carlo technique. Monte Carlo methods require a large number of simulations. Uncertain input parameters are modeled by random variables and characterized by their probability density functions. The analysis is focused on the following question: *Which of the deviations of the input variables most affect the output of the model and should be estimated more precisely to improve output accuracy?*

A systematic approach to sensitivity analysis studies in the field of air pollution modeling is presented. The target model studied is the unified Danish Euler model (UNI-DEM) [5]. Various parts of the large amount of output data produced by the model have been used in various practical applications where the reliability of these data must be properly assessed. In his complex chemical scheme, where all relevant chemical processes in the atmosphere are represented, there are some experimentally determined parameters. It is necessary to know which ones are critical for certain output values to evaluate them more accurately.

2 UNI-DEM and its SA version – SA-DEM

2.1 Description and implementation of UNI-DEM

The Unified Danish Eulerian Model (UNI-DEM) is a large numerical model used for air pollution studies and simulations in Europe. It is designed to simulate the behavior of a large number of air pollutants, such as gases and aerosols, in the atmosphere and their long-range transport. UNI-DEM integrates various physical and chemical processes, including emissions, chemical reactions, advection, diffusion, and deposition. The model is based on the Eulerian framework, which divides the atmosphere into grid cells and tracks the movement and transformation of pollutants within these cells over time. UNI-DEM is widely used in air quality research and environmental assessments. It helps to understand the sources, distribution, and impacts of air pollutants on local, regional, and global scales [5].

Formally, UNI-DEM is represented by a complex system of partial differential equations (PDE), from which the unknown concentrations of the air pollutants can be calculated. For efficient numerical treatment, the system is split into 3 submodels across the major physical and chemical processes. Spatial and time discretization makes each of the submodels a tough computational task, even for the most advanced supercomputer systems. Efficient parallelization has always been a crucial point in the computer implementation of UNI-DEM. The task became much more challenging with the development of the sensitivity analysis version of the code–SA-DEM [6].

[1] Component by Component Fast Construction method

2.2 Scalability and efficiency of SA-DEM

This section shows scalability results of SA-DEM for a series of experiments performed on the supercomputer Discoverer [7,8] with the high-resolution two-dimensional grid version (see Table 1).

Table 1: Scalability of SA-DEM on the Discoverer

Time T [sec.] , **speed-up *Sp*** and total **efficiency E [%]**
of SA-DEM on Discoverer $(480 \times 480 \times 1)$ grid

NP		Advection		Chemistry		TOTAL		
(MPI)	nodes	T [sec.]	*Sp*	T [sec.]	*Sp*	T [sec.]	*Sp*	E [%]
10	1	72142	*10.0*	64726	*10.0*	146335	*10*	100
20	2	36175	*19.9*	30027	*21.6*	71129	*21*	103
40	3	18297	*39.4*	14295	*45.3*	36619	*40*	100
80	5	9523	*75.8*	7839	*82.6*	20383	*72*	90
160	10	4781	*151*	3925	*164*	11769	*124*	78
320	20	2525	*286*	2037	*317*	6861	*213*	67
640	40	1332	*542*	1034	*626*	4852	*302*	47
960	60	1017	*710*	697	*929*	3472	*421*	44
1600	100	787	*917*	463	*1398*	2822	*519*	32

It is seen from Table 1 that the chemical stage (the most computationally expensive) scales very well (shows almost linear speed-up in the whole range of experiments). The advection stage scales pretty well in most of the experiments, with an understandable slow-down in the highly parallel experiments. It is caused by the significant boundary overlapping of the domain partitioning when approaching the inherent partitioning limitations. In general, SA-DEM performs quite efficiently and shows relatively high scalability on such a large supercomputing system.

3 Improved Lattice Sequence approach for SA

We shall use the rank-1 lattice sequence (LS) defined by [9]: $\mathbf{x}_k = \left\{ \frac{k}{N}\mathbf{z} \right\},\ k = 1, \ldots, N$, where $N \geq 2$ is an integer, $\mathbf{z} = (z_1, z_2, \ldots z_s)$ is the generating vector (GV). More about the widely used Fibonacci method FIBO can be found in [9]. Now we develop a new method LS, by using GV obtained by the Component by Component Fast Construction method (CBC) [10] with CBC construction of rank-1 lattice rule with prime number of points and with product weights.

The present analysis of sensitivity relies on representing the model function through ANOVA and employing the Sobol' method, which utilizes sensitivity measures (known as sensitivity indices) determined by partial and total variances [11]. Consequently, the primary mathematical challenge lies in approximating Sobol' sensitivity indices, which involve integrals of multiple dimensions defined by the terms involved. We use $g_d(\mathbf{x}), d = 1, \ldots$ from the model function $f(\mathbf{x}),\ \mathbf{x} \in \mathbb{U}^n$ decomposition: $I^d = \int_{\mathbb{U}^d} g_d(\mathbf{x}) \mathrm{d}\mathbf{x},\ d = 1, \ldots$. One should notice that $f_0 = \int_{\mathbb{U}^n} f(\mathbf{x}) \mathrm{d}\mathbf{x}$. Finally, the approximate value I_N^d of the corresponding integral is obtained by the following MC estimate: $I_N^d = \frac{1}{N} \sum_{k=1}^{N} F\left(\left\{ \frac{k}{N}\mathbf{z} \right\} \right)$, where F is g_d or f and N is the number of samples.

4 Sensitivity of UNI-DEM with respect to some chemical reaction rate coefficients

Among UNI-DEM's many large output datasets are monthly mean concentrations of 35 pollutants or groups of pollutants. For this study, one of them, *ozone* (O_3), was chosen because it is dangerous to human health. Of the more than 70 chemical reactions in the condensed CBM-IV scheme ([5]), six were found to be important for UNI-DEM ozone output results during our previous studies. The results (specifically the relative errors) related to the sensitivity studies concerning the rates of these 6 chemical reaction rate coefficients are presented in Table 2.

Table 2: Relative error for estimation of sensitivity indices of 6 chemical rate coefficients, calculated by using various stochastic approaches ($N \approx 2^{20}$).

Index	Ref. value	**CRU**	**LS**	**FIBO**
S_1	4 **e**-01	2.5e-03	5.5e-05	9.2e-03
S_2	3 **e**-01	1.9e-02	3.6e-04	1.4e-02
S_3	5 **e**-02	3.5e-03	5.4e-04	6.5e-01
S_4	3 **e**-01	1.7e-02	2.1e-03	1.5e-01
S_5	4 **e**-07	1.9e+02	2.4e+02	2.7e+03
S_6	2 **e**-02	5.4e-02	1.8e-04	1.1e+00
S_1^{tot}	4 **e**-01	7.9e-03	8.4e-04	9.7e-03
S_2^{tot}	3 **e**-01	1.9e-02	7.8e-04	3.0e-02
S_3^{tot}	5 **e**-02	3.1e-03	5.4e-03	1.4e+00
S_4^{tot}	3 **e**-01	2.0e-02	1.7e-03	3.7e-01
S_5^{tot}	2 **e**-04	5.8e-01	1.5e-01	3.9e+01
S_6^{tot}	2 **e**-02	7.2e-02	6.1e-04	1.8e+00
S_{12}	6 **e**-03	1.3e-01	6.0e-02	8.4e-02
S_{14}	5 **e**-03	2.7e-01	4.0e-03	1.8e-01
S_{24}	3 **e**-03	3.0e-01	2.3e-02	1.4e+01
S_{45}	1 **e**-05	3.1e+00	1.4e-01	2.6e+01

From the numerical data presented, it can be concluded that the new version of the LS algorithm significantly outperforms the standard Fibonacci (FIBO) and traditional (Crude) Monte Carlo (CRU) algorithms. Furthermore, LS performs significantly better in evaluation of small value indices. In case of extremely small values, however, none of the algorithms give reliable results (for example, S_5).

Acknowledgements

This work is supported in parts by the Bulgarian NSF project "Efficient methods for modelling, optimization and decision making" (Grant No. KP-06-N52/5 , 2021) and by the Petascale-Bulgaria supercomputer consortium and EuroHPC JU. The work of Tzvetan Ostromsky was supported in the framework of the National Science Program "Environmental Protection and Reduction of Risks of Adverse Events and Natural Disasters", approved by the Resolution of the Council of Ministers No.577/17.08.2018 and by the Ministry of Education and Science (MES) of Bulgaria (D01-271/09.12.2022). The work of Silvi-Maria Gurova was carried out using the infrastructure purchased under the National Roadmap for RI, financially coordinated by the MES of the Republic of Bulgaria (Grant No. DO1-325/01.12.2023) and supported also by Grant No 30 from CAF America.

References

[1] Saltelli, A., Chan, K., Scott, M.: *Sensitivity Analysis.* John Wiley & Sons publishers, Probability and Statistics series (2000)

[2] Helton, J.C., Uncertainty and sensitivity analyses techniques for use in performance assessment for radioactive waste disposal, *Reliability Engineering & System Safety*, **42**, pp. 327-367, (1993)

[3] Borgonovo, E.: A new uncertainty importance measure, *Reliability Engineering & System Safety*, **92** (6), 771-784, (2007)
[4] Dimov, I.T., Zlatev, Z.: Testing the sensitivity of air pollution levels to variations of some chemical rate constants, *Notes on Numerical Fluid Mechanics*, **62**, pp. 167-175, (1997)
[5] Zlatev, Z., Dimov, I. T., Computational and Numerical Challenges in Environmental Modelling, Elsevier, (2006)
[6] Ostromsky Tz., Dimov I.T., Georgieva R., Zlatev Z., Air pollution modelling, sensitivity analysis and parallel implementation, Int. Journal of Environment and Pollution, **46** (1/2), pp. 83-96, (2011)
[7] The official web page of the supercomputer Discoverer: https://sofiatech.bg/en/petascale-supercomputer (Last accessed January 2024)
[8] Discoverer HPC Doc: https://docs.discoverer.bg/index.html (Last accessed January 2024)
[9], Y., Hickernell, F.J., An historical overview of lattice point sets. In: Monte Carlo and Quasi-Monte Carlo Methods 2000, Proc. Conf. held at Hong Kong Baptist Univ., China (2000)
[10] Baldeaux, J., Dick, J., Leobacher, G., Nuyens, D., Pillichshammer, F.: Efficient calculation of the worst-case error and (fast) component-by-component construction of higher order polynomial lattice rules, *Numer. Algor.* **59**, pp. 403-431, (2012)
[11] Sobol, I.M., Sensitivity estimates for nonlinear mathematical models, *Mathematical Modeling and Computational Experiment*, **1** (4), pp. 407-414, (1993)

* * *

Impact of the Mutations in the Spike-Protein Binding Domain of SARS-CoV-2 Virus: A Computational Study of RBM Peptides of the Wuhan, Alpha, Beta/Gamma, and Zeta Variants

P. Petkov, E. Lilkova, N. Ilieva, D. Witkowska, A. Rombel-Bryzek, L. Litov

The SARS-CoV-2 Spike protein (S) is the key actor of the viral invasion into the host cells. Structurally, the S protein is a trimeric glycoprotein protruding from the virus surface. Each monomer of the S protein is composed of two main subunits, S1 and S2, which have distinct roles in the virus entry process.

The S1 subunit contains the Receptor Binding Domain (RBD), which is critical for the virus' recognition and binding to the host cell receptor. Within the RBD, there is a specific segment known as the Receptor Binding Motif (RBM). The RBM directly interacts with the angiotensin-converting enzyme 2 (ACE2) receptor on the surface of human cells. This interaction is the first step in the process of viral entry into the host cell.

Table 1: The four investigated RBM subsequences.

Wuhan (WT)	...	^{482}GVEGFNCYFPLQSYGFQPTNG^{502}	...
Alpha	...	^{482}GVEGFNCYFPLQSYGFQPTYG^{502}	...
Beta/Gamma	...	^{482}GVKGFNCYFPLQSYGFQPTYG^{502}	...
Zeta	...	^{482}GVKGFNCYFPLQSYGFQPTNG^{502}	...

The RBM's molecular interactions with the ACE2 receptor are highly specific, involving a series of key residues that form hydrogen bonds, salt bridges, and van der Waals contacts. This specificity is crucial for the SARS-CoV-2 ability to bind to human cells effectively. Therefore, it is a major focus of the research on the virus' infectivity, but also in the development of vaccines and therapeutic agents against it. Since the appearance of omicron, the strength of the RBD binding of the virus to the human

ACE2 receptor is not closely related to its virulence and ability to spread, but understanding the impact of specific mutations within this domain on the binding remains an indispensable element in the drug design.

Here, we present a computational study of the binding of several peptide analogues of RBM of the wild-type (WT) and three variants of SARS-CoV-2 (Table 1) to a model of the glycosylated human ACE2 receptor (Fig. 1). We aim to provide molecular basis for the experimentally observed variations in the enthalpic and entropic contributions to the binding free energy of the four peptides. We demonstrate that the measured thermodynamic properties of the binding can be traced back to different H-bonding patterns and forming of hydrophobic contacts.

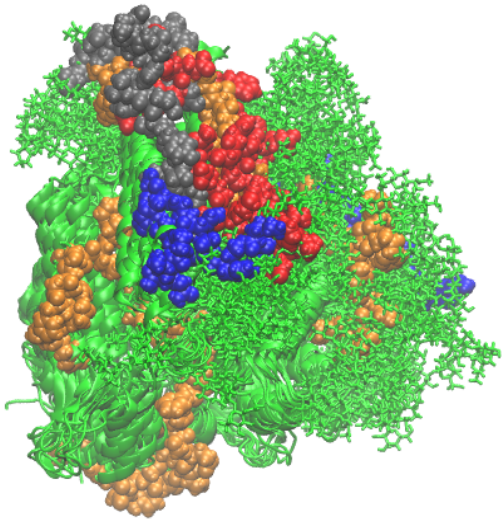

Figure 1: Binding of the RBM peptides of the WT (gray), alpha (red), beta (orange) and zeta (blue) variants of SARS-CoV-2 to the glycosylated hACE2 protein (green).

Acknowledgments

We acknowledge the inspiring discussions within the DYNALIFE COST Action, CA21169, supported by the European Cooperation in Science and Technology (COST). This work was supported in part by the Bulgarian National Science Fund (grant KP-06-COST-20/2023) and by the Polish National Science Centre (grant UMO-2020/37/B/ NZ6/01476).

Computaional resources were provided by the BioSim HPC cluster at the Faculty of Physics, Sofia University "St. Kliment Ohridski", the Centre for Advanced Computing and Data Processing, supported under Grant BG05M2OP001-1.001-0003 by the Science and Education for Smart Growth Operational Program (2014–2020) and co-financed by the European Union through the European structural and in-vestment funds, as well as by the DEEP system, operated at the Jülich Supercomputing Centre and built as part of the DEEP project series, which received funding from the European Commission's FP7 or H2020 Programmes, under Grant Agreements No 287530, 610476, and 754304.

* * *

Numerical Simulations Based on Micro–CT Data Visualization in Dentistry

M. Raykovska, M. Tsvetkov, I. Georgiev, R. Iankov

In dentistry, the integration of micro-CT data visualization and numerical simulation has opened up new avenues of research. This interdisciplinary approach combines advanced imaging technology with computational analysis, enabling a deeper understanding of the complex structures in the oral cavity.

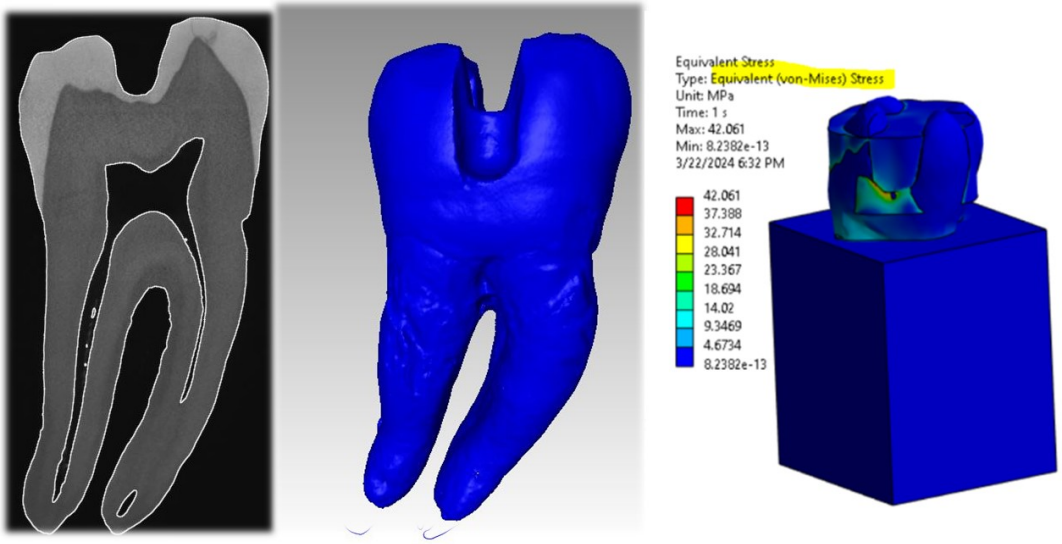

Figure 1: Micro-CT and STL images and the result from the numerical simulation - equivalent (von Mises) stress distribution.

Micro-CT scans provide high-resolution, three-dimensional representations of dental anatomy. These images can be transformed into simulations, which allow dental experts to explore different phenomena digitally. The tooth is composed of different parts, including dentin, enamel, cementum, and dental pulp. Dentin is a mineralized tissue and the primary part of the tooth structure. Enamel is a protective layer covering the dentin on the tooth's crown. A cementum layer on the root helps anchor the tooth to the bone. The dental pulp is a soft tissue containing nerves and blood vessels inside the tooth. The pulp connects to the periodontal ligament and the bone socket. Dentin is a tubular-porous structure with a mineral composition of 70%, an organic matrix of 20%, and a water content of 10%. The organic matrix is predominantly represented by collagen fibers, which make dentin exceptionally resistant to loads. This is why dentin is of interest in studies involving finite elements.

Numerical simulation is a valuable technique that enables researchers to predict the mechanical behavior and stress distribution of dental structures under various loading conditions. Finite element analysis and computational modeling are used to study how dental prostheses and restorative materials interact with the body. These tools aid in designing and evaluating materials more effectively. By utilizing these techniques, researchers can better understand complex biomechanical interactions.

The integration of numerical simulation and micro-CT data visualization represents a transformative approach to dental science, offering unprecedented insights into the complex dynamics of the oral environment. This process significantly streamlines and accelerates the analysis of various materials and cavity forms, saving time and resources, and enabling the selection of models for further research.

Acknowledgements
The author would like to express gratitude for the financial support of the Bulgarian National Science Fund, grant KP-06-H27/6.

* * *

Adaptive Explicit-Implicit Solver for Parabolic Fractional Diffusion Problems

D. Slavchev, S. Margenov

1 Introduction

The Fractional Laplace operator is used to model *anomalous* diffusion problems. Such problems arise in many research fields, for example in diffusion within cells, porous materials, ion channels in the plasma membrane, atmospheric processes and others. The Fractional Laplace operator is *non-local* and solving practical problems involving it is a computationally complex task. Using the finite element method for the discretization in space leads to a dense stiffness matrix K. Solving elliptic or parabolic problems with K leads to systems of linear algebraic equations. In the general case solving one such system with LU factorization has computational complexity $O(N^3)$, where N is the amount of nodal unknowns introduced by the triangulation.

In this work we examine a parabolic fractional in space problem. For the discretization in space we use the finite element method and for the discretization in time we employ an adaptive explicit-implicit Euler scheme. First we calculate the solution obtained by increasing the time step size and calculating a prognostic solution with explicit Euler and then we use it to gauge the error of the method. This error is then used to determine the size of the next time step to be used by the implicit Euler method. With this method the computational complexity is $O(N^3 m_{\text{adaptive}})$, where m_{adaptive} is the number of time steps. We will then compare thus described method with an explicit Euler scheme with uniform time steps. The Euler scheme with uniform time steps has computational complexity $O(N^3 + N^2 m_{\text{uniform}})$, where m_{uniform} is the number of steps. For the model problem we introduce large jumps in the right hand side, which require relatively small time steps to calculate an accurate solution.

2 Parabolic Fractional Diffusion problem

For our numerical experiments we use the following fractional parabolic problem

$$\left|\begin{array}{rcll} \dfrac{\partial u(x,t)}{\partial t} + (-\Delta)^{\alpha} u(x,t) &=& f(x,t), & x \in \Omega, \quad t \in [0,T] \\ u(x,t) &=& 0, & x \in \Omega^c, \quad t \in [0,T] \\ u(x,0) &=& u^0(x), & x \in \Omega. \end{array}\right.$$

Here $u(x,t)$, $x \in \Omega$, $t \in [0,T]$ is the unknown quantity defined within the space domain Ω and the time interval, Ω^c is the complement of Ω, $(-\Delta)^{\alpha}$ is the Fractional Laplace operator on power α. We should note that we are examining the 2 dimensional problem.

After applying finite elements to the space domain with suitable triangulation as described in [1] and discretization in time with implicit Euler scheme the problem can be written in the following form

$$M_L \frac{\mathbf{u}^{j+1} - \mathbf{u}^j}{\tau_j} + K\mathbf{u}^{j+1} = M_L \frac{\mathbf{f}^{j+1} + \mathbf{f}^j}{2}, \quad j = 0, \ldots, m-1, \tag{1}$$

where $\mathbf{u}^j$ is the solution at the current time and $\mathbf{u}^{j+1}$ is the unknown solution at the next time step, τ_j is the current time step, m is the number of time steps, M_L is the lumped mass matrix and K is the stiffness matrix. At each time step the problem is reduced to solving the following system of linear algebraic equations

$$\left(\frac{M_L}{\tau_j} + K\right)\mathbf{u}^{j+1} = M_L \frac{\mathbf{f}^{j+1} + \mathbf{f}^j}{2} + \frac{\mathbf{u}^j}{\tau_j}. \tag{2}$$

When using an uniform time stepping scheme $\tau_j = \tau, j = 0, \ldots, m-1$ the matrix $(K + M_L/\tau)$ is the same for all time steps. This allows us to factorize the matrix only once with computational complexity $O(N^3)$ and at each time step to solve with the factorized matrix with computational complexity for the whole time period $O(N^2 m)$. One disadvantage of the described method is that if there are large jumps in the values of the right hand side in time it would require a very small time step τ and a large total amount of steps m. One way to get around this problem is to use an adaptive scheme that adapts the time step to the truncation error on the fly.

3 Adaptive forward-backward Euler scheme

For the adaptive evaluation of time step size we use the method described by Vabishchevich in [2]. The following estimate can be made for the error $z_n = y_j - u_j$ (here y_j is the approximate solution, u_j is the exact solution)

$$\frac{z_{j+1} - z_n}{\tau_j + 1} + (-\Delta)^\alpha z_{n+1} = \frac{f_{j+1} + f_j}{2} - \frac{u^{j+1} - u^j}{\tau_{n+1}} - Ku^{j+1} = \Psi_{j+1}.$$

Here Ψ_j is the truncation error. We can estimate the error as

$$||z_j + 1|| \leq \sum_{k=0}^{n} \tau_j \|\Psi_{j+1}\| \tag{3}$$

The summarized error $\tau_{j+1}\delta$ over the $t_j \leq t \leq t_{j+1}$ interval c an be used for error control. Here δ is the prescribed level of error. Following (3) the approximate solution accumulates with time and satisfies the estimate

$$||z_{j+1}|| \leq \delta t_{j+1}.$$

The algorithm developed in [2] uses three steps to correct the time step τ_{j+1}:

1. *Prognostic solution.* The prognostic solution $\tilde{y}_{j+1}$ is calculated at time $\tilde{t}_{j+1} = t_j + \tilde{\tau}_{j+1}$. The prognostic step is always increased in comparison to the previous step $\tilde{\tau}_{j+1} = \gamma\tau_j$, we are using $\gamma = 1.5$ in the numerical experiments. The prognostic solution is then calculated with a single step explicit Euler scheme
$$\frac{\tilde{y}_{j+1} - y_j}{\tau_{\tilde{j+1}}} + (-\Delta)^\alpha y_j = f_j.$$

2. *Truncation error.* The implicit scheme and the prognostic solution are used to determine the truncation error at the prognostic step in the following way

$$\tilde{\Psi}_{j+1} = \tilde{f}_{j+1} - \frac{\tilde{y}_{j+1} - y_j}{\tilde{\tau}_{j+1}} + (-\Delta)^\alpha \tilde{y}_{j+1}, \quad \tilde{f}_{j+1} = f(x, t_n + \gamma\tilde{\tau}_j).$$

3. *Step Selection.* The next step $\tau_{j+1} = \gamma_{j+1}\tau_j$ is calculated using the error norm and δ with the following formula

$$\gamma_{j+1} = \frac{\delta}{\left\| \tilde{f}_{j+1} - f_j - (-\delta)^\alpha (\tilde{y}_{j+1} - y_j) \right\|} \gamma.$$

The solution at $t_{j+1} = t_j + \tau_{j+1}$ is then calculated with an implicit Euler scheme as described in (1). The overall computational complexity of the method is dominated by the solution of the dense system of linear algebraic equations (2). The overall computational complexity of the method when using LU factorization for the solution is $O(N^3 + m_{\text{adaptive}} N_2)$. Here m_{adaptive} is the number of steps with the adaptive explicit-implicit algorithm.

4 Numerical experiments

For the numerical experiments we use the following settings in $t = [0, 0.1]$

$$f(x,t) = \begin{cases} 100\bar{f}(x), & t \in (0, \widetilde{\tau}_1) \\ 200\bar{f}(x), & t \in (\widetilde{\tau}_2, \widetilde{\tau}_3) \\ 0, & otherwise \end{cases}, \text{ where } \bar{f}(x) = \begin{cases} 1 & x_1 x_2 > 0, x \in \Omega \\ -1 & x_1 x_2 \leq 0, x \in \Omega. \\ 0 & x \notin \Omega \end{cases}$$

Here $\widetilde{\tau}_1 = 0.01$, $\widetilde{\tau}_2 = 0.05$ and $\widetilde{\tau}_3 = 0.06$. The right hand side of the problem includes large jumps and in order to obtain reasonable accuracy a very small step is required near those points of interest. With the uniform time stepping scheme this results in large amounts of steps needed. With the adaptive method the step is naturally shrinked when such jumps are present and then increased in the rest of the interval.

Our study includes determining the size of steps needed to achieve a certain accuracy level. This is achieved by calculating the relative errors between solutions calculated with decreaasing step sizes with the uniform method. We then analyze the computational times of the adaptive method with the thus determined initial step size. We also study the parallel efficiency and speed up of the methods on the supercomputer AVITOHOL.

Acknowledgements

The authors are supported by the Bulgarian NSF with grant number KP-06 N72/2.

We acknowledge the provided access to the e-infrastructure of the NCHDC – part of the Bulgarian National Roadmap on RIs, with the financial support by the Grant No D01-325/01.12.2023.

References

[1] G. Acosta and J.P. Borthagaray. A Fractional Laplace Equation: Regularity of Solutions and Finite Element Approximations. In *SIAM Journal on Numerical Analysis*, volume 55, pages 472–495, 2017.

[2] P. N. Vabishchevich and A. O. Vasil'ev. Time step selection for the numerical solution of boundary value problems for parabolic equations. *Computational Mathematics and Mathematical Physics*, 57(5):843–853, May 2017.

* * *

Application of AI in Digital Marketing

J. Stanchov

1 Introduction

Artificial intelligence is changing the world today. You likely use it many times a day without even realizing it. When you want to figure out how to make protein pancakes, you can search the web with Google, Bing, or Baidu to find out. And it works so well because it is machine learning software that has figured out how to rank web pages. Or when you upload photos to Instagram or Snapchat and think, "I want to tag my friends so they can see their photos well." Every time you say to your phone, "Hey Siri, play me a Rihanna song," that is also an application of artificial intelligence. Artificial intelligence finds wide application in big companies, industrial applications, and society. For example: I am deeply concerned about climate change and I am happy to see how AI optimizes the generation of energy from wind turbines; or in healthcare - artificial intelligence enters hospitals to help doctors make accurate diagnoses. This scientific article explores the application of Artificial Intelligence (AI) in the field of Digital Marketing. The research covers various aspects of AI technology and how they are utilized to enhance the effectiveness of marketing strategies and campaigns.

2 Classification of AI Based on Different Types of Technologies

Classifying AI into weak and strong categories is too restrictive. A classification approach based on different types of technologies appears more appropriate, providing a more comprehensive overview of the diversity of methods and techniques used in the development of artificial intelligence. This classification includes visual recognition, speech recognition, natural language processing (NLP), expert systems, efficient computations, and artificial intelligent robots [1].

Visual recognition - Thanks to new image recognition technologies, we now have specific software and applications that can interpret visual information.

Natural Language Processing (NLP) is a part of AI that involves analyzing natural language data and converting it into a machine-readable format. Speech recognition and AI play an integral role in NLP models to improve the accuracy and efficiency of human language recognition for intelligent home devices and appliances that accept instructions and can be remotely turned on and off.

Expert systems - a computer program designed to solve complex problems and provide decision-making capabilities like a human expert. It does this by extracting knowledge from its knowledge base, using reasoning rules, and making inferences based on user requests. The system aids in decision-making for complex problems by using both facts and heuristics. These systems are designed for specific domains - medicine, science, etc.

Affective Computing, also known as Emotion AI, automatically recognizes emotions. Affective Computing is a state of the system that can recognize, interpret, process, and simulate human feelings and emotions.

Artificial intelligent robots - Robotics is a branch of engineering and computer science where machines are created to perform programmed tasks without further human intervention.

3 The Role and Function of Artificial Intelligence

A multitude of methods provide opportunities for solving a wide range of challenging problems in business and society. The main functions of artificial intelligence (AI), which facilitate such effective

implementation, are focused on four main directions: The first function reflects the unique capabilities of AI in machine learning. We will focus on neural networks, deep learning, support vector machines, and k-nearest neighbor methods. Another functional direction focuses on the unique capabilities of AI in prediction. It includes forecasting and training causal relationships through Bayesian learning (Naive Bayes Classifier), decision forests (Random Forest), model ensembles like XGBoost, and, most importantly, predicting critical business parameters. The importance of the third main function of AI - the ability to reason and provide automated solutions to complex problems - is increasingly growing. This function is based on fuzzy logic methods, expert systems, knowledge graphs, and cognitive models. There is also an extensive area for problem-solving where AI can assist us with several algorithms, including genetic algorithms, heuristic algorithms, optimization with ant colonies (Ant Colony Optimizatons - ACO), optimization through simulation of bird flocking (Particle Swarm Optimization - PSO).

4 How Artificial Intelligence Is Transforming Digital Marketing?

AI is at the core of social platforms such as Twitter, Facebook, Snapchat, etc. AI algorithms suggest to users to follow and share news based on individual user preferences, for tracking and categorizing video content based on subjects, recognizing hate speech and terrorist language, etc. In addition, AI is widely used on online shopping and e-commerce platforms as well as on online content streaming platforms where content and products that might interest the user are suggested based on previous experiences (recommendation) [2].

4.1 New User Experience

Most users engage in both webrooming and showrooming when shopping for various products. This hybrid user journey requires the use of an omnichannel approach to user experience, high-tech but also high-touch service. New approaches to interacting with a product are now more exciting than the product itself. Here are some new approaches to product interaction: Virtual and Augmented Reality (VR and AR); Voice Interfaces; Internet of Things (IoT).

These new approaches to product interaction provide users with more convenient, personalized, and immersive experiences, which can improve their satisfaction and connection with the brand.

4.2 Content Personalization with Artificial Intelligence

Content marketing has become a modern phrase and is used as an alternative to advertising. Content is not as intrusive as advertising. It attracts attention without being aggressive, simultaneously entertaining, educating, and inspiring users. Content personalization with AI can enhance user engagement, increase the effectiveness of marketing campaigns, and provide a better user experience. Content personalization involves various aspects and approaches that can be implemented using artificial intelligence. Some of these aspects include: analyzing user behavior, searches, and interests; personalized recommendations; dynamically generating content; adaptive design; and interface building. The use of artificial intelligence for content personalization can be accomplished through various tools and platforms like: Content Management Systems (CMS); Customer Relationship Management (CRM). These tools and platforms are just some of the possibilities for content personalization using artificial intelligence and can be combined and adapted depending on the needs and goals of specific marketing projects.

4.3 Data-Driven Marketing

Target creates an algorithm that predicts the likelihood of a woman shopping in the store being pregnant based on the products she has purchased. The market is diverse, and every customer is unique. That is why marketing always starts with segmentation and targeting. Companies can develop strategies and tactics based on an understanding of the market. The rise of Big Data has opened up new opportunities for gathering additional information. Customer databases and market research are not the only sources of customer information. All data from media, social networks, websites, point-of-sale, the Internet of Things (IoT) can enrich customer profiles. Once a data ecosystem is created, marketers can apply personalized marketing by customizing offers and campaigns for each specific customer.

5 Conclusion

Artificial Intelligence (AI) is becoming increasingly popular in the arena of digital marketing, and with good reason: it can help marketers significantly improve customer engagement. AI tools enable automated analysis of customer data such as search queries, website clicks, and social media interactions to obtain valuable insights into customer behavior; these insights then enable more effective strategies for customer acquisition and retention.

References

[1] Kordon, A. (2023). The Artificial Intelligence Perspective. East-West Publishing House.

[2] Kotler, P., Kartajaya, H., & Setiawan, I. (2021). Marketing 5.0: Technology for Humanity. John Wiley & Sons.Top of Form

* * *

Numerical Model to Analyze FCS (Fluorescence Correlation Spectroscopy) Sata – the Case for Micro-Flow Near the Glass-Water Interface

S. Yordanov, D. Prodanov

Total Internal Reflection Fluorescence Cross Correlation Spectroscopy (TIR-FCCS) has been established as an experimental method [1] to probe hydrodynamic flows near surfaces, on length scales of tens of nanometers. Its main advantage is that fluorescence only occurs for tracer particles close to the surface, thus resulting in high sensitivity. The measured correlation curves depend on the flow parameters of interest, such as the shear rate and the slip length. In the present work, we show how to combine detailed and fairly realistic theoretical modelling of the phenomena by Brownian Dynamics simulations with accurate measurements of the correlation curves, in order to establish a quantitative method to retrieve the flow properties from the experiments [2]. Firstly, Brownian Dynamics is used to sample highly accurate correlation curves for a fixed set of model parameters. Secondly, these parameters are varied systematically by means of an importance-sampling Monte Carlo procedure in order to fit the experiments. This provides the optimum parameter values together with their statistical error bars. The approach is well suited for massively parallel computers, which allows us to do the data analysis within moderate computing times. The method is applied to flow near a hydrophilic surface, where the slip length is observed to be smaller than $10nm$, and, within the limitations of the experiments and the model, indistinguishable from zero.

Summary

A good understanding of liquid flow in confined geometries is not only of fundamental interest, but also important for a number of industrial and technological processes, such as flow in porous media, electro-osmotic flow, particle aggregation or sedimentation, extrusion and lubrication. It is also essential for the design of micro- and nano-fluidic devices, e. g. in lab-on-a-chip applications. However, in all these cases, an accurate quantitative description is only possible if the flow at the interface between the liquid and the solid is thoroughly understood.

Important parameter that defines the flow velocity on the surface is the so called slip length - non-zero slip length means the boundary velocity on the interface is also non-zero. This boundary condition is important to know in order to describe flow behaviour correctly.

TIR-FCCS is an optical technique, which allows measuring the slip length be means of the auto- and cross-correlation of the recorded intensity signals from two probed volumes.

Analysing such correlation data is trivial in normal 3D diffusion without flow, but in case of a flow there is no closed form analytical solution.

Therefore, we develop a suitable numerical model [2], which can simulate the experimental data in the presence of flow and extract the relevant parameters of interest such as - slip length, shear rate etc.

First, we describe the TIR-FCCS technique. Second, we present the theoretical model that describes the experimental geometry. Third, we describe our Brownian Dynamics sampling algorithm that generates correlations giving fix set of input parameters. Fourth, we introduce a Monte-Carlo importance sampling analysis to fit the data and extract the error bars. At the end we give an example with analysing micro-flow data over hydrophilic surface to extract the slip length and the shear rate.

Acknowledgements

The present work was funded by the European Union's Horizon Europe program under grant agreement VIBraTE 101086815.

References

[1] S. Yordanov, A. Best, H. J. Butt, and K. Koynov, Optics Express **17**, 21149 (2009).

[2] R. Schmitz, S. Yordanov, H. J. Butt K. Koynov, and B. Dünweg, Physical Review E **84**, 066306 (2011).

* * *

Adaptive Combination Methods of Picard and Upwind-Newton (PUN) Iteration for Solving Nonlinear Diffusion Equations

G. Yuan, X. Hang

Picard and Newton iterations are commonly used methods for solving nonlinear diffusion equations. The construction of the so-called upwind-Newton iteration method is as follows: first, the nonlinear diffusion equation is linearized by Newtonian methods to form a linear convection-diffusion equation, then the diffusion term is discretized in a central type, and the convection term is discretized in an upwind type. In this talk an adaptive combination of Picard iteration and upwind-Newton iteration is introduced, which adopt the Picard iteration of wide range convergence for the first few steps, and shift automatically between Picard and upwind-Newton iteration according to the variation of the values on every cell-edges. The technique is not only novel, but also simple and efficient, which avoids traditional complex and time-cost techniques such as the linear searching technique. The other novelty is that we prove the convergence of the upwind-Newton method, which gives an interesting corollary, i.e., if

the solution at certain iteration step is of first order accuracy to the implicit solution, then the upwind-Newton method gives a second order accurate solution at the next iteration step. Numerical results verify that the adaptive combination of Picard iteration and upwind-Newton iteration is both efficient and robust, and even obviously more faster than the Picard and Newton iteration algorithms.

* * *

Predictive Modeling of Acute Morbidity Based on Air Quality Data

P. Zhivkov

1 Introduction

Air pollution, specifically outdoor particulate matter with a diameter of 2.5 micrometers (PM2.5) and 10 micrometers (PM10), is currently the leading environmental risk factor contributing to the global burden of illness, rising from the fifth position in 1990 [1].

Studies show a strong link between air pollution and respiratory hospital admissions [2,3]. Finaly to be concluded by a cohort review of 175 papers that exposure to air pollution increases the chance of developing a variety of diseases [4].

In light of these findings, there is a growing need for predictive models that can forecast acute morbidity rates based on air quality data. The aim is to predict the visitations in 3 following days based on PM concentrations. To do this, air qulity data from over 300 citizen and five official monitoring stations across Sofia is analysed. This data is compared with morbidity rates from two big hospitals. Results are compared and fine-tuned models are applied on selected morbities. The final results draw the conclusion that the two selected models can provide stable predictions on potential health risks associated with different air pollution levels.

2 Data and methods

We collect over the period 1 January 2018 to 1 March 2019 data for acute morbidity cases from emergency services and two hospitals Tokuda and Pirogov. Simultaneously, air pollution data for these 451 days is gathered from two sources: official and low-cost air quality stations, ensuring spatiotemporal alignment with health data. As there missing values exist within the air quality dataset, a strategy of imputing missing values with the mean of each column is adopted. This approach ensures the preservation of data integrity while mitigating the impact of missing entries on subsequent analyses. Pertinent features for model training are identified through careful examination and domain expertise.

The morbidity dataset examined in this research comprises multiple columns denoting distinct health conditions categorized by the International Classification of Diseases, 10th Revision (ICD-10) codes. Each column serves as a conduit for investigating specific morbidity clusters, thereby facilitating a comprehensive exploration of health implications associated with exposure to air pollution. The morbidity cases in the dataset of the research are grouped based on their corresponding ICD-10 codes: Diabetes Mellitus (E10-E11), Otitis Media and Related Conditions (H65-H66.0H81), Cardiovascular Diseases (I20-I25 I50), Hypertension (I10), Respiratory Tract Infections and Diseases (J00-J06,J20-J21,J30-J39,J40-J47,J44), Asthma (J45J45.9), Gastritis and Duodenitis (K29), Skin Disorders (L00-L08), and Syncope and Collapse (R55).

The dataset is partitioned into training and testing sets to facilitate model training and subsequent evaluation in a ration 80:20. This partitioning, typically done with a predefined ratio ensures the independence of training and testing data, thereby preventing overfitting and enabling robust model assessment.

Two distinct modeling approaches, Random Forest (RF) and Support Vector Machine (SVM), are explored. These models are chosen based on their versatility, ability to handle complex datasets, and proven efficacy in regression tasks.

Hyperparameter tuning is employed using Grid Search Cross-Validation (GridSearchCV) to optimize model performance. This systematic approach involves searching through a predefined grid of hyperparameters to identify the combination that yields the best model performance. Hyperparameters such as the number of estimators, maximum depth, and kernel type are tuned for both RF and SVM models to enhance predictive accuracy. Feature scaling using StandardScaler is incorporated into the modeling pipeline to address potential disparities in the magnitude of feature values.

3 Results

According to the updated Air Quality Guidelines (AQGs) from the World Health Organization (WHO), during the course of the study - 451 days in total, 203 days exceeded the healthy limit for PM levels.

From the nine groups of morbidities our models pefromed best on the following three groups and we selected them for further fine-tune of the models. This result can be considered as the following 3 groups are mostly correlated to PM, they are: 'Asthma',' Respiratory Tract Infections', and 'Cardiovascular Diseases'.

The predictive performance of the RF and SVM models was enhanced through systematic hyperparameter tuning. Hyperparameter tuning is a critical step in optimizing model performance by identifying the combination of hyperparameters that yield the best results. The fine-tuning process involved the following three steps: GridSearchCV, Parameter Grid Definition, and $K - foldcross - validation$.

The final results for the 3 groups of morbidies are shown in Table 1.

Table 1: Results After Fine-Tuning of RF and SVM Models

Condition	**Metric**	**RF**	**SVM**
Asthma	Mean Absolute Error	7.66	7.08
	Root Mean Squared Error	9.64	9.48
	R-squared	0.74	0.71
Respiratory Tract Infections	Mean Absolute Error	12.39	14.01
	Root Mean Squared Error	16.68	17.95
	R-squared	0.57	0.34
Cardiovascular Diseases	Mean Absolute Error	4.55	4.45
	Root Mean Squared Error	5.56	5.44
	R-squared	0.23	0.31

Both RF and SVM models demonstrated improved performance after fine-tuning across all health conditions compared to their initial results. The fine-tuned models exhibited decreased MAE and RMSE values, indicating enhanced accuracy in predicting the severity of various health conditions. Moreover, the increase in R-squared values suggests that the fine-tuned models better capture the variability in disease occurrence.

Air quality data is crucial in understanding the health effects of air pollution and developing effective strategies for mitigating its impact on public health. Therefore, studies are essential to identify factors of susceptibility specific to health outcomes [5].

4 Conclusion

In summary, the RF and SVM models were evaluated for their efficacy in predicting morbidity based on selected air quality values. While both models demonstrated respectable performance, after fine-tuning both models showed lower error metrics and higher R-squared value, further investigation and refinement may be warranted to enhance predictive accuracy and better understand the underlying dynamics of air quality fluctuations.

The predictive modeling of acute morbidity based on air quality data holds promise for enhancing healthcare systems and improving patient outcomes. The methodology outlined above serves as a foundation for generating valuable insights and planning proactive healthcare interventions.

In conclusion, by leveraging advanced machine learning techniques and gathering air quality data from various monitoring stations, we provide predictions on potential short-term health risks associated with PM levels, establishing a quantitative relationship between air pollution levels and acute morbidity rates.

Acknowledgements

The work is supported by the National Scientific Fund of Bulgaria grant DFNI KP-06-N52/5 .

References

[1] Christopher JL Murray. The global burden of disease study at 30 years. *Nature medicine*, 28(10):2019–2026, 2022.

[2] Lisha Luo, Yunquan Zhang, Junfeng Jiang, Hanghang Luan, Chuanhua Yu, Peihong Nan, Bin Luo, and Mao You. Short-term effects of ambient air pollution on hospitalization for respiratory disease in taiyuan, china: a time-series analysis. *International journal of environmental research and public health*, 15(10):2160, 2018.

[3] Petar Zhivkov and Alexandar Simidchiev. Quantitative relationship between particulate matter and morbidity. In *International Conference on Large-Scale Scientific Computing*, pages 275–283. Springer, 2021.

[4] Norfazillah Ab Manan, Azimatun Noor Aizuddin, and Rozita Hod. Effect of air pollution and hospital admission: a systematic review. *Annals of global health*, 84(4):670, 2018.

[5] Reza Bayat, Khosro Ashrafi, Majid Shafiepour Motlagh, Mohammad Sadegh Hassanvand, Rajabali Daroudi, Günther Fink, and Nino Künzli. Health impact and related cost of ambient air pollution in tehran. *Environmental research*, 176:108547, 2019.

* * *

Operator Preconditioning and Reduced Basis Methods

L. Zikatanov

This work is on a fast and accurate reduced basis method for solving discretized fractional elliptic partial differential equations. A direct computation of the action of such an approximation would require solving multiple large-scale sparse linear systems. Our method constructs the reduced basis using the first few directions obtained from the preconditioned conjugate gradient method applied to one of the linear systems. This reduces the computational cost dramatically because: (1) We only use one of the large-scale problems to construct the basis; and (2) all large-scale problems restricted to the subspace have much smaller sizes. We test our algorithms for fractional PDEs on a 3d Euclidean domain, a 2d surface, and random combinatorial graphs. We also use a novel approach to construct the rational approximation for the fractional power function by the orthogonal greedy algorithm (OGA). This is a joint work with Cheng Zuo (Penn State, USA) and Yuwen Li (Zhejiang University, China).

List of participants

Lidia Aceto
Università del Piemonte Orientale,
Dipartimento di Scienze e
Innovazione Tecnologica
Viale Teresa Michel, 11
15121 Alessandria, Italy
lidia.aceto@uniupo.it

Hitesh Bansu
Institute of Information and
Communication Technologies,
Bulgarian Academy of Sciences
Acad. G. Bonchev Str., bl. 25A
1113 Sofia, Bulgaria
hiteshbansu@gmail.com

Raphaël Bulle
Department of Mathematics and Statistics,
Université Laval
2325 rue de l'Université
G1V 0A6 Québec, Canada
rbulle@tutanota.com

Jun Cao
Department of Mechanical, Industrial,
and Mechatronics Engineering,
Toronto Metropolitan University
M5B 2K3 Toronto, Ontario, Canada
jcao@torontomu.ca

Maria Datcheva
Institute of Mechanics
Bulgarian Academy of Sciences
Acad. G. Bonchev Str., Bl. 4
1113 Sofia, Bulgaria
datcheva@imbm.bas.bg

Hristo Djidjev
Institute of Information and
Communication Technologies,
Bulgarian Academy of Sciences
Acad. G. Bonchev Str., bl. 25A
1113 Sofia, Bulgaria
hdjidjev@msn.com

Nina Dobrinkova
Institute of Information and
Communication Technologies,
Bulgarian Academy of Sciences
Acad. G. Bonchev Str., bl. 2
1113 Sofia, Bulgaria
nina.dobrinkova@iict.bas.bg

Stefka Fidanova
Institute of Information and
Communication Technologies,
Bulgarian Academy of Sciences
Acad. G. Bonchev Str., bl. 25A
1113 Sofia, Bulgaria
stefka.fidanova@gmail.com

Ivan Georgiev
Institute of Information and
Communication Technologies,
Bulgarian Academy of Sciences
Acad. G. Bonchev Str., bl. 2
1113 Sofia, Bulgaria
ivan.georgiev@parallel.bas.bg

Silvia Grozdanova
Institute of Information and
Communication Technologies,
Bulgarian Academy of Sciences
Acad. G. Bonchev Str., bl. 25A
1113 Sofia, Bulgaria
silvia@parallel.bas.bg

Silvi-Maria Gurova
Institute of Information and
Communication Technologies,
Bulgarian Academy of Sciences
Acad. G. Bonchev Str., bl. 25A
1113 Sofia, Bulgaria
smgurova@parallel.bas.bg

Xudeng Hang
Institute of Applied Physics and
Computational Mathematics,
Fenghaodong Road, Haidian District,
Beijing 100094, China
hang_xudeng@iapcm.ac.cn

Stanislav Harizanov
Institute of Information and
Communication Technologies &
Institute of Mathematics and Informatics,
Bulgarian Academy of Sciences
Acad. G. Bonchev Str., bl. 25A
1113 Sofia, Bulgaria
sharizanov@parallel.bas.bg

Roumen Iankov
Institute of Mechanics
Bulgarian Academy of Sciences
Acad. G. Bonchev Str., Bl. 4
1113 Sofia, Bulgaria
iankovr@abv.bg

Oleg Iliev
Fraunhofer Institute for Industrial
Mathematics, ITWM
Fraunhofer Platz 1
67663 Kaiserslautern, Germany
oleg.iliev@itwm.fraunhofer.de

Nevena Ilieva
Institute of Information and
Communication Technologies,
Bulgarian Academy of Sciences
Acad. G. Bonchev Str., bl. 25A
1113 Sofia, Bulgaria
nevena.ilieva@iict.bas.bg

Veselin Ivanov
Faculty of Medicine,
Trakia University
Stara Zagora, Bulgaria
veskoasenov@abv.bg

Vladimir Ivanov
National Institute of Geophysics,
Geodesy and Geography,
Bulgarian Academy of Sciences
Acad. G. Bonchev Str., bl. 3
1113 Sofia, Bulgaria
vivanov@geophys.bas.bg

Ivaylo Katzarov
Institute of Metal Science
Equipment and Technologies,
Bulgarian Academy of Sciences
67 Shipchenski prohod Str.
1574 Sofia, Bulgaria
ivo@ims.bas.bg

Virginia Kiryakova
Institute of Mathematics and Informatics,
Bulgarian Academy of Sciences
Acad. G. Bonchev Str., bl. 8
1113 Sofia, Bulgaria
virginia@diogenes.bg

Nikola Kosturski
Institute of Information and
Communication Technologies,
Bulgarian Academy of Sciences
Acad. G. Bonchev Str., bl. 25A
1113 Sofia, Bulgaria
nikola.kosturski@iict.bas.bg

Johannes Kraus
University of Duisburg-Essen
Thea-Leymann-Str. 9
45127 Essen, Germany
johannes.kraus@uni-due.de

Raytcho Lazarov
Texas A&M University,
Department of Mathematics
2909 CORTEZ CT
77843 College Station, TX, USA
&
Institute of Mathematics and Informatics,
Bulgarian Academy of Sciences
Acad. G. Bonchev Str., bl. 8
1113 Sofia, Bulgaria
raytcho.lazarov@gmail.com

Elena Lilkova
Institute of Information and
Communication Technologies,
Bulgarian Academy of Sciences
Acad. G. Bonchev Str., bl. 25A
1113 Sofia, Bulgaria
elena.lilkova@iict.bas.bg

Ivan Lirkov
Institute of Information and
Communication Technologies,
Bulgarian Academy of Sciences
Acad. G. Bonchev Str., bl. 25A
1113 Sofia, Bulgaria
ivan@parallel.bas.bg

Svetozar Margenov
Institute of Information and
Communication Technologies,
Bulgarian Academy of Sciences
Acad. G. Bonchev Str., bl. 25A
1113 Sofia, Bulgaria
margenov@parallel.bas.bg

Maya Neytcheva
Uppsala University,
Department of Information Technology
Box 337
75105 Uppsala, Sweden
maya.neytcheva@it.uu.se

Tzvetan Ostromsky
Institute of Information and
Communication Technologies,
Bulgarian Academy of Sciences
Acad. G. Bonchev Str., bl. 25A
1113 Sofia, Bulgaria
ceco@parallel.bas.bg

Miryana Raykovska
Institute of Information and
Communication Technologies,
Bulgarian Academy of Sciences
Acad. G. Bonchev Str., bl. 2
1113 Sofia, Bulgaria
mirianaraykovska@gmail.com

Dimitar Slavchev
Institute of Information and
Communication Technologies,
Bulgarian Academy of Sciences
Acad. G. Bonchev Str., bl. 25A
1113 Sofia, Bulgaria
dimitargslavchev@parallel.bas.bg

Jelenko Stanchov
Institute of Information and
Communication Technologies,
Bulgarian Academy of Sciences
Acad. G. Bonchev Str., bl. 2
1113 Sofia, Bulgaria
elenko.stanchov@gmail.com

Yavor Vutov
Institute of Information and
Communication Technologies,
Bulgarian Academy of Sciences
Acad. G. Bonchev Str., bl. 25A
1113 Sofia, Bulgaria
yavor@parallel.bas.bg

Stoyan Yordanov
Institute of Information and
Communication Technologies,
Bulgarian Academy of Sciences
Acad. G. Bonchev Str., bl. 2
1113 Sofia, Bulgaria
stoyan.yordanov@iict.bas.bg

Svetlozar Yordanov
Institute of Information and
Communication Technologies,
Bulgarian Academy of Sciences
Acad. G. Bonchev Str., bl. 2
1113 Sofia, Bulgaria
svetlozar@parallel.bas.bg

Guangwei Yuan
Institute of Applied Physics and
Computational Mathematics,
Fenghaodong Road, Haidian District
Beijing 100094, China
yuan_guangwei@iapcm.ac.cn

Petar Zhivkov
Institute of Information and
Communication Technologies,
Bulgarian Academy of Sciences
Acad. G. Bonchev Str., bl. 25A
1113 Sofia, Bulgaria
zhivkovpetar@gmail.com

Ludmil Zikatanov
Penn State University ,
Department of Mathematics
239 McAllister Bldg, Penn State
16802 State College, PA, USA
ludmil@psu.edu